AIRS CLASSIFIERS IN HANDWRITING RECOGNITION

Conference Paper · December 2013

3 authors:

Hamid Seridi
Université 8 mai 1945 - Guelma
159 PUBLICATIONS 495 CITATIONS

Merabti Hocine
Université Kasdi Merbah Ouargla
7 PUBLICATIONS 9 CITATIONS

Med Nadjib Kouahla
Université 8 mai 1945 - Guelma
33 PUBLICATIONS 49 CITATIONS

CONTROL ENGINEERING TECHNOLOGIES CONFERENCE

DAKAM Publishing (D/PB)
May 2014 , İstanbul.

www.dakam.org
Tarık Zafer Tunaya Sokak 19/2, 34437; Istanbul

Control Engineering Technologies Conference
CONTECH '13 / Control Engineering Technologies Conference Proceedings
Dec 26-28, 2013, İstanbul
organized by DAKAM (Eastern Mediterranean Academic Research Center)
hosted by Yildiz Technical University

Academic Advisor:
Asst. Prof. Alptekin Ergenç - Yildiz Technical University

Edited by: Pelin Alcan, Burçak Ada Döner
Design: Özgür Aydoğan
Cover Design: D/GD (DAKAM Graphic Design)
Print: Metin Copy Plus / Artı Dijital & Baskı Merkezi
Türkocağı Cad No:3 Türkiye Gazeteciler Cemiyeti Altı, İran Kon. Karşısı, Cağaloğlu, İstanbul
ISBN: 978-605-5120-82-5

CONTECH'13

CONTROL ENGINEERING TECHNOLOGIES CONFERENCE

DEC 26-28, 2013

YILDIZ TECHNICAL UNIVERSITY

DAKAM Publishing

CONTENTS

7 CONTROL ENGINEERING TECHNOLOGIES

9 INDIRECT FORCE CONTROL IN 6DOF HUMANOID ROBOT ARM USING IMPEDANCE CONTROLLER
Behnaz Hosseini, Cihat Bora Yigit,
Arezou Rahimi, Pinar Boyraz

23 VISUAL SERVO-CONTROL APPLICATION IN HUMANOID ROBOTS USING DEPTH-CAMERA INFORMATION
Arezou Rahimi, Cihat Bora Yigit,
Behnaz Hosseini, Pinar Boyraz

35 INDUSTRIAL APPLICATION OF ANALYSIS AND VIBRATION MONITORING OF ROTATING MACHINES. PRACTICAL CASE
OUALI Mohammed, MAGRAOUI Rabah, MEGHATRIA M'Hamed

51 PREDICTIVE VIBRATIONAL DIAGNOSTICS OF ROTATING MACHINES VENTILATOR ATOMISER APPLICATION
MAGRAOUI Rabah, OUALI Mohammed, TEMMAR Mustapha

63 DYNAMIC BEHAVIOR OF PIEZOELECTRIC BEAMS. ELASTIC AND PIEZOELECTRIC CASES
Bouhedma Sofiane, Ouali Mohammed, Mahieddine Ali

77 INDUCTION MACHINE MODELING USING FINITE ELEMENT METHOD UNDER STATOR SHORT-CIRCUIT FAULT
A. Bouzida, O. Touhami and R. Abdelli

79 ROTOR FLUX ESTIMATION BASED ON ACCURATE ADAPTIVE ALGORITHM FOR FIELD ORIENTED CONTROL INDUCTION MACHINE DRIVES
A. Aibeche, M. Kidouche, H. Akroum and S. Grouni

81 ACTUATION USING PIEZOELECTRIC BIMORPH BEAMS UNDER THE EFFECTS OF STRUCTURAL DAMPING
Zemirline Adel, Ouali Mohammed and Mahieddine Ali

89 ANALYSIS METHODS FOR THE DETERMINATION OF ENERGIES ACTIVATION AND THE STUDY OF THE PRECIPITATION REACTIONS IN AL-CU ALLOYS
H. Bensouyad

95 MODEL-BASED ROBUST TRAJECTORY CONTROL OF 6-DOF STEWART PLATFORM
Dr. Mohammad Al-Khedher

103 IMAGE GUIDED STEERABLE PROBE PATH PLANNING
Minou Kouhsoltani, Sohrab Khanmohammadi

109 A REAL TIME RT-LAB BASED DISCRETE SPACE VECTOR MODULATION SCHEME FOR INDUCTION MOTORS FED
A. Idir & M. Kidouche

119 MP3 FILE IDENTIFICATION BASED ON CONCURRENCE ORDER OF METADATA
Youngseok Lee, Jongweon Kim

127 AIRS CLASSIFIERS IN HANDWRITING RECOGNITION
Hamid Seridi, Hocine Merabti, Med Nadjib Kouahla

135 USING GAUSSIAN MIXTURE MODELS AND HSV COLOR SPACE FOR BACKGROUND SUBTRACTION
Farou Brahim, Seridi Hamid and Akdag Herman

147 AN IMPROVED ADAPTIVE THRESHOLDING SCHEME FOR FAULT DETECTION: APPLICATION TO A CEMENT ROTARY KILN SYSTEM
Boualem Ikhlef, Abdelmalek Kouadri,
Abderrazek Bensmail and Mimoun Zelmat

149 CRASH RESISTANCE SIMULATION, AN INVESTIGATION INTO VEHICLE FRAME STIFFNESS IN FULL FRONTAL IMPACT TEST USING LS DYNA
Benhizia A., Outtas T.

161 RELIABILITY STUDY FOR A MECHANISM AIDED BY ASYNCHRONOUS ACTUATOR POWERED BY ASYNCHRONOUS DIESEL GENERATOR
H. Meglouli, A Chebouba, Y Naoui

CONTROL ENGINEERING TECHNOLOGIES

CONTECH '13 Control Engineering Technologies Conference took place in Istanbul, Turkey, organized by DAKAM and Yıldız Technical University. CONTECH '13 aims to provide a high level international forum to bring together industry professionals, academics, and individuals from institutions, industrials and government agencies to exchange information, share achievements, and discuss the advancement in the fields of control science and engineering, mechanic automation,information theory, communication and networking. All accepted papers will be published by DAKAM.

INDIRECT FORCE CONTROL IN 6DOF HUMANOID ROBOT ARM USING IMPEDANCE CONTROLLER

Behnaz Hosseini[1], Cihat Bora Yigit*, Arezou Rahimi[1], Pinar Boyraz*
*Mechanical Engineering Department, Istanbul Technical University
[1]Control Engineering Department, Istanbul Technical University

Abstract*:*

This paper presents the implementation of a 6 DOF impedance control on a humanoid robot arm (UMAY) to balance interaction forces between arm and its surrounding environment. A concise description of analyzing procedure is given for modeling and simulation of a robot arm focusing on the particular way it interacts with its environment under impedance control scheme. The modeling and comparison are made by adopting Matlab/ Simulink environment, in which we use SimMechanics to produce the mechanical model of UMAY's 6 DOF arm. An alternative Euler angle-based method, which moderates the effects of representation singularities, is used to display the end effector orientation. The resulting impedance controller is designed according to dynamic model based strategy in which inner loop acting on the end-effector position and orientation error is adopted to gain robustness to unmodeled dynamics and external disturbances. Final results display the impedance controller performance managing interaction forces in order to obtain safe and feasible operations within the workspace.

Introduction:

The remarkable proficiency that humans exhibit in various manipulation tasks, especially considering unknown objects or environments, is a long target of robots. For a robot manipulator to interact safely and in a human- friendly way in unknown environments, it is necessary to include an interaction control method that reliably adapts the forces exerted on the environment in order to avoid damages both in the environment and on the manipulator itself. Therefore, human-robot interaction is one of the core areas in the research effort put towards making robots safer and more human friendly. In contrast with direct force control methods which can be used in practice where the maximum or threshold value of force to be exerted is known in advance, an indirect force control technique can be found more appropriate when applied in a scenario involving unexpected collisions or contacts [1,9]. Impedance control [2] is one of these indirect force control methods. The objective of indirect force control is to control neither force nor position but their dynamic relation, the *desired impedance*, along each direction on the task space [1]. Moreover, the steady-state force can be easily set to a desired maximum value [3]. The main idea is that the impedance control system establishes virtual new impedance for the manipulator, which interacts with the environment as if new mechanical elements (mass-spring-damper system) had been included in the real manipulator [4, 8]. Humanoid UMAY is designed to target especially human-robot interaction using its multi-mode interfaces having learning capabilities. UMAY aims to help incremental rehabilitation of children with Autistic Spectrum Disorder (ASD) utilizing its modular structure [12]. (Figure1)

Figure 1. UMAY with 7 DOF head and 6DOF arm

The main contribution of this work is to exhibit the application of a six-DOF impedance control algorithm on humanoid robot-arm. To achieve this goal, first, a mechanical model of the robot structure is created using Matlab/SimMechanics. In order to make the system linear and decoupled, the impedance controller is designed according to an inverse dynamic strategy with contact force and moment measurements, leading to a resolved-acceleration scheme. For three-DOF tasks, only the end-effector position and contact linear force have to be considered. On the other hand, in order to perform six DOF tasks, a sufficient representation of end-effector orientation displacement to be related to the contact moment should be sought after. In order to mitigate the effects of representation singularities, in this paper, we used an impedance equation, which is based on a suitable set of Euler angles extracted from the mutual orientation between the compliant frame and the desired frame [4]. As final step, impedance controller is designed and used to control the forces exerted by the six DOF robot arm. To test the control system, the robot is given a reference input trajectory that causes the robot to hit a wall so as to observe the performance of the robot- environment interaction.

1.Mechanical Model:

The first step is to form the mechanical model of six DOF arm of humanoid UMAY. Figure 2 shows the model of the arm described with SimMechanics. The model is composed of six revolute joints and six rigid bodies. The module receives torques as input and yields joint angles, torques, end-effector position and orientation as outputs. Body masses, inertia matrices and center of gravities are extracted from the Solidworks model of the UMAY arm. SimMechanics automatically creates a visualization of all the bodies in mechanical model. During simulation, a motion simulation of the mechanism is generated to observe the motion capability closer. Figure 3 shows the visualization of UMAY SimMechanics model.

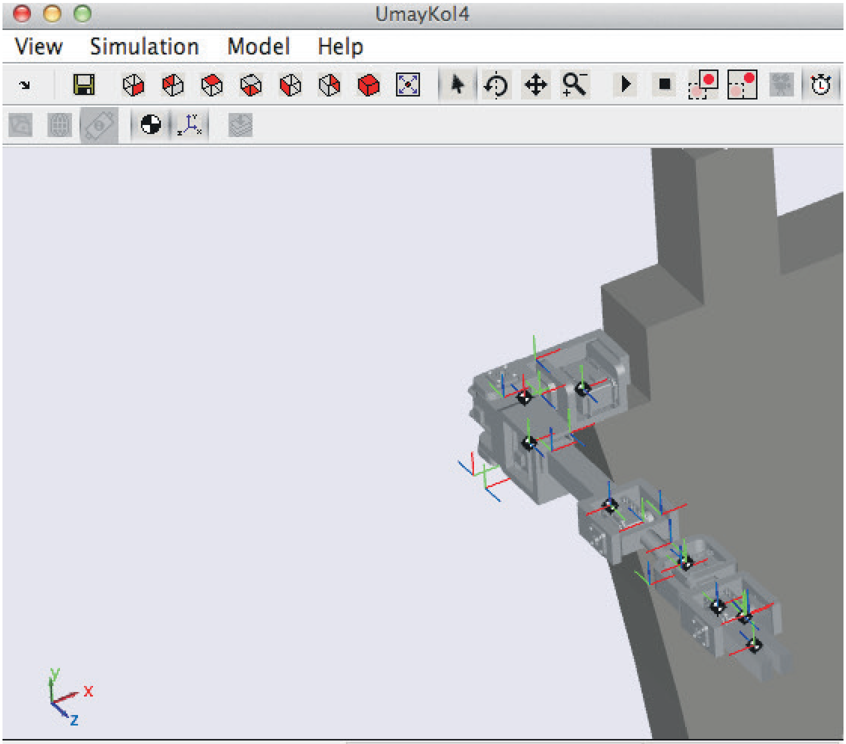

Figure 3. Visualizing UMAY robot arm in SimMechanics

2.Dynamical Model:

We will be introducing the general dynamic model of the generic 6 DOF robot arm here and then apply the results to the arm of humanoid UMAY. For a six-DOF rigid robot manipulator, the dynamic model can be written in Lagrangian form

$$B(q)\,\underline{\ddot{q}}+\underline{C}+d+J^{T}(q)\,h=\tau \qquad (1)$$

Where q is the (6×1) vector of joint variables, B is the (6× 6) generalized mass matrix, $\underline{C}$ is the (6× 1) bias terms including Coriolis and gravity, d is the (6× 1) vector of friction torques, τ is the the (6×1) vector of driving torques, h=$[f^{T}\ \mu^{T}]^{T}$ is the (6× 1) vector of contact forces exerted by the end effector on the environment and finally J is the (6×6) Jacobian matrix. In order to achieve dynamic parameters of the UMAY robot arm, we used Spatial Operator Algebra (SOA) method [6], in which we use two main equations (2) and (3)

$$B = H^{T}\,\phi^{T}\,M\,\phi\,H \qquad (2)$$

$$C = H^{T}\,\phi^{T}(M\,\phi\,a + b) \qquad (3)$$

In equations (2) and (3), the variables are described as follows:

H is the axis of rotation and/or translation matrix of the arm,

ϕ is the propagation operator of the arm,
M is the Mass matrix of the arm,
a is the Stacked bias spatial acceleration of the arm,
b is the Stacked bias spatial forces of the arm.

3. Dynamic Model-Based Compensation

The dynamic model in the form (1) is represented by a set of n second-order coupled and nonlinear differential equations relating the joint positions, velocities and accelerations to the joint torques and end-effector force and moment. A classical strategy to control this type of mechanical system is using the inverse dynamic control, which is aimed at linearizing and decoupling the manipulator dynamics via feedback. Nonlinearities such as Coriolis, gravity and friction torques can be merely cancelled by adding these terms to the control input, while decoupling can be achieved by weighting the control input by the inertia matrix [4,5,7]. According to this dynamic model-based compensation, the joints driving torques can be chosen as seen in equation (4)

$$\tau = B\,(q)\,\alpha + \underline{C} + d \qquad (4)$$

Folding this control law into the system model yields (5)

$$\ddot{q} = \alpha \qquad (5)$$

Equation (5) constitutes a linear and decoupled system corresponding to a double integrator between the input α and the input q. The quantity α represents a resolved acceleration in terms of joint variables. Since equation (5) contains $\ddot{q}$, it is worth considering the time derivative of the end-effector velocity (V_e), i.e.

$$\dot{V}_e = J\,(q)\,\ddot{q} + \dot{J}\,(q, \dot{q})\,\dot{q} \qquad (6)$$

At this point, the control input α can be chosen as indicated in (7) and (8);

$$\alpha = J^{-1}(q)\,(a - \dot{J}\,(q, \dot{q})\,\dot{q}) \qquad (7)$$
$$\dot{V}_e = a \qquad (8)$$

Where *a* attains the meaning of a resolved acceleration in terms of end effector variables and we can partition *a* into its linear and angular components, i.e

$$a = \begin{bmatrix} a_o \\ a_p \end{bmatrix} \qquad (9)$$

Therefore equation (8) can be written as in (10) and (11)

$$\ddot{p}_e = a_p \qquad (10)$$
$$\dot{\omega}_e = a_o \qquad (11)$$

a_o and a_p are designed so as to ensure tracking of the reference end-effector orientation and position trajectory, respectively.

Assuming no interaction with the environment (h=0): A position error between the reference and actual end-effector position can be defined as in (12)

$$\Delta p_{de} = p_d - p_e \quad (12)$$

Then the resolved linear acceleration can be chosen as in (13)

$$a_p = \ddot{p_d} + K_{Dp} \Delta \dot{p_{de}} + K_{Pp} \Delta p_{de} \quad (13)$$

, where K_{Dp} and K_{Pp} are suitable feedback matrix gains. Substituting (13) in (10) gives the closed-loop dynamic behavior of position error

$$\Delta \ddot{p_{de}} + K_{Dp} \Delta \dot{p_{de}} + K_{Pp} \Delta p_{de} = 0 \quad (14)$$

In order to define orientation error, an alternative Euler angles error can be considered which is based on the rotation matrix describing the mutual orientation between reference and end-effector frames (see (15)).

$$R_d^e = R_e^T R_d \quad (15)$$

Differentiating (15) with respect to time gives (16)

$$\dot{R_d^e} = S(\Delta \omega_{de}^e) R_d^e \quad (16)$$

, where $S(\Delta \omega_{de}^e)$ is the skew symmetric matrix of end-effector angular velocity error, which has been referred to the end-effector frame. Considering φ_{re} as the set of Euler angles that can be extracted from R_r^e, we can achieve the relation of $\Delta \omega_{de}^e$ and the time derivative of φ_{de} like the way shown in (17)

$$\Delta \omega_{de}^e = T(\varphi_{de}) \dot{\varphi_{de}} \quad (17)$$

The time derivative of (17) gives the acceleration relationship in the form of (18)

$$\dot{\omega_e} = \dot{\omega_d} - T_e(\varphi_{de}) \ddot{\varphi_{de}} - \dot{T_e}(\varphi_{de}, \dot{\varphi_{de}}) \dot{\varphi_{de}} \quad (18)$$

, where

$$T_e(\varphi_{de}) = R_e T(\varphi_{de}) \quad (19)$$

In view of (18), the resolved angular acceleration can be chosen as in (20)

$$a_o = \dot{\omega_d} + T_e(\varphi_{de})(K_{Do} \dot{\varphi_{de}} + K_{po} \varphi_{de}) - \dot{T_e}(\varphi_{de}, \dot{\varphi_{de}}) \dot{\varphi_{de}} \quad (20)$$

, where K_{Do} and K_{po} are suitable feedback matrix gains. Substituting (20) into (11) gives the closed loop dynamic behavior of the orientation error expressed in (21)

$$\ddot{\varphi}_{de}+K_{Do}\,\varphi_{de}+K_{po}\,\varphi_{de}=0 \qquad (21)$$

The system described in (21) is exponentially stable for any choice of positive definite K_{Do} and K_{po}. The clear advantage of the alternative over the classical Euler angles error is that by adopting a representation φ_{de}= $[\alpha_{de}, \beta_{de}, \gamma_{de}]^T$ for which T (0) is nonsingular, representation singularities occur only for large orientation errors, e.g. when β_{de} =$\pm\pi/2$ for XYZ representation. In other words, the ill-conditioning of matrix T is not influenced by the desired or actual end-effector orientation but only by the orientation error; hence, as long as the error parameter satisfies the relationship given by | β_{de} |< $\pi/2$, the behavior of system is not affected by the representation singularities. [7,10]

4.Impedance Controller:

So far we have modeled and controlled the dynamics of 6-DOF UMAY arm without considering any interaction with the environment. The next step is to design a controller that regulates the interaction when the robot contacts the environment. The simple scenario can be described as follows: at present, if the robot follows a pre-defined trajectory that is determined on its way to an object, it may collide with the object, then trying again to reach the final end position of the given trajectory, and hence, likely to be exerting large forces into the contact environment, therefore, that would likely to have high degree of damages to a real robot and/or the object of collision. To avoid such massive impact forces, an impedance controller is introduced so that its input is the reference trajectory at each time step. Additionally, the measured contact forces will be included on the controller so as to get an immediate feedback of the contact state. The output will be a modified trajectory that takes into account the contact forces. This frame is referred to as the compliant frame and is specified by a position vector p_c and a rotation matrix R_C. In this way, the inverse dynamics motion control strategy can be still adopted as long as the actual end-effector position p_e and orientation R_e is taken to coincide with p_c and R_c in lieu of p_d and R_d respectively. That means, if no forces are sensed, the trajectory will be followed strictly. Otherwise, when forces are measured, the trajectory will be modified in order to limit the maximum steady-state forces and to dynamically behave as the mass- spring-damper system. A block diagram of the resulting scheme is sketched in figure 4, which reveals the presence of an inner motion control loop with respect to the outer impedance control loop. [10]

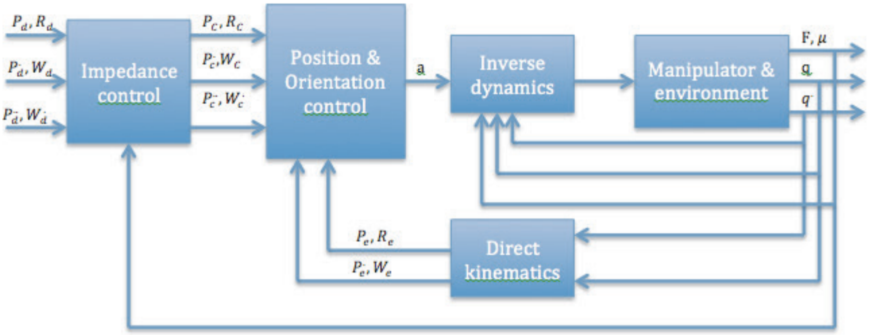

Figure 4. Impedance control structure with inner motion control loop

The translational impedance equation is chosen so as to enforce an equivalent mass-damper-spring behavior for the position displacement when the end-effector exerts a force f on the environment, like the equation given in (22)

$$M_p \bigtriangleup \ddot{p}_{dc} + D_P \bigtriangleup \dot{P}_{dc} + K_p \bigtriangleup p_{dc} = \mathrm{f} \qquad (22)$$

, where M_p, D_P and K_p are positive definite matrices.

Figure 5 shows the translational impedance control scheme. The controller parameters were M_p= 5kg, D_p= 1000Ns/m and K_p = 10N/m.

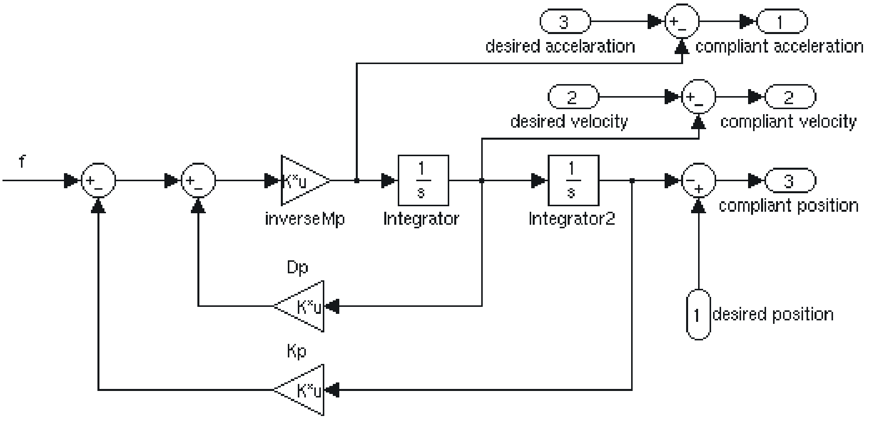

Figure5. Translational impedance control scheme

With reference to the scheme in figure 4, the translational impedance control generates the reference position for the inner motion control. Therefore, in order to allow the implementation of the complete control scheme, the linear acceleration according to the previous section is

$$a_p = \ddot{p}_c + K_{Dp} \bigtriangleup \dot{p}_{ce} + K_{Pp} \bigtriangleup p_{ce} \qquad (23)$$

, where $\triangle p_{ce}= p_c - p_e$ is the position error between compliant and actual frame.

Adopting the alternative Euler angles displacement, φ_{dc}, rotational impedance at the end effector can be defined as in (24)

$$M_o \ddot{\varphi}_{dc} + D_o \dot{\varphi}_{dc} + K_o \varphi_{dc} = T^T(\varphi_{dc})\, \mu^c \quad (24)$$

, where M_o, D_o and K_o are positive definite matrices describing the generalized inertia, rotational damping, rotational stiffness, respectively, and μ^c is referred to compliant frame. Figure 6 shows the rotation impedance control scheme. . The controller parameters were M_o= 5kg, D_o= 500Ns/m and K_o = 50N/m.

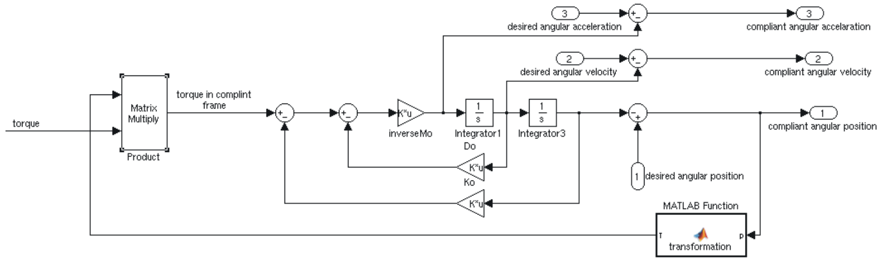

Figure 6. Rotation impedance control scheme

On the other hand, with reference to the alternative Euler angles error used in (20), the angular acceleration is taken as in (25)

$$a_o = \dot{\omega}_d - \dot{T}_e(\varphi_{de}, \dot{\varphi}_{de})\, \dot{\varphi}_{de} - T_e(\varphi_{de})(\ddot{\varphi}_{dc} + K_{Do}(\dot{\varphi}_{dc} - \dot{\varphi}_{de}) + K_{po}(\varphi_{dc} - \varphi_{de})) \quad (25)$$

, where the orientation control acts to take φ_{de} to coincide with φ_{dc}. [4,10]

5. Modeling Environment:

To deal with the robot interaction with the environment or external forces acting on the robot, obtaining correct model of the acting forces is crucial when designing robot applications. Therefore, a model of the environment is included in our system whose interaction force will act on our robot tool end. We assume that the environmental stiffness can be modeled as a linear spring with a spring constant K_e, and a damper with a damping constant B_e, so it can be modeled as in (26)

$$f = K_e(x - x_e) + B_e(\dot{x} - \dot{x}_e) \quad (26)$$

In (26) f is the contact force, x is the end-effector position at the contact point, x_e is the static position of the environment and x_d is the desired end-effector position. As we see in (1), in order to take contact forces into account on the dynamic response, the term J^Th translates the task-space forces acting on the end-effector to the joint space making use of the transpose of the Jacobian. [11]

6. Results:

In order to test the performance of the control system, in the case of no interaction with the environment, the desired trajectories are given to the robot arm. The input trajectory for the X-axis is a ramp starting at 0.1159 (m) with slope of 0.02 (m/s), which continues with the constant value 0.2159 (m) after 5 seconds. The reference for the alpha angle is the ramp starting at 0.3694 (rad) with slope of 0.02 (rad/s) and continues with constant value 0.4694 (rad) after t=5s. In control loop, we set K_{Dp}=K_{Do}=1000, K_{Pp}=K_{Po}=2000. As it can be seen in figures 8 and 9, the end-effector is tracking given desired trajectory with high accuracy. The mean square errors (MSE) in this operation for position tracking is 1.1255e-7 and for rotation tracking is 4.3832e-11, which emphasize on the high performance of the controller.

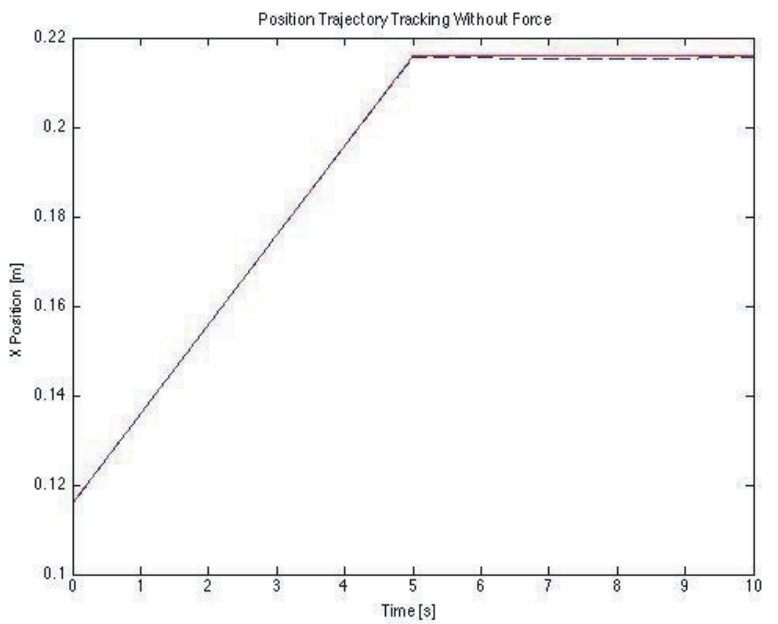

Figure 8. Position (X) trajectory tracking
Without applying force on end-effector

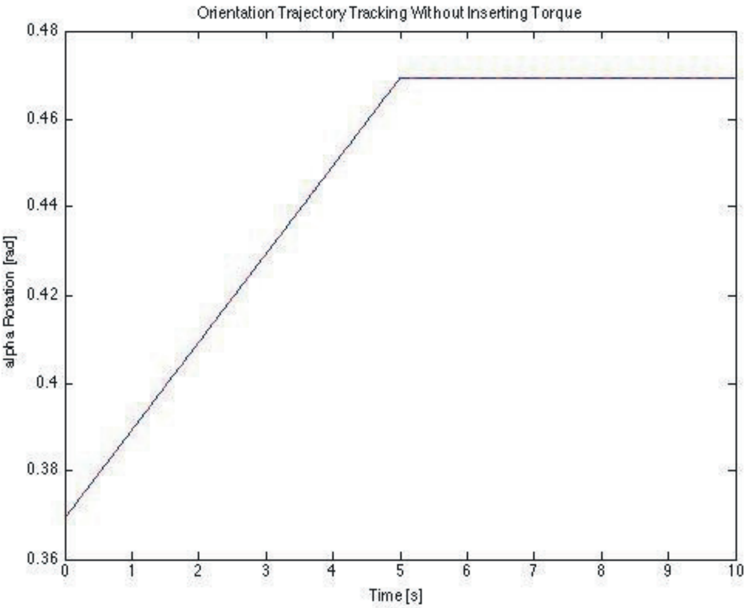

Figure 9. Orientation (alpha) trajectory tracking
without applying torque on end-effector

In order to show the response of the position impedance control system while approaching and contacting the environment, at X=0.23, we installed a wall, which modeled as defined in (26) with K_e=500000 N/m, B_e=0.1 Ns/m. Figure 10 shows that, at the contact point, the impedance controller reacts to redefine a new position trajectory that limits the steady state force, by limiting the X reference position to a value of 0.23.

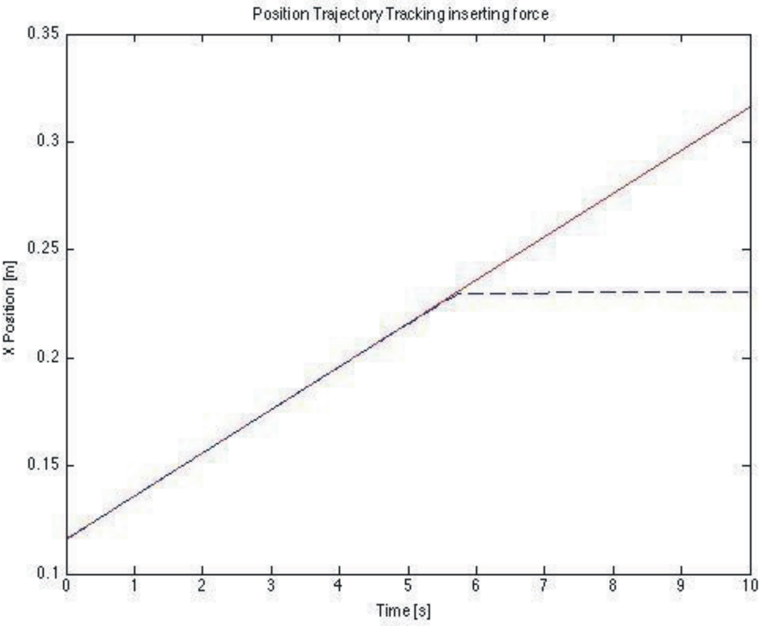

Figure 10. Position (X) trajectory tracking applying force on end-effector

On the rotation part of impedance control system, a constant torque is inserted to the system at t=4s, while the end-effector tracking given desired trajectory. Similar to the previous case, the impedance controller bounded the alpha reference angle to a value of 0.45, in order to limit the torque, which is applied to the environment by the end-effector.

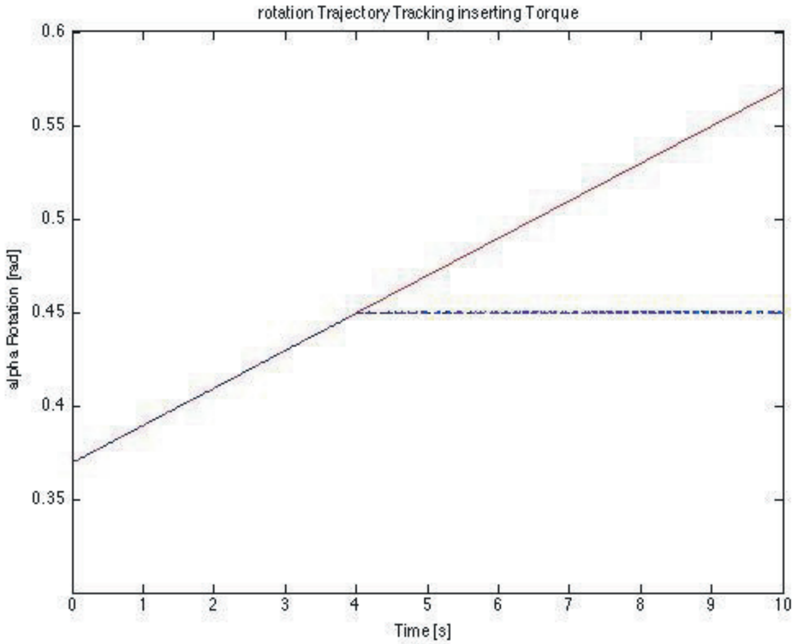

Figure 11. Orientation (alpha) trajectory tracking with applying torque on end-effector

References:

[1] N. Hogan, "Impedance Control of Industrial Robots", IEEE Transaction on Robotics, Computer, Integrated Manufacturing, Vol. 1, Issue 1, pp. 97-113, 1984.

[2] N. Hogan, Impedance control-An approach to manipulation, Journal of Dynamics Systems, Measurement, and Control-Transactions of the ASME, Vol. 107,1985, pp. 8-16

[3] S. Chiaverini, B. Siciliano and L. Villani, "A Sur- vey of robot interation control schemes with exper- imental comparison", *IEEE/ASME Transactions on Mechatronics*, Vol. 4, pp. 273-285, 1999.

[4] F. Caccavale, C. Natale, B. Siciliano, L. Villani,"Six-DOF impedance control based on angle/axis representation", IEEE Transactions on Robotics and Automation, Vol. 15, No 2, April 1999

[5] J. Craig, "Introduction to Robotics Mechanics and Control", *Pearson Education Int*. 3rd Edition, 2005.

[6] yesiloglu, S. M., 'High performance dynamical modeling of complex topology systems', ITU PhD Thesis,2007

[7] L. Sciavicco and B. Siciliano, "Modeling and control of robot manipulators", *London: Springer*, pp. 270-290, 2000.

[8] F. Caccavale, C. Natale, B. Siciliano, L. Villani, "Integration for the next generation - Embedding force control into industrial robots" IEEE Robotics and Automation Magazine, pp.53-64, September 2005

[9] R. Schiavi and A. Bicchi, "Integration of Active and Passive Compliance

Control for Safe Human- Robot Coexistence", *IEEE InternationalConference on Robotics and Automation*, Kobe, Japan, pp. 259- 264, 2009.

[10] B. Siciliano, L. Villani, "Robot Force Control", Kluwer Academic Publishers, pp. 36-46, 1999

[11] J. Gea, F. Kirchner, "Modelling and Simulation of Robot Arm Interaction Forces Using Impedance Control", IFAC Congress on Automatic Control,Seoul,Korea, 2008.

[12] P. Boyraz, C.Bora Yigit, B. H.Okan, "UMAY: A Modular Humanoid Platform For Education and Rehabilitation of Childran with Autism Spectrum Disorder", IEEE International Conference on Control (ASCC),2013 9th Asian, Istanul, Turkey, 23-26 June 2013.

VISUAL SERVO - CONTROL APPLICATION IN HUMANOID ROBOTS USING DEPTH - CAMERA INFORMATION

Arezou Rahimi[1], Cihat Bora Yigit*, Behnaz Hosseini[1], Pinar Boyraz*
***Mechanical Engineering Department, Istanbul Technical University**
[1]Control Engineering Department, Istanbul Technical University

Abstract

In this paper a new implementation approach for visual-servoing in ***six*** degrees of freedom (DOF) is described. In general approach of visual servo controls, the procedures of close loop image-based visual-servoing(IBVS) need depth information, which plays a crucial role in the overall algorithm performance. The depth information has to be obtained fast in each iteration for calculating the interaction matrix .The motivation of this paper is not similar to other visual servoing method, which use eye-in-hand method, using IBVS scheme which is adapted for an eye-to-hand configuration. The implementation is achieved with a optical depth sensor to control the position and orientation of its end effector. Obtaining the depth information directly from Kinect accelerates the solution, and reduces the computational cost of the control algorithm. The framework is implemented on the UMAY humanoid robot. The implementation on UMAY is performed using the ROS as software architecture. The results presented show simulations on Gazebo. The robot is tested with different rehabilitation-play scenarios with the applied method.

Introduction

Humanoid robots are designed with a human form factor, which defines similarity between human and robot behaviors. The desire for this kind of design is rooted in the need to bring robots into everyday environment. Many of the earliest motivations for developing humanoids, centered on creating robots that can play a role in the daily lives of people. Today, humanoid robots are being developed to provide the elderly with assistance in their homes and to support medical care. To enhance the robot control performance, vision data are integrated into the robot control systems [2]. Visual servoing is a form of control that directly incorporates visual information into the control loop [1],[3]. Early works on using visual servoing for enabling a robot to grasp objects are reported in [4] and [5]. Since then, it has been utilized in much more complicated scenarios. The realization of robots similar to humans has been the goal of many research groups around the world. The replication of the human visual sense is one of the most important aspects of such goal. Humanoid UMAY aims to help incremental rehabilitation of children with Autistic Spectrum Disorders (ASD) utilizing its computer-vision interface as a core capability. Human-robot interaction and robot learning in UMAY need to use visual servo control as a sub-module to interact with its environment in a more controlled way. The visual sense is often lacking in many human-made machines. In fact, without visual information, manipulating devices can operate only in “structured” environments, where every object and its relative position and orientation is known a priori. With the increase of real time capabilities of visual systems, vision is beginning to be utilized in the automatic control as a powerful and versatile sensor to measure the geometric characteristics of the work piece. Visual servoing is a form of control that directly incorporates visual information into the control loop. Incorporating visual feedback makes it robust to errors that may come from a lack of calibration, system noise or the nature of the environment [1]. For these reasons, visual servoing is an attractive choice for performing manipulation tasks as opposed to open-loop approaches such as the one described in [3] .It is very well known that the depth information in visual-servo control is the most imperative one, especially in uncertain environments. Unlike other visual servo approaches, which use eye-in-hand or stereo configuration, the solution proposed here uses a depth camera that is located in the middle of torso of the robot. This is aimed to bring the advantage of calculation of the depth information with higher accuracy.

System overview:

The visual servoing framework has been implemented for UMAY Robot shown in Fig 1, UMAY is a humanoid platform that has 6 DOF arms, a special hybrid neck mechanism[10], and a moving base platform. Humanoid UMAY can be used in clinical therapies for the children with ASD using some rehabilitation tools or toys.

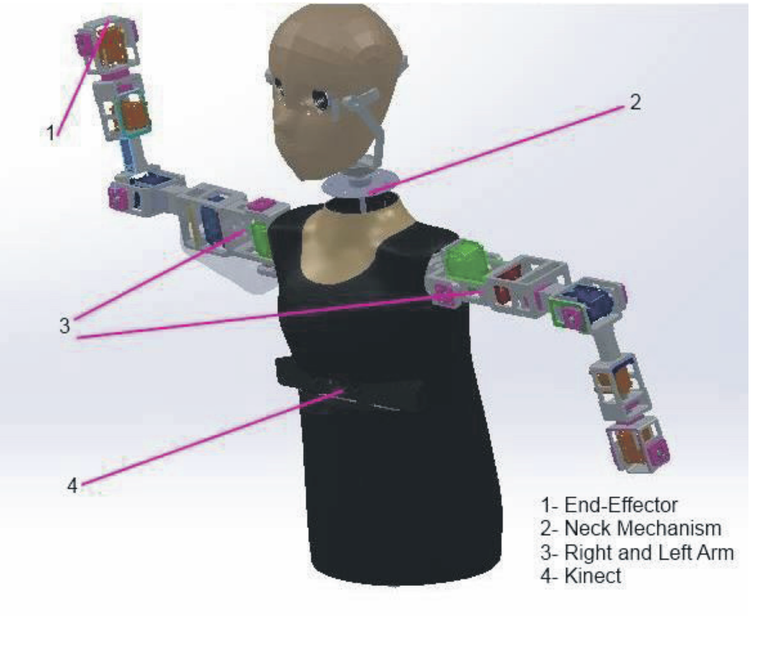

Figure1. An overview of UMAY robot with sensor positions indicated

In order to describe the kinematics and dynamics of robot Umay we use The Denavit-Hartenberg parameters as seen in Table 1.

i	Alpha (i-1)	a(i-1)	d(i)	teta(i)
1	0	0	0	T1
2	-90	0	20	T2
3	90	5	264	T3
4	-90	0	0	T4
5	-90	0	212	T5
6	90	0	0	T6

Table 1. D-H parameters of Umay

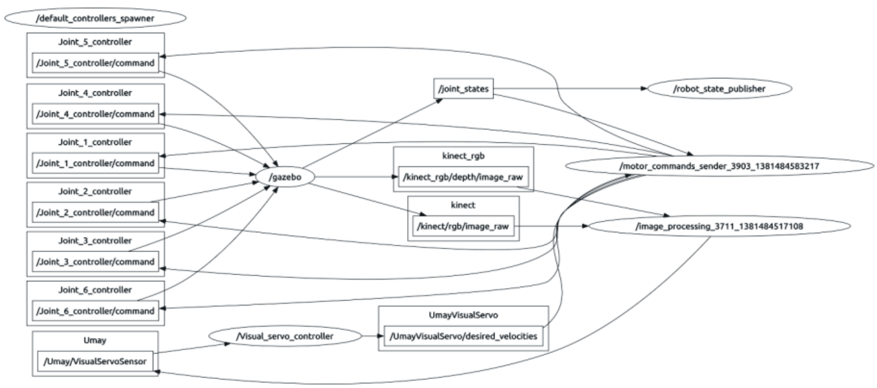

Figure 2

Simulation Environment

A computer with an Intel i5 processor and 4 GB RAM was used for the simulations described below. The operating system of the computer was Ubuntu 12.04 and runs Robot Operating System (ROS) (Groovy version) and Gazebo (1.5 version) as the dynamic simulator. C++, Python programming languages and OpenCV (2.6.1) computer vision library were used. The figure 2 shows the connection between the ROS nodes. Gazebo publishes the depth and RGB images which are taken from the simulated depth camera. In addition to this, Gazebo publishes the 'joint states' topic which includes kinematic states of the joints. Since the robot arm has 6 degree of freedom, there are 6 joint velocity controllers which can be seen from the left part of the figure. 'Image processing' node, subscribes the RGB images topic and finds the red object and green end effector. It publishes the coordinates in image frame. 'Visual_servo_controller' node implements the IBVS controller which is explained in this paper. 'Motor_commands_sender' subscribes the joints states in order to calculate

Jacobian matrix and visual servo controller for taking the desired velocities of the end effector. It calculates the velocities of all motors. Joint controllers control the motors speeds. The depth camera runs on 1 Hz and other nodes run on 100 Hz. 'message filters' library was used for synchronization of depth and RGB images.

Visual servoing

Image-based visual servoing (IBVS) uses direct image measurements as feedback to control the motion of the robot. The robot's positioning task is expressed as an image-based error function to be minimized using a suitable control law. In terms of manipulation, one of the main motivations for incorporating vision in the control loop was the demand for increased flexibility of robotic systems. Image based visual servo control uses image features derived from image plane and the servo controls them to a desired goal configuration. Even if new visual features were proposed, point features still remain the most used image measurements in designing visual servo control laws. Usually these measurements comprise the coordinates of the centroids or corners that describe an object. Purpose of any image based control architecture is to drive a robot system using information acquired by a visual sensor [2]. Therefore, the main goal of the image based visual servoing is to control the end-effector of a robot arm such as a set of image features to reach a desired configuration. If the considered robot system is a manipulator robot that has a video camera mounted on the gripper then a visual servoing structure with an eye-in-hand configuration is formed. In order to achieve the main goal, a trajectory for the video camera must be designed. The trajectory is given by the integration of the camera velocity obtained from the IBVS architecture by minimizing the error between the current point features configuration and the desired one [7-8]. The error between point features in the image plane is defined as in (1):

$$e(t) = s(m(t),a) - s^* \quad (1)$$

The parameters in (1) are defined as follows: The vector $\mathbf{m}(t)$ is a set of image measurements (e.g., the image coordinates of interest points or the image coordinates of the centroid of an object). These image measurements are used to compute a vector of k visual features, $\mathbf{s}(\mathbf{m}(t),\mathbf{a})$, in which $\mathbf{a}$ is a set of parameters that represent potential additional knowledge about the system (e.g., coarse camera intrinsic parameters or 3-D models of objects). The vector $\mathbf{s}^*$ contains the desired values of the features.Actually, there are two fundamentally different approaches to visual servo control: Position-Based Visual Servo (PBVS) and Image-Based Visual Servo (IBVS). Position-based visual servoing uses observed visual features, a calibrated camera and a known geometric model of the target to determine the pose of the target with respect to the camera. The robot then moves toward that pose and the control is performed in task space which is commonly *SE* (3). Good algorithms exist for pose estimation but it is computationally expensive and relies critically on the accuracy of the camera calibration and the model of the object's geometry. Image-based visual servoing, omits the pose estimation step, and uses the image features directly. The control is performed in image coordinate space R^2. The desired camera pose with respect to the target is defined *implicitly* by the image feature values at the goal pose. As IBVS methods, which utilize direct feedback from image features to motion control, have been proposed to handle many stability and reliability issues in vision-based control systems, we use this method in implementation of visual-servoing in UMAY as well.

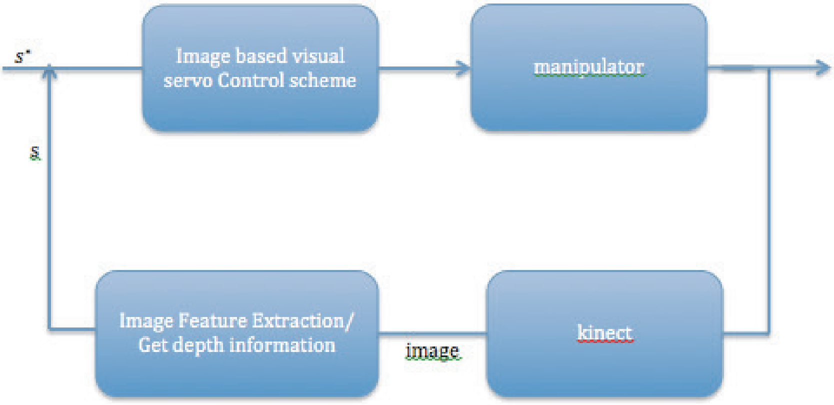

Fig3.Block diagram of visual servo control using kinect

From Figure 3 , we can see the IBVS takes the error from the two-degree image plane space. Let s be the current image feature observed by the camera and s* be the desired value of s to be reached.

If the task of extracting point features and finding the correspondences in the desired configuration are completed, then a relationship between time variation of s and end effector can be generated. Let v_c^* be a vector composed from linear velocities of the camera frame and the instantaneous angular velocities of the camera frame. The link between the motion of point features and camera velocity v_c is given by (2):

$\dot{s} = L_s \, v_c$ (2)

The L_s is the interaction matrix (namely called the image Jacobian matrix) related to s. It is well known that the Jacobian matrix plays an important role when we define the control laws. Based on the classical perspective projection model with a fixed focal length and the relation of the 3D point (X,Y,Z) in Euler coordination and the 2D image point (x,y) in image plane space, two successive rows of L_s are given by(3):

$$L_s = \begin{bmatrix} \frac{-1}{Z} & 0 & \frac{x}{Z} & xy & -(1+x^2) & y \\ 0 & \frac{-1}{Z} & \frac{y}{Z} & 1+y^2 & -xy & -x \end{bmatrix} (3)$$

Where L ∈ $R^{2n\times6}$ denotes the image interaction matrix of n point features [9] that compose the vector. In this work, we choose four points, so interaction matrix is 8x6. In this matrix, Z represents the depth of the image point (x,y) ,distance between end effector and desire object is unknown , thus the real value of Jacobian is obscure.

$$L_e = \begin{bmatrix} L_{s1} \\ L_{s2} \\ L_{s3} \\ L_{s4} \end{bmatrix} (4)$$

$\dot{e} = L_e V_c$ (5)

A classical proportional controller is defined [2] considering the static model of the velocities control loop, i.e $v_c = v_c^*$,from equation (5):

$v_c^* = -\lambda L_e^+ e$(6)

Where L_e^+ is the approximation of the pseudo-inverse of L_e .The output of the image-based controller is the reference velocity v_c^* of camera in eye in hand method. In this work, as we use eye to hand method we follow end effector and object in image plane of depth camera thus the output is Ve, velocity of end effector.

We have established the relationship between the velocity of individual joints and the translational and angular velocity of the robot's end-effector as follows**.** This equation describes the instantaneous forward kinematics where v = (v_x, v_y, v_z, ω_x, ω_y, ω_z) ∈ R^6 is a spatial velocity and comprises translational and rotational velocity components. The matrix ***J***(q) ∈ $R^{6\times N}$ is the manipulator Jacobian or the geometric Jacobian.

$$V = J(q)\dot{q} \ (7)$$

After finding velocity of the end effector using suitable controller, we should find velocity of each joint using (6):

$$\dot{q} = J^{-1} q_e (8)$$

In order to ensure better performances of a servoing system, different types of controller were used. Here we give a brief description of them;

As mentioned previously, there are different ways of defining the Image Jacobian. It can be defined in the current pose, and is then calculated using the current distances to the object. This is called Dynamical Image Jacobian L_n. It is a common alternative in using 2D cameras that is to define the true z in interaction matrix i.e. distance between initial position of end effector and desired object. This time the Jacobian is called the Constant Image Jacobian $L^{\star}$. Unlike L_n, $L^{\star}$ is constant over time and does not require image measurements for its adaptation to the current pose [6].

Finding z in each iteration using 2D camera is extremely costly and difficult in contrast to operating with depth cameras in which the calculation is drastically simpler. Using depth camera helps forming interaction matrix in a more computationally efficient way.

Simulation result for controller using Constant Image Jacobian:

The control problem can be expressed in terms of image coordinates. The task is to move end effector indicated by green square toward desired point indicated by red square. The points may, but do not have to, follow the straight line paths indicated by dot line. See Figure 4,6.

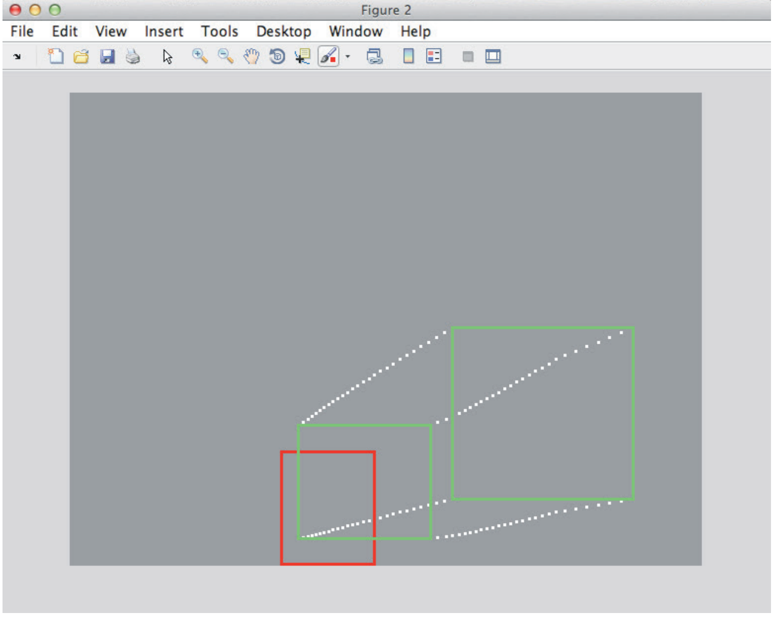

Figure4.Views of end effector trajectory using controller with Constant Image Jacobian

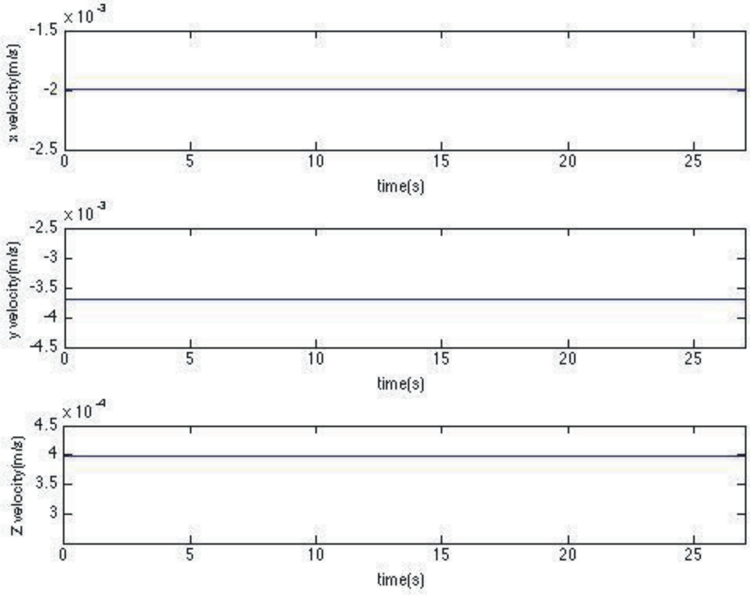

Figure5.velocity of end effector using controller with Constant Image Jacobian

Simulation result for controller using Dynamical Image Jacobian:

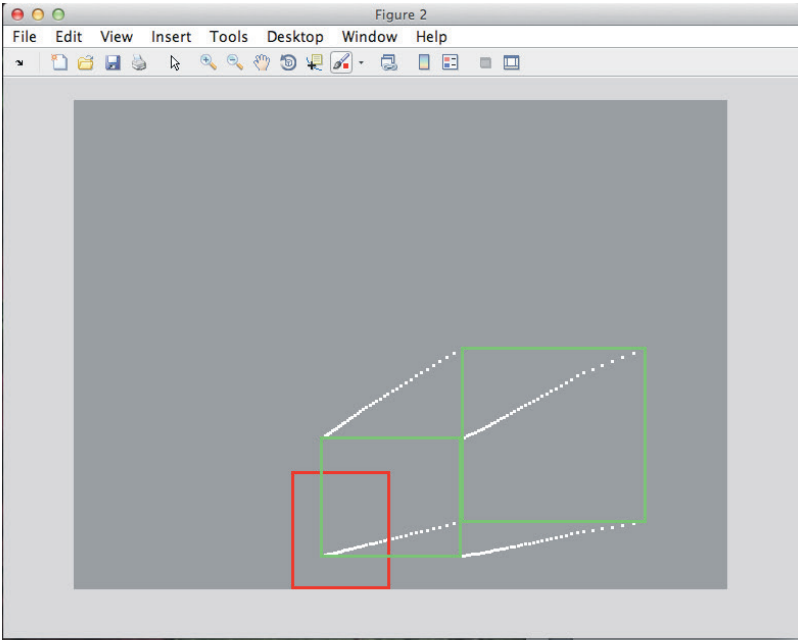

Figure6.Views of end effector trajectory toward desired point with Dynamical Z

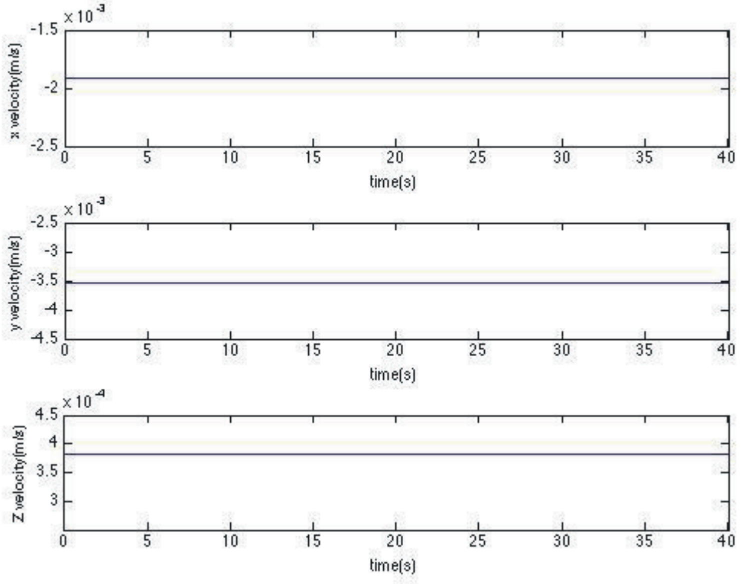

Figure7.velocity of end effector with controller
using Dynamical Image Jacobian

Screenshot of the simulation environment:

In Simulation the complete camera-robot system is modeled. This includes the complete Umay robot arm with inverse kinematics, rendering of the camera image in a realistic resolution and application of the image processing algorithms to obtain the image features. see Figure 8,9.

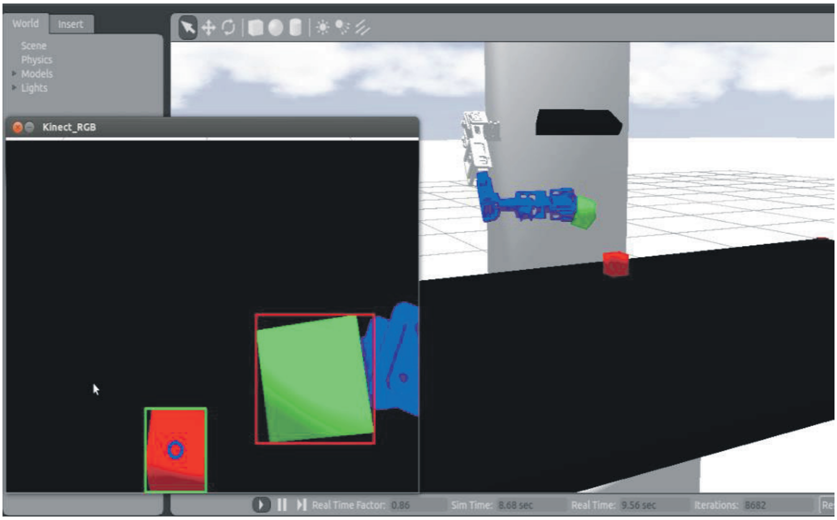

Figure8

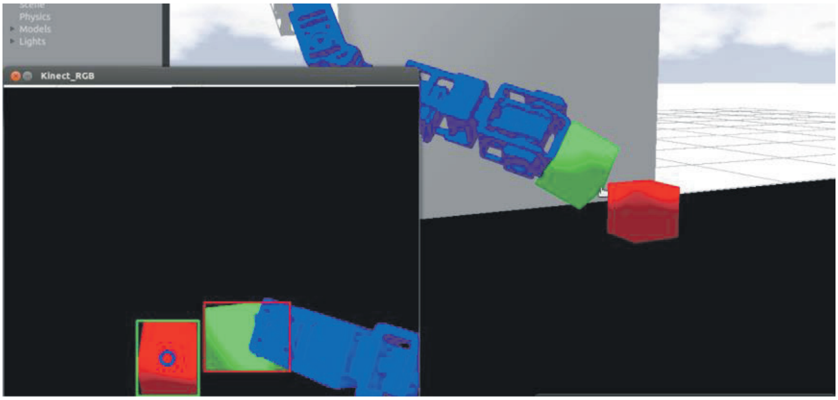

Figure 9.Simulation of optical depth sensor -robot system
with simulated depth camera image (bottom left)

As <u>you</u> see below end effector reaches the desire point, According to the given result , it can be said that the controller with Dynamical Image Jacobian L_n ,gives better result in compare to other controllers.

References

[1] F. Chaumette and S. Hutchinson, “Visual servo control, part i: Ba- sic approaches,” IEEE Robotics and Automation Magazine, vol. 13, pp. 82–90, December 2006.

[2] Visual Servoing for the REEM Humanoid Robot's Upper BodyDon Joven Agravante 1, J. Pages 2, François Chaumette ,IEEE Int. Conf. on Robotics and Automation, ICRA'13 (2013) 5233-5238

[3] S. Hutchinson, G. Hager, and P. Corke, “A tutorial on visual servo control,” IEEE Transactions on Robotics and Automation, vol. 12, pp. 651–670, 1996.

[4] R. Horaud, F. Dornaika, C. Bard, and B. Espiau, “Visually guided object grasping,” IEEE Transactions on Robotics and Automation, vol. 14, pp. 525–532, 1995.

[5] D. Kragic and H. I. Christensen, “Model based techniques for robotic servoing and grasping,” in IEEE/RSJ Int. Conf. on Intelligent Robots and Systems, IROS’02, (Lausanne, Switzerland), pp. 299 – 304, 2002.

[6] Improving vision-based control using efficient second-order minimization techniques,Ezio Malis I.N.R.I.A. Sophia Antipolis 2004, route des Lucioles, France

[7] P. Corke, "Visual Control of Robot Manipulators - A Review," in Visual Servoing, 1993, pp. 1-31.

[8] P. Corke, Visual control of robots : high-performance visual servoing vol. 2. Taunton England ; New York, NY: Research Studies Press ; Wiley, 1996.

[9] J. T. Feddema and O. R. Mitchell, "Vision-guided servoing with feature-based trajectory generation [for robots]," Robotics and Automation, IEEE Transactions on, vol. 5, pp. 691-700, 1989.

[10]] P. Boyraz, C.Bora Yigit, B. H.Okan, ”UMAY: A Modular Humanoid Platform For Education and Rehabilitation of Childran with Autism Spectrum Disorder”, IEEE International Conference on Control (ASCC),2013 9th Asian, Istanul, Turkey, 23-26 June 2013

INDUSTRIAL APPLICATION OF ANALYSIS AND VIBRATION MONITORING OF ROTATING MACHINES. PRACTICAL CASE

OUALI Mohammed [1, a] , MAGRAOUI Rabah[2,b] , MEGHATRIA M'Hamed[3,c]

[1, 2 , 3] Structural Mechanics Research Laboratory, Department of Mechanical Engineering

University Saad Dahlab, Blida, Algeria

[a] oualimohammed@yahoo.fr. [b] r.magraoui.labstructures.usdb@gmail.com

[c] m_ghatria@yahoo.fr

The corresponding author: Mohammed Ouali[1, a] , oualimohammed@yahoo.fr

Keywords: Preventive maintenance, vibration analysis, rotating machines, wear , bearing fault , unbalance.

Abstract: Today with software design and diagnostic methods for malfunctions of machines and availability of computer tools, industrial came to exploited the machine at a time maximum, with a guarantee of zero failures. And, by monitoring of rotating machinery and maintenance management cost.

In this paper, we present applications of industrial signal processing techniques used in vibration diagnosis and early detection of rotor imbalance, which leads eventually to the emergence of other mechanical defects, namely: The wear and bearing fault. We first present methods for spectral analysis of high resolution, using a data collector vibration for vibration measurements (levels and signature). Then, we present an analytical method for the detection of mechanical or electrical defects that may arise during the operation of the facilities. Powerful software is used to load the routes machines. The measures identified experimentally are compared with those of the literature.

An application was made on an industrial machine: a shredder.

Introduction

Condition monitoring by vibration analysis prevents premature the appearance of defects with a true state of the machine at any time. It allows programming of interventions and repairs on the machines. The vibration monitoring is provided by vibration measuring devices with whom the monitoring of rotating machinery is ensured with periods determined by their states based on international standards. This monitoring technique identifies the mechanical or electrical failures that may occur during operation of the machine, such as defects:- bearing, wear, alignment, gearing, unbalance (imbalance of rotors, fans, ...) of flexion, transmissibility of vibration structures, the electromagnetic motors (eccentricity of the magnetic field, wear plates, electrical interference, ...). We can also mention the malfunction of some rotating machines: centrifugal pumps, fans ventilator,...

In this work, the early detection of anomalies is due to the spectral interpretations.

The spectra are provided by a data collector and vibration analyzer MOVILOG 2 which is associated with its PC DIVADIAG predictive maintenance software. This allows also to deepen the spectral analysis of signals and detection precision of the source of anomalies which cause vibrations. [1]

Application:

We intend to present a case study lived in a factory hygiene baby products: paper shredder.

We will not insist on the theoretical side because it has been the subject of recent research [2,3,4,5,6]. We insist more on the experimental part. We will proceed to results confrontations between theory and experiment. We proceed directly to the application by citing the essential formulas.

1. Description of the machine :

The shredder is a cutting mill located in the preparation area in a factory hygiene products. The machine consists of an asynchronous electric motor turning 2985 rpm / min and power of 90 kW, the movement is transmitted by a belt with two driving and driven pulleys to a line shaft supported by two bearings separated bearings and supporting a shredder comprising a shaft on which are mounted the knives (see photo 1-2), rotating at the speed of 3300 rev / min (see Figure 1-1).

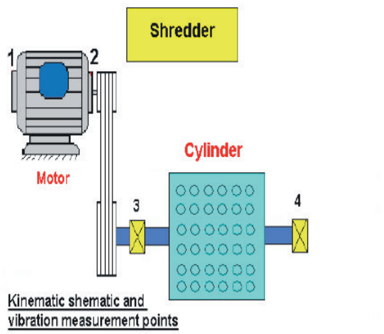

Figure 1-1

Photo 1-1

Photo 1-2

Principal theoretical formulas [2, 3, 4,5,6] :

We consider a system of bearings supporting the rotor. By modeling the rotor-bearing, after some mathematical considerations, we obtain the own pulsation ω_0, ..., the damping ratio of Lehr , the maximum amplitude of the movement X , the maximum range of motion, the ratio $\frac{X}{|e|}$ for different regimes,... we give:

$$\omega_0 = \sqrt{\frac{k}{(m_r + m_p)}} \qquad (1)$$

$$A = \frac{a}{2 \bullet \sqrt{k.(m_r + m_p)}} \qquad (2)$$

$$\frac{X}{|e|} = \frac{m_r \bullet \omega^2}{k} \qquad (3)$$

$$\frac{X}{|e|} = \frac{1}{\frac{(m_r + m_p)}{m_r}} \qquad (4)$$

- When the rotational speed of the rotor is lower than the resonant frequency of the support, then: the whole behaves as if the bearings were very rigid and we obtained (3).

- When the rotational speed of the rotor is higher than the resonant frequency of the support, the whole behaves as if the bearings were very flexible, the inertia forces in the system are larger than the limited resilient forces exerted by the suspension which may be neglected (4).

m_r : mass of the rotor, m_p : parasite mass, k : rigidity of the support (N / m), a : damping of support (N / m.s), X : maximum amplitude of movement (μm), eccentricity $|e|$, pulsation ω.....

This shows that, if the vibration sensors measure the movement of the bearings as representative of the eccentricity, the relationship between the parasite and the mass of rotor mass is minimized to achieve greater sensitivity. When the speed of the rotor coincides with the natural frequency of the support, the elastic inertia forces are in opposite phases and the same amplitude. The amplitude of the radial displacement is then related to the amortization period. If the damping is small, the dynamic effect can produce significant radial displacements.

3. Historic [4] :

The shredder is a strategic machine in the production line of the factory.

Control by the technique of vibration analysis is started: January 10, 2010, following the onset of machine vibration. The interpretation of spectral measurements on the machine revealed the presence of an imbalance in the rotor bringing the shredder as indicated by the dominant amplitude component related to the frequency of rotation - spectra taken on two levels No. 03 and 04 in both horizontal and vertical radial directions (figures 3-1, 3-2, 3-3, 3-4), generating a vibration level of 08.85 mm / s in the bearing 03 in the horizontal radial direction. According to international standards VDI 2056 Alarming tried this. For this purpose, it was monitored periodically by the method of vibration analysis during thirty days (curves 3-5 tend to 3-10) to follow the evolution of the defect and the potential risks caused it in the appearance of a possible failure: default bearing, bearing wear, ..., which may eventually generated the unexpected shutdown of the production tool.

The machine has been programmed to stop more to balancing on the rotor of the shredder after recording several imbalance (Table 3-1). The most important was held November 5, 2011 and on July 29, 2012. We have detected a global level respectively 44.01 mm / s and 48.18 mm / s on bearing No. 04 in the vertical direction, according to the trend curve No. 3-10. Also, the bearing problems have arisen repeatedly in the system. The ball bearings have been changed as a result of default of imbalance or default of greasing ...

Date of intervention	Unbalance level before balancing (mm/s)	Unbalance level after balancing (mm/s)	Date of intervention	Unbalance level before balancing (mm/s)	Unbalance level after balancing (mm/s)
May 23, 2011	29.44	06.13	March 10, 2012	21.30	02.09
November 5, 2011	43.80	04.52	July 31, 2012	25.20	02.39
November 27,2011	16.80	01.85	October 1, 2012	37.88	03.16

Tableau 3-1 Unbalance level before and after balancing.

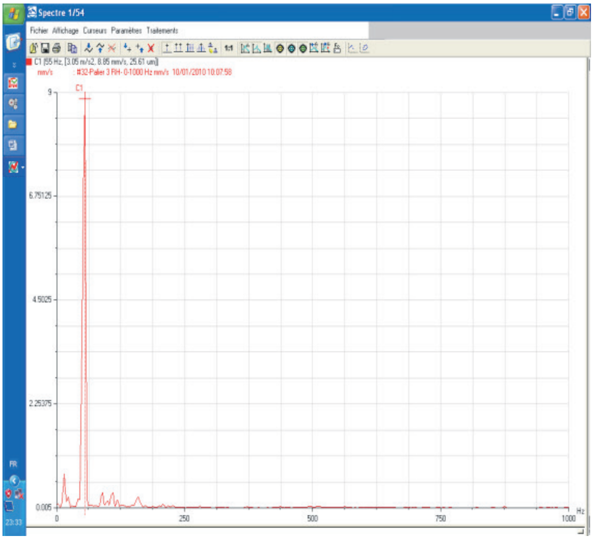

Figure 3-1 : Spectrum of 10/01/2010 on the motor landing No. 03 in the horizontal radial direction.

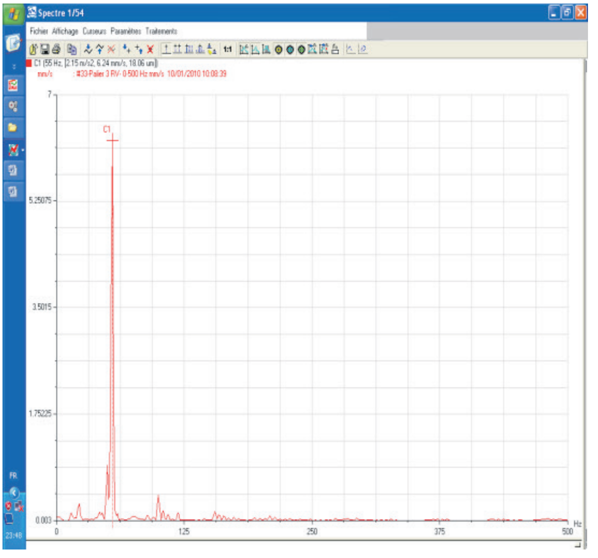

Figure 3-2 : : Spectrum of 10/01/2010 on the landing No. 03 in the vertical radial direction.

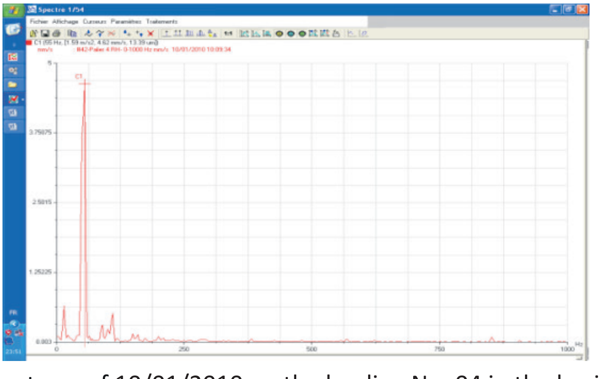

Figure 3-3 Spectrum of 10/01/2010 on the landing No. 04 in the horizontal radial direction.

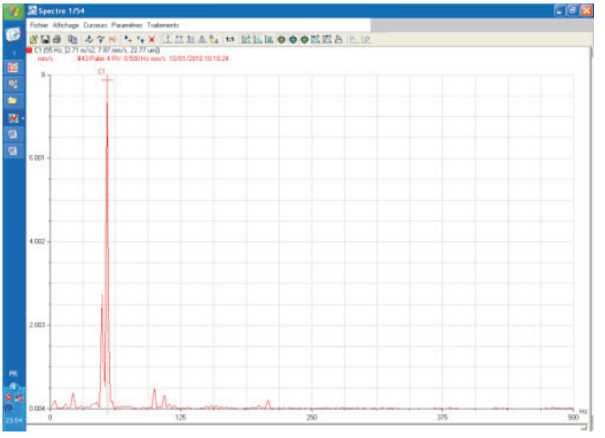

Figure 3-4 : Spectrum of 10/01/2010 on the landing No. 04 in the vertical radial direction.

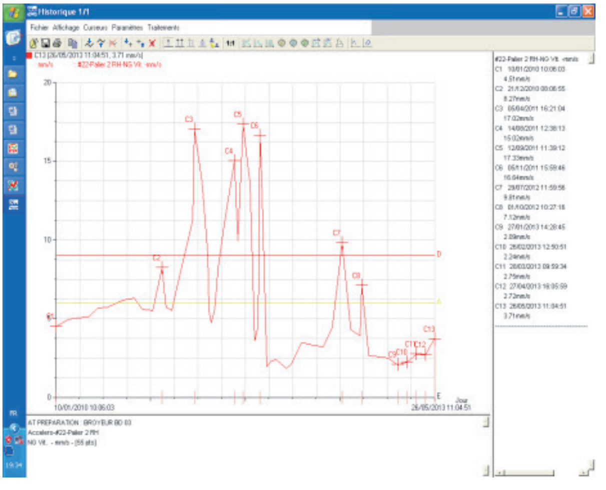

Figure 3-5 Trend curve taken on the motor bearing in the horizontal direction.

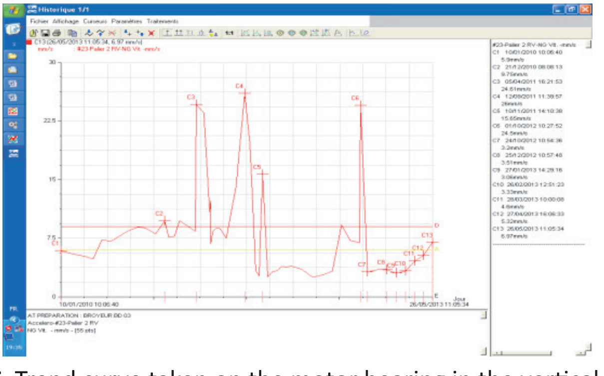

Figure 3-6 Trend curve taken on the motor bearing in the vertical direction

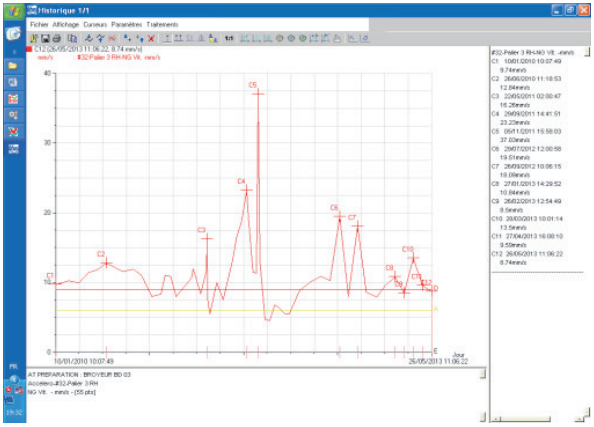

<u>Figure 3-7</u> Trend curve taken on the bearing No. 03 in the horizontal direction.

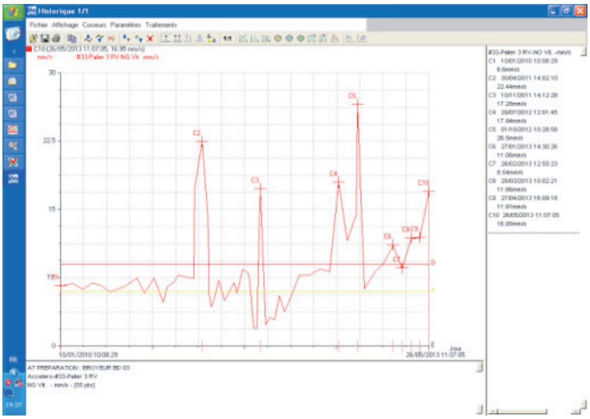

<u>Figure 3-8</u> <u>Trend curve</u> taken on the bearing No. 03 in the vertical direction.

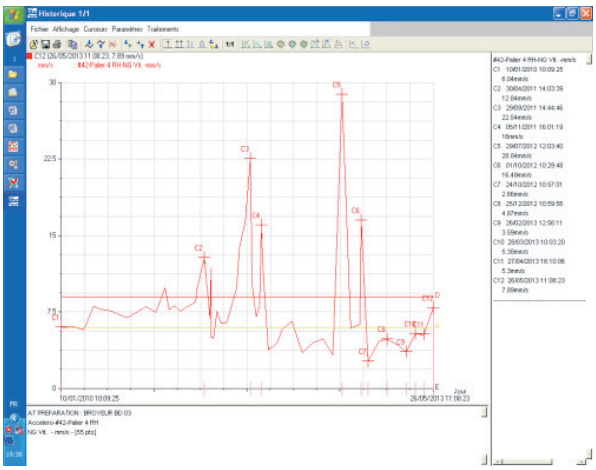

<u>Figure 3-9</u> Trend curve taken on the bearing No. 04 in the horizontal direction.

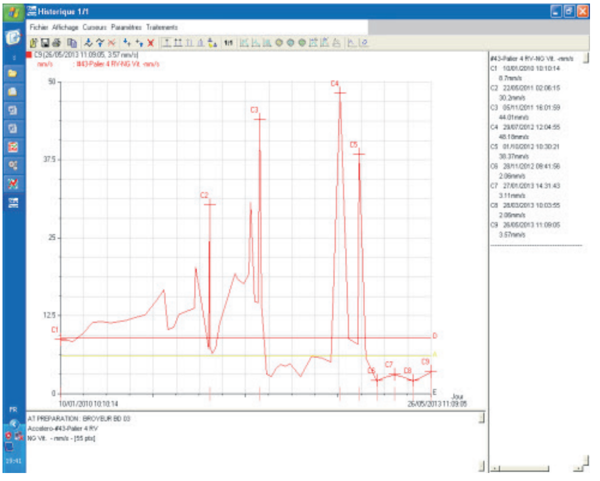

Figure 3-10 Trend curve taken on the bearing No. 03 in the vertical direction.

4- Diagnostic. [2, 3, 4,5,6, 7,8] **Analysis results:**

During periodic monitoring by vibration analysis, diagnosis reveals the presence of a fault on the rotor unbalance bringing knives of shredder. Other anomalies may occur: The bearing fault of both bearings No. 03 and 04, as well as the defect of usury . We will consider these cases as follows:

4-1 Imbalance fault: The imbalance is a rotary centrifugal force which occurs in the rotational frequency of the rotor (turbine), it causes vibrations in a radial planes. If we consider the case where the imbalance is a scale (5 November 2011), where the spectral interpretation of vibration measurements allows us to detect the presence of an imbalance in the rotor shredder, generating a vibration level of 3664 mm / s in the spectrum of Figure 4-1 taken from the bearing No. 03 in the horizontal radial direction, and 43.80 mm / s on bearing No. 04 in the vertical radial direction from the spectrum in Figure 4-4, as indicated by the amplitude of dominant component related to the frequency of rotation of the rotor is 52 Hz for this purpose, we recommend balancing the rotor, which is place in two (02) plans to remove the couple unbalance for the large width that represents the rotor, as we veered later in the correction part. Unfortunately, this machine several known imbalance that led to the emergence of other mechanical defects, namely: failure to wear or play on the bearing surface, bending the shaft carrying the shredder misalignment between levels and a bearing fault in both bearings. In this case, we will see some anomalies accompanying the default of imbalance.

4-2 Failure to wear: This fault has occurred on several occasions. On July 17, 2011, we have detected an impact on the shaft carrying the rotor shredder line presented by a comb lines whose components are of order 2, 3, 4, ..., spaced apart from the fundamental frequency of 52 Hz, as shown in all spectra programmed to 500 Hz, taken on two bearings No. 03 and 04 in the vertical radial direction, respectively shown in Figures 4-5 and 4-6. Therefore, measures have been taken to stop the program and change the bearings of the installation.

4-3 Bearing fault: The bearing fault is is clearly seen when taking measures overall vibration level expressed in acceleration, reaching and sometimes exceeding the danger threshold arriving until 20 g (g = 9.81 m/s2). This defect causes a shock to the tree line with the shredder (case of 24 April 2012), where we comb lines whose components are of order 2, 3, ..., spaced apart from the fundamental frequency of 272 Hz of the spectrum taken on two bearings No. 03 & 04 in the horizontal radial direction of a frequency band of 500 Hz (see Figure 4-7 and 4-8) which is a bearing fault type - flaking roller elements . Both bearings were changed just after our recommendations.

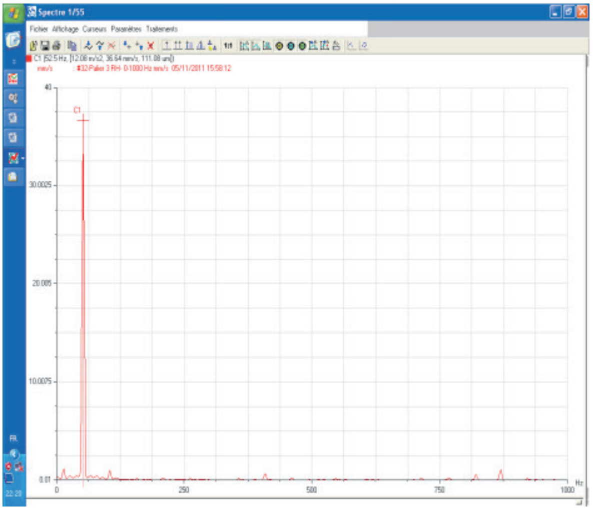

Figure 4-1 Spectrum taken on: November 5, 2011 on the bearing No. 03 in the horizontal radial direction.

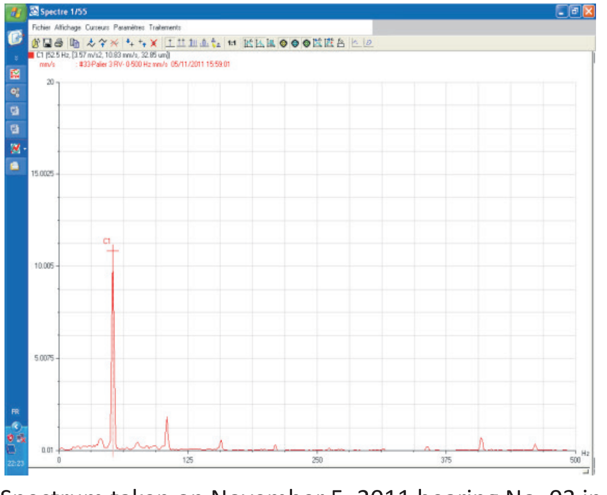

Figure 4-2 : Spectrum taken on November 5, 2011 bearing No. 03 in the vertical radial.

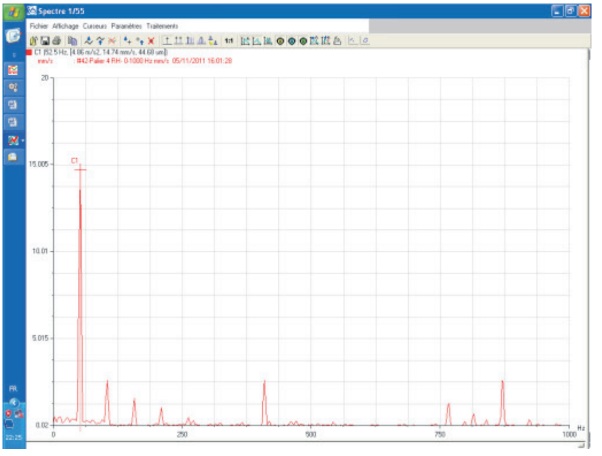

Figure 4-3 : Spectrum of 5 November 2011 on the bearing No. 04 in the horizontal radial direction

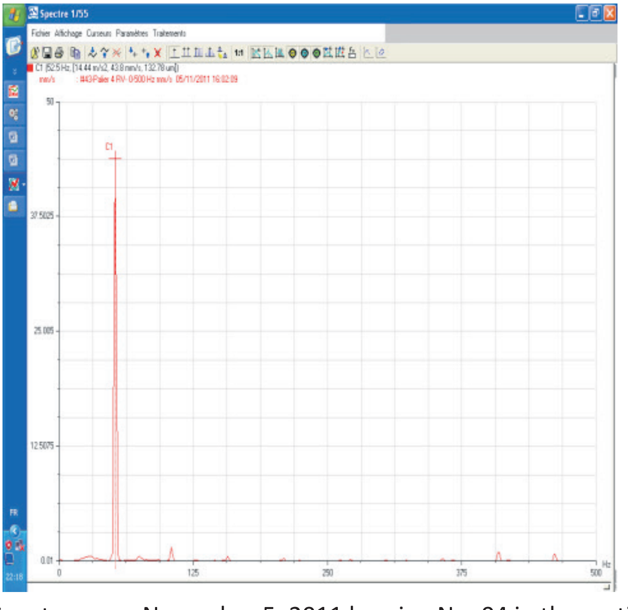

Figure 4-4: Spectrum: on November 5, 2011 bearing No. 04 in the vertical radial direction.

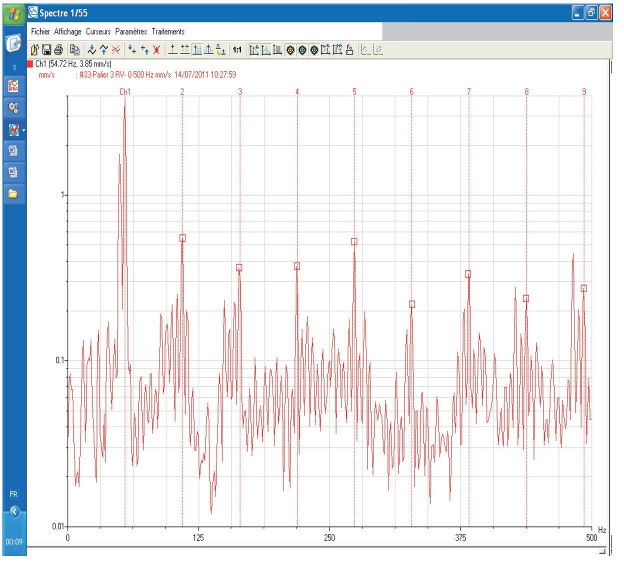

Figure 4-5: Spectrum taken: 14/07/2011 on the bearing No. 03 in the vertical radial direction.

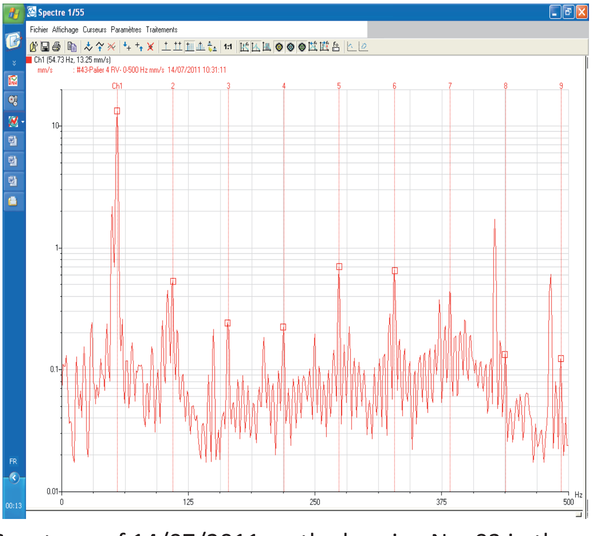

Figure 4-6: Spectrum of 14/07/2011 on the bearing No. 03 in the vertical radial direction.

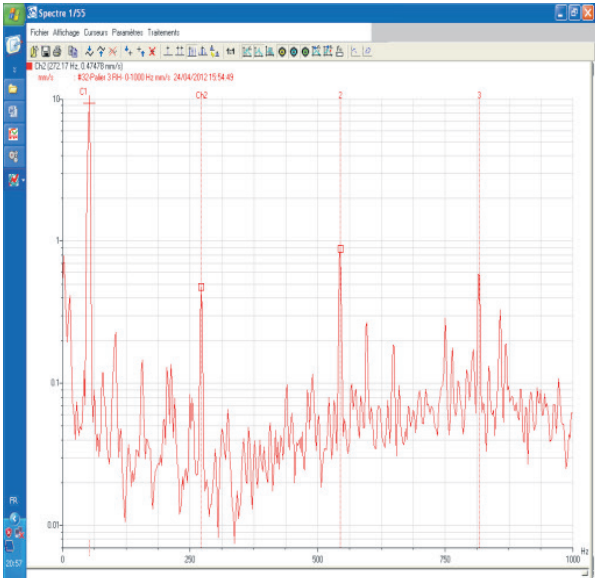

Figure 4-7: Spectrum taken: 24/04/2012 on the bearing No. 03 in the horizontal radial direction.

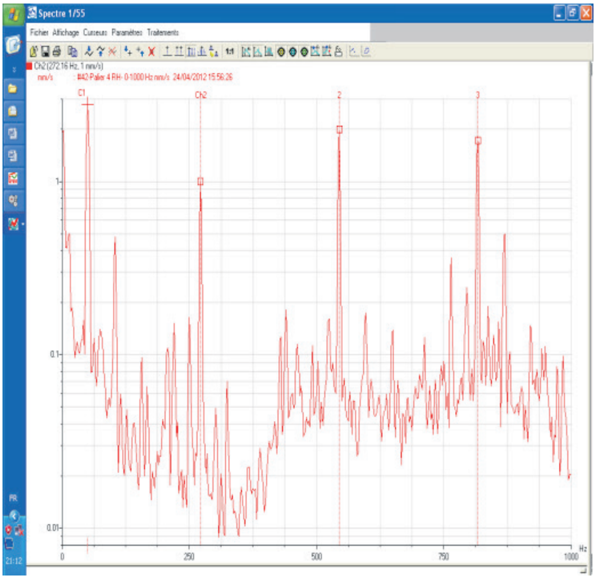

Figure 4-8: Spectrum taken: 24/04/2012 on the bearing No. 04 in the horizontal radial direction.

5. Correcting the imbalance

Will thus induce an unbalance in a radial plane on a vibration spectrum which has a dominant frequency the amplitude of rotation of the rotor component. Usually this feature is seen more clearly on a spectrum from a measurement taken radially

Many defects are expressed by a prominent component of high amplitude related to the frequency of rotation is phase analysis that distinguishes between defects from a turning effort as the unbalance, and defects from a directional effort (non-rotating) as induced by a belt too tense, bearing wear, a unclamping bearing stress, eccentricity pulley, ... etc.

Indeed, for two points located at radial measures 90° on the same level, the phase shift between frequency components equal to the rotation frequency (order component 1) is:

• close to 90 °, in the case of a fault associated with a rotary force as the unbalance.

• Close to 0 ° or 180 ° in the case of a fault related to a directional effort.

Also, we must distinguish between static and dynamic unbalance. In the case of a static unbalance the two bearings supporting the rotor will experience, at the same time, the centrifugal force due to the imbalance. It will have no phase shift between the measurements taken at the same point on both levels. While in the case of a dynamic imbalance, the two bearings supporting the rotor will experience centrifugal forces (alternately). The phase (close to 180°) between the measurements at the same point on two consecutive bearings and therefore indicative of an dynamic imbalance. [2] The dynamic imbalance is still sanctioned by a correction on two balancing planes : October 1, 2012, or measures vibration levels and phases when balancing are shown in the two tables 5-1 and 5-2.

The balancing method is composed of several launched performed on two bearings supporting the rotor. The pulley receiving side (No. 03) is the balancing plane No. 01. The open side of the bearing (No. 04) is the balancing plane No. 02. The first one launched is initiated to make the measurements of vibration level with the phase without proof mass, said second is carried out with a test block according to the calculated rotation speed of the rotor to be balanced, and its radius of its weight, and launched last will be made with the mass and correction of in the calculated position. Measurements are taken from the two above bearings indicated in the same time.

Sometimes this mass (of correction) with its position does not give the value of the desired level of vibration, so we will be forced to improve the correction by a refining operation. The rotor consists of 16 part (phases or angles). The procedure is summarized in the following two tables:

launched	Mass(gr)	Horizontal measures	
		levels(mm/s)	Phase
N°01	-	26,812	07,760
N°02	80 gr Position 0	34,490	08,910
N°03	Correction : 155,45 gr Position : 0,41	04,741	06,415
Refining	103,52 gr Position : 01,15		

Table 5-1 Measurements carried out on the bearing No. 03: October 1, 2012.

Launched	Mass(gr)	Vertical measures	
		levels(mm/s)	Phase
N°01	-	37,880	02,960
N°02	80 gr Position 0	16,549	04,352
N°04	Correction : 218,82 gr Position : 12,35	03,166	
Refining	70,426 gr Position : 11,64		

Table 5-2 Measurements carried out on the bearing No. 04: October 1, 2012

6. Validation of Results for the Shredder

6.1 Measurements on the plan No. 01 on the bearing No. 03 **(Table 1**).

Measurements on the plan No. 02 on the bearing No. 04 **(Table2**).

According to the method of calculating the MOVILOG 02, the results are measured in RMS.

	vibratory displacement (m)	vibratory speed (mm/s)
Theoretical values	**$8.022\ 10^{-5}$**	**26.20**
Experimental values	**$7.819\ 10^{-5}$**	**26.818**

Table 1 Theoretical and Experimental values of shredder - bearing No. 03

	vibratory displacement (m)	vibratory speed (mm/s)
Theoretical values	$1.1088\ 10^{-4}$	36.20
Experimental values	$1.1315\ 10^{-4}$	37.880

Table 2 Theoretical and Experimental values of shredder - bearing No. 04

Conclusion:

The shredder requires a vibration monitoring. This increases availability and

can plan interventions for possible repairs. In addition, vibration monitoring can track the fault and arrange for supply of spare parts. Vibration analysis has enabled us to diagnose mechanical failures and propose solutions to overcome them. Note that our advice is not always followed, which can have catastrophic consequences for the various machines and facilities, causing nuisance shutdowns of manufacturing plants. The vibration analysis helps not only to accurately detect these problems, but also to control the mounting during the installation of some new machines. The vibration analysis, allowed us to balance the rotor shredder...

The results of the experiment (on the machine) have been checked and compared with the results of the theory.

References

[1]. Framatome Diagnostic- Jean de MANS- *Le diagnostic vibratoire au service de la Maintenance Réf : 104-1.* LYON 1992.

[2]. M Dougdag, M.Ouali, 2010, A simple and compact model of defects and non-linear dynamic stiffness of a ball bearing, *Mecanique et Industries*, vol. 10, no 6, p. 525.

[3]. M Dougdag, M.Ouali, 2011, An experimental testing of a simplified model of a ball bearing: stiffness calculation and defect simulation- Meccanica, Springer ISSN 0025-6455,Meccanica

[4]. M.Ouali, R.Magraoui, *Contribution à la maintenance conditionnelle par l'analyse vibratoire. Défaillances mécaniques et solutions proposées,* 10th Mechanical Congress Oujda Maroc, 19 au 22 avril 2011

[5]. M.Ouali, R. Magraoui, *Contribution à la maintenance conditionnelle par l'analyse vibratoire. Contrôle vibratoire des machines tournantes, avril 2011,* 10th Mechanical Congress Oujda Maroc,19- 22.

[6]. M Dougdag, M.Ouali, Introduction of mass points into the finite element method for the dynamic behaviour modeling of rotating , 2012, Proceedings of the ASME 2012 International Mechanical Engineering Congress & Exposition IMECE2012 November 9-15, Houston, Texas, USA. IMECE2012-87485

[7]. Philippe Arquès. Professeur des Universités. *Ecole centrale* de Lyon-

Diagnostic prédictif de l'état des machines, Edition MASSON 1996.

[8]. *Les défauts des machines. Les défauts des engrenages Encyclopédie pour formation en maintenance préventive 1993.*

PREDICTIVE VIBRATIONAL DIAGNOSTICS OF ROTATING MACHINES VENTILATOR ATOMISER APPLICATION

MAGRAOUI Rabah[1, a] , OUALI Mohammed [2,b] , TEMMAR Mustapha[3,c]

[1, 2, 3] Structural Mechanics Research Laboratory, Department of Mechanical Engineering

University Saad Dahlab, Blida, Algeria

[a] r.magraoui.labstructures.usdb@gmail.com ,

[b] oualimohammed@yahoo.fr, [c] temmar_m@yahoo.fr

The corresponding author: MAGRAOUI Rabah[1], r.magraoui.labstructures.usdb@gmail.com

Keywords: Conditional maintenance, vibration, modeling , rotating machines , unbalance.

Abstract.

In recent years, engineers have focused on vibration problems of industrial machines and they studied the isolation or the reduction of the vibration. The deterioration of these machines leads to their unavailability, resulting in a loss of production, costs of major maintenance, noise and vibration. Therefore, it is more important than necessary for their monitoring and diagnostics. Vibration analysis of rotating machines can better perceive the dynamic phenomena. Vibration measurements and analysis of the signal do not require stopping the machine. A control of vibration analysis requires knowledge of measurement tools and the ability to interpret the results of diagnosis. Vibration analysis can detect not only the mechanical or electrical defects that may arise during operation of the facility, but also the design flaws of these installations, particularly resonance phenomena.

The aim of our work is to study the vibratory behavior of strategic equipment in an industrial factory. Also, we modeled the actual equipment and replaced by a theoretical mathematical model and numerical model for the determination of the equations of motion of the system and solutions that will be confronted with those of the practice like with the own pulsations of this system.

Introduction

Monitoring of rotating machines by vibration analysis was developed in the 1970s. The advent of electronic data collectors gave a boom not only to the periodic monitoring of machines, but also to the early detection of mechanical or electrical defects that may arise during operation. The development micro-computer has also provided the maintenance investigative which was very considerable. During our work, we propose to study the vibrational behavior of a fan sprayer Draw in ceramic industry.

The vibration monitoring brings knowledge of the actual state of the machine at any time early enough to prevent the occurrence of a fault and can track its evolution to manage maintenance. The role of vibration monitoring is not to limit the damage but to estimate the running time allowed before any damage to provide the necessary maintenance [1].

This work shows early fault detection by spectral interpretations provided by a data collector and vibration analyzer that is associated with its software. The spectral analysis of signals and the precise detection of the source of anomalies which cause vibrations are studied. Proposals are suggested and appropriate solutions are made.

Analysis and study: a practical case

We intend to present a case study lived in a ceramic industry: Fan atomizer **(Fig. 1-1 and 1-2)**

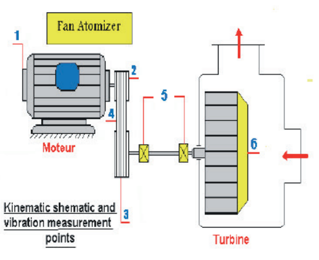

Figure 1-1

Figure 1-2

Fan atomizer -ceramic industry

1. Description of the machine:

The atomizer is a fan for extraction of the material constituting the ceramic slurry in a spray chamber. It sucks the waste by evacuating as atomization gas through the chimney outlet Positioned on a suction line producing the ceramics line **(Fig. 1-1 and 1-2)**. The Machine Consists of an asynchronous electric motor at 1485 rev / min, and 90 KW power. The movement is Transmitted by belts with two driving and driven pulleys, to a piece Free-shaft supported by a roller bearing, and Supporting a suction turbine with a diameter of 900 mm and width 290 mm, rotating at a speed of 1767 t / min, consisting of a single row of 11 vanes .

2- Equation of vibration behavior of the system [2, 3].

A system of bearings supporting a rotor is considered. Modeling the rotor-bearing as a system of one degree of freedom, the differential equation of motion may be expressed as [2,3,4]:

$$\left(m_r + m_p\right) \bullet \ddot{x} + a \bullet \dot{x} + k \bullet x = m \bullet |r| \bullet \omega_0^{2} \tag{1}$$

m_r : mass of rotor, m_p : parasite mass:, ω_0 : natural frequency of the rotor, k : rigidity of the support (N / m), a : damping of support (N / m.s), x : amplitude of the movemen (m, μm) and e is the eccentricity.

The maximum amplitude of motion X (μm), a solution of the differential equation (1) is:

$$\frac{X}{|e|} = \frac{m_r \bullet \left(\frac{\omega}{\omega_0}\right)}{(m_r + m_p) \bullet \sqrt{\left(1 - \left(\frac{\omega}{\omega_0}\right)^2\right)^2 + 4 \bullet D^2 \bullet \left(\frac{\omega}{\omega_0}\right)^2}} \quad (2)$$

$$\omega_0 = \sqrt{\frac{k}{(m_r + m_p)}} \quad (3)$$

and $$A = \frac{a}{2 \bullet \sqrt{k.(m_r + m_p)}} \quad (4)$$

$$C_r = 2 \bullet \sqrt{k.(m_r + m_p)} \quad (5)$$

A represents the amortization of Lehr [4] .In practice, the value of A is small.

For example and in in the case of a spring steel $A = 0.001$, and a rubber spring $A = 0.05$ [4]. The phase shift ϕ is expressed by:

$$\tan(\phi) = \frac{2 \bullet A \bullet \left(\frac{\omega}{\omega_0}\right)}{1 - \left(\frac{\omega}{\omega_0}\right)^2} \quad (6)$$

The different regimes are [4,5]:

- When the rotational speed of the rotor is lower than the resonant frequency of the support [6]: the assembly behaves as if the bearings were very rigid and the above equation can be written:

$$\frac{X}{|e|} = \frac{m_r \bullet \omega^2}{k} \quad (7)$$

- When the rotational speed of the rotor is higher than the resonant frequency of the support, then the whole behaves as if the bearings were very flexible, the system of inertial forces are larger than the resilient forces exerted by limited the suspension [6] which may be neglected, therefore :

$$\frac{X}{|e|} = \frac{1}{\frac{(m_r + m_p)}{m_r} \bullet \left(\left(\frac{\omega}{\omega_0} \right)^2 - 1 \right)} \tag{8}$$

Equation ((9), for $\omega_0 << \omega$ and after simplifications, takes the form:

$$\frac{X}{|e|} = \frac{1}{\frac{(m_r + m_p)}{m_r}} \tag{9}$$

This shows that if the vibration sensors measure the movement X of the bearings as representative of the eccentricity $|e|$, then the relationship between parasite mass and the mass of the rotor is minimized to obtain a higher sensitivity.

When the speed of the rotor coincides with the natural frequency (own) of the support, and the spring forces of inertia are in opposite phases and have the same amplitude. The amplitude of the radial displacement is then linked to the damping term A .

If the damping is small, the dynamic effect can produce significant radial displacements.

3- Historic [4]

The Atomizer is a strategic machine in the production line- start in June 2008. The machine operated under normal conditions, without vibration, until our intervention on: July 22, 2008, where we were informed by the maintenance team, that it was a vibration problem resulted in this fan.

Our initial diagnosis revealed the presence of an imbalance of the turbine, generating a vibration level of 15.04 mm / s on the shaft bearing on the turbine -side turbine- (No. 04 from Figure No. 1-1), this level is considered Danger(international standards VDI 2056).

We proceeded to balancing the turbine, correcting the imbalance, and to decrease the vibrations caused by the latter up to 01.55 mm / s.

This fan has had several defects imbalance during operation, and every time we intervened to solve this problem (see curves of trend N°3-1, 3-2, 3-3, 3-4, 3-5 et 3-6). After having eliminated the possibility of existence of other defects, we had to repeatedly perform balancing operations are shown in Table 3-1.

To this end, just before the last balancing operation December 20, 2012, an intervention to change both bearings shown above is achieved. Unfortunately, the monobloc was not changed as we have recommended.

Intervention	Unbalance level before equilibration (mm/s)	Unbalance level after equilibration (mm/s)	Intervention	Unbalance level before balancing (mm/s)	Unbalance level after balancing (mm/s)
July 23, 2008	15.04	01.55	October 14, 2010	08.59	01.02
March 24, 2009	09.28	01.18	October 26, 2011	10.36	01.95
July 18, 2009	07.95	01.03	17 September 2012	30.02	02.44
August 22, 2009	25.02	02.59	October 29, 2012	26.18	02.30
March 17, 2010	07.14	01.89	December 20, 2012 Change bearings	18	01.94
August 8, 2010	09.09	02.21			

Table 3-1 Intervention- Recommandation

We give only some curves trending obtained

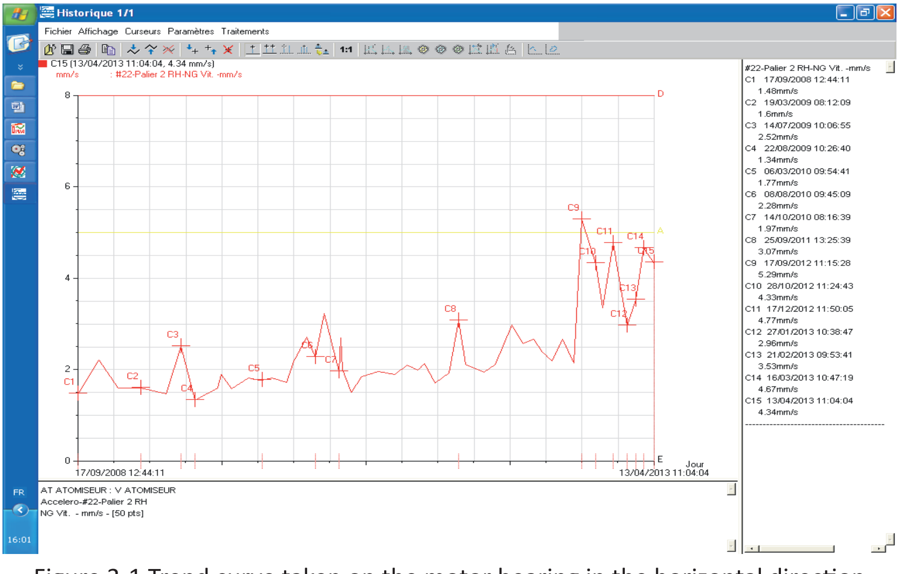

Figure 3-1 Trend curve taken on the motor bearing in the horizontal direction

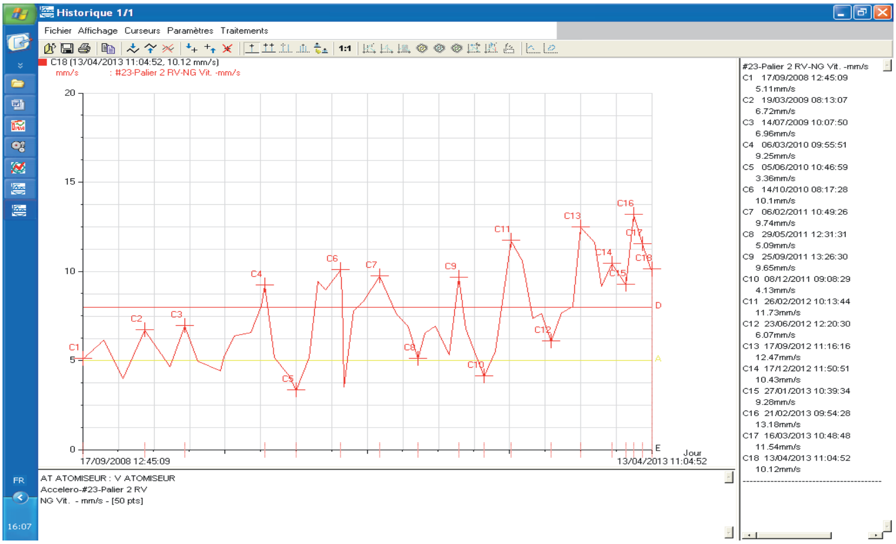

Figure 3-2 Trend curve taken on the motor bearing in the vertical direction

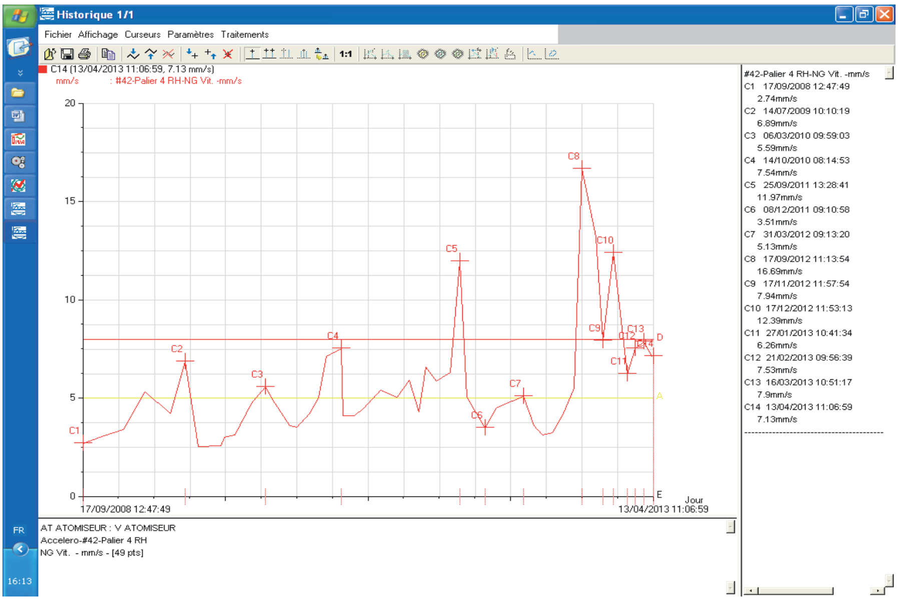

Figure 3-5 Trend curve taken on the bearing No04 in the horizontal direction

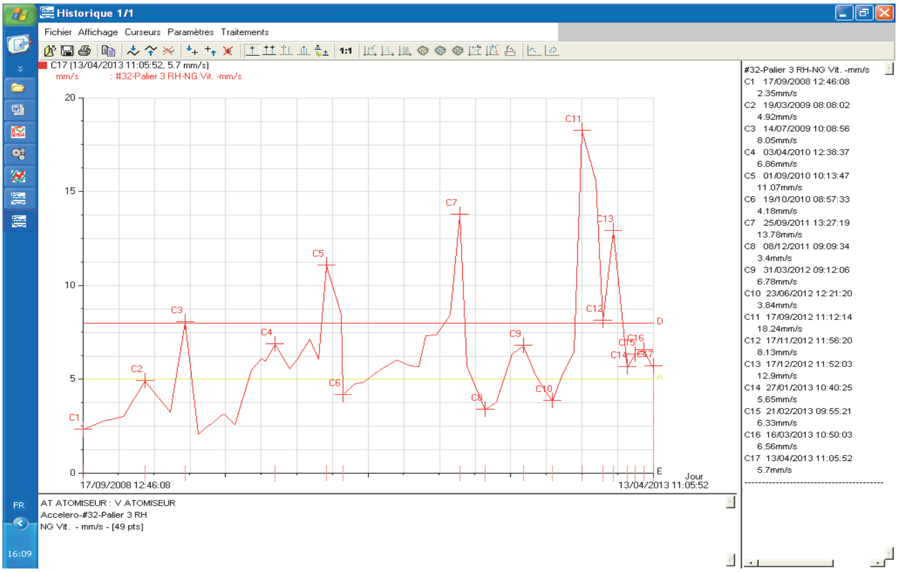

Figure 3-3 Trend curve taken on the bearing No. 03 in the horizontal direction

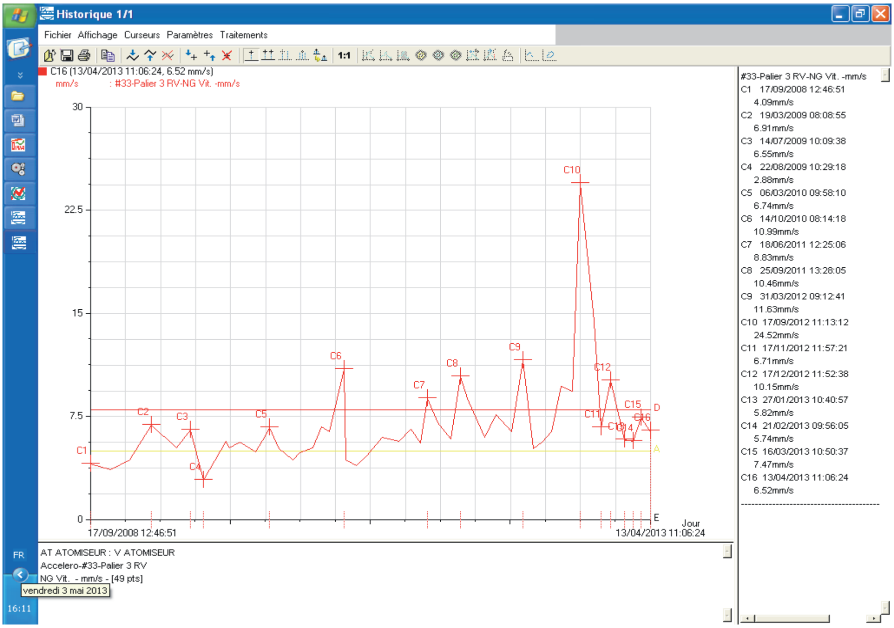

Figure 3-4 Trend curve taken on the bearing No03 in the vertical direction

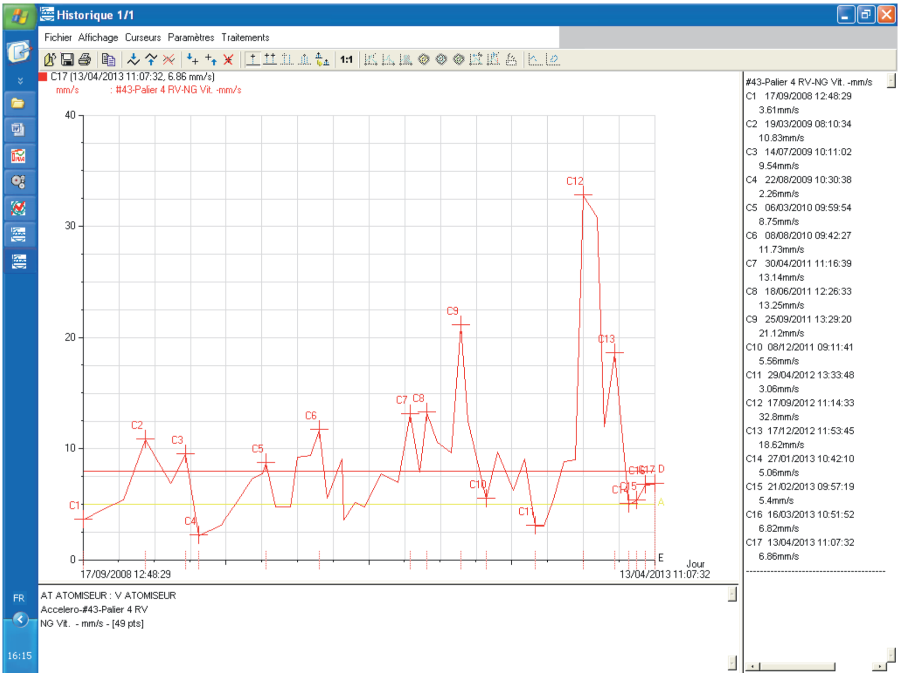

Figure 3-6 Trend curve taken on the bearing No04 in the vertical direction

4- Diagnostic. Analysis of results [3,4,7,8]

The imbalance is a rotary centrifugal force which occurs in the rotational frequency of the rotor (turbine), it causes vibrations in a radial planes, which propagates on the first steps of the machine (bearing No. 03 & 04), and obviously the bearings. This imbalance, in a year, can cause other mechanical defects, failure to wear or play on the bearing surface, bending the shaft carrying the turbine misalignment between levels, and a default turnover in both levels. In our case, this failure (unbalanced) resulted in the appearance of a shock to the transmission line on the turbine started in November 7, 2009.

It was noted that all operations performed on the balancing of the turbine fan were performed in the presence of game bearing fault caused by the imbalance gradually evolving court time to deterioration of the bearings and their change: December 20, 2012 (tab. 3-1).

Just before changing bearings on December 17, 2012, a vibratory diagnosis was established on the fan. Taking measurements on two levels No. 03 & 04 shows the presence of an imbalance in the rotor, which is clearly visible on all spectra taken radially in both horizontal and vertical directions, as shown in Figures 4-5 to Figure 4-8, which have a preponderant component amplitude related to the frequency of rotation of the rotor which is 30 Hz, such that the maximum level is 14.94 mm / s stored on the bearing No. 04 in the vertical radial direction or in the same spectrum we see the appearance of a comb spectral lines whose order 2 and 3 components, as shown in Figure 4-4. They show low amplitude compared to the predominant component related to the frequency of rotation of the rotor, this is due to the presence of the above on both bearing seats game, which explains the difference in the level of vibrations caused by the imbalance when balancing (of 14.94 mm / s11.04 mm / s).

To confirm the presence of the game, we conducted the analysis phase, making two phase measurements on bearing No. 04 in the horizontal and vertical direction (Table 4-1).

Position	Phase	Position	Phase
Horizontal	05,782	Vertical	05,070

Table 4-1

The turbine consists of eleven (11) blades, so each blade is: 32.72 °. The phase difference between the two phase measurements located at 90 °, horizontal and vertical is: 05,782 – 05,070 = 0,712. This gives a phase difference of: 23,296°

For two points located at radial measures 90 ° on the same level, the phase shift between frequency components equal to the rotation frequency (of order 1 of the rotation component) is:
• close to 90 °, in the case of a fault associated with a rotary force as the unbalance.
• Close to 0 ° or 180 ° in the case of a fault related to a directional effort.

In our case, the phase shift is 23.296 °, which is not included in the above stated terms. It allows us to confirm the detection of a default on the rotor unbalance on the turbine connected to the rotary effort in the presence of default game detected by the integral spectral analysis which is linked to the steering effort.

Nevertheless, the failure of the game on the bearing seat in the monobloc persists, and appears as imbalance (unbalance).

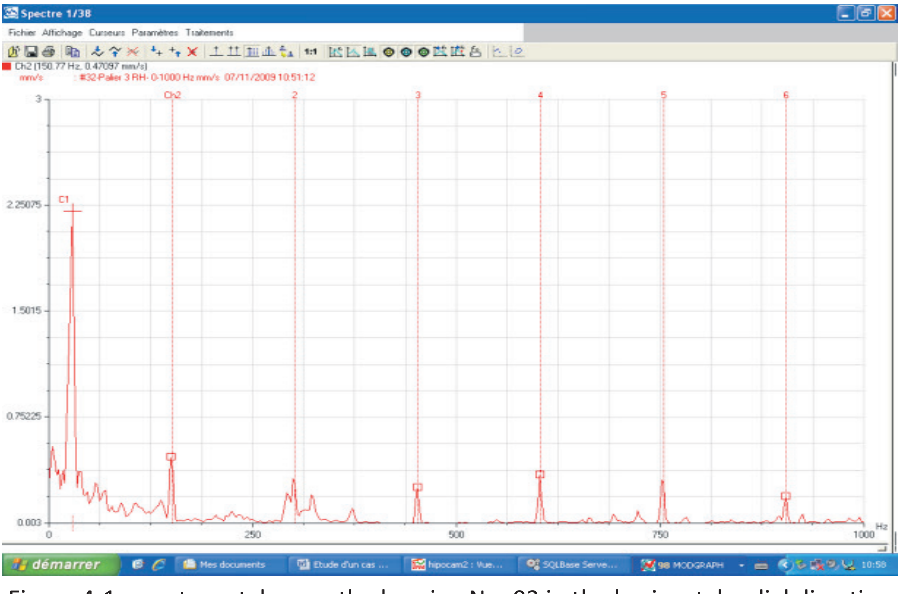

Figure 4-1: spectrum taken on the bearing No. 03 in the horizontal radial direction

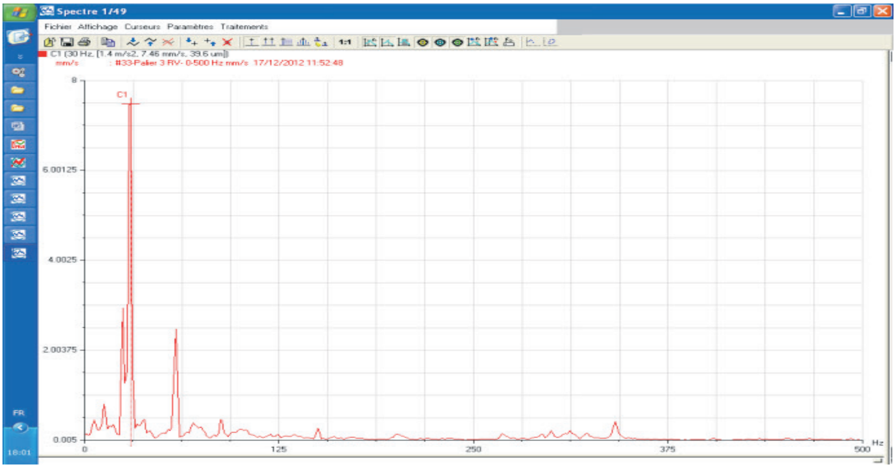

Figure 4-2: spectrum taken 17 12/2012 on the bearing No. 03 in the vertical radial

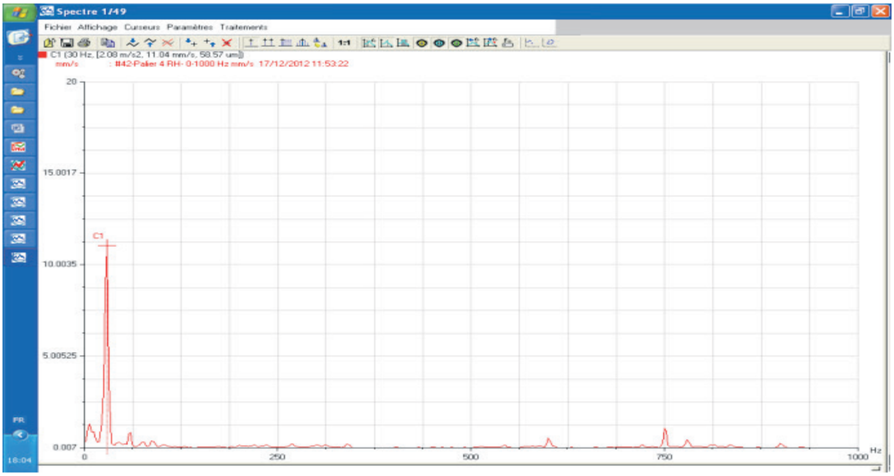

Figure 4-3 spectrum taken 17 12/2012 on the bearing No. 03 in the radial horizontal direction

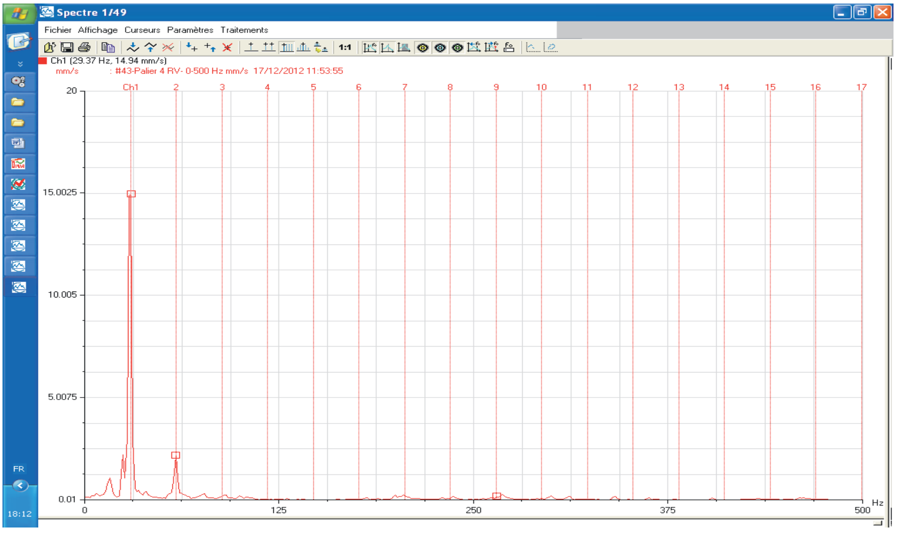

Figure 4-4: spectrum taken 17 12/2012 on the bearing No. 04 in the vertical radial

5- Correction of the imbalance

There is a residual imbalance normal or abnormal resulting in a vibrational spectrum, (turbine pulley, cylinder, ...). By comparing the amplitude of the induced vibration of the thresholds in standards or manufacturer specifications, we can decide on the nature of the imbalance, and whether the need to balance or not.

In our case, the amplitude of vibration associated with the predominant component is 14.94 mm / s (Danger, international standards VDI 2056), which recommends the correction of unbalance on the rotor (balancing). The balancing method is composed of several started, the first is to make the measurements of vibration level with the phase without proof mass, the second mass is carried out with a test speed calculated by the rotation of the rotor is balanced, its radius and weight, and the last launched will be made with correction mass in the calculated position. Sometimes this mass correction with its positioning does not give the value of the desired level of vibration, so we will be forced to improve the correction by a refining operation. The procedure is summarized in Table 03.

LAUNCHED	MASS (gr)	VERTICAL MEASUREMENT	
		LEVELS (mm/s)	PHASE
N°01	-	11.140	05,070
N°02	30 gr Position : 0	21.129	04.279
N°03	Correction : 20.297 gr Position : 06.82	01.940	02.691
Raffinage	02.915 gr Position : 07.06	-	-

Table 5-1 Vertical measurment

The operation of the rotor balancing took place successfully, or the level of vibrations caused by the imbalance to 01.940 mm / s, acceptable by international standards VDI 2056.

These values were found from the analytical [2,3] expressions (theoretical).

6. Validation of the results of the atomiser

According to the method of calculating of MOVILOG 02, the results are measured in RMS.

determined values	vibratory displacement (m)	vibration velocity (mm/s)
theory	$7.784\ 10^{-5}$	14.39
experimentation	$7.928\ 10^{-5}$	14.94

Table 6.1 : Theoretical and experimental results

Conclusion

These types of machines studied require a systematic vibration control. We should avoid their nuisance shutdowns and increase their availability. The programming interventions to repair the appearance of dice defects may arise during their operation.

Condition monitoring by vibration analysis, ensuring the availability of the means of production and guarantees the company's forecasts for a given program. Today a good maintenance of rotating machinery has several advantages, from a reduction of a cost of the product and a business success.

References

[1]. Framatome Diagnostic- Jean de MANS- Le diagnostic vibratoire au service de la Maintenance Réf : 104-1. LYON 1992.

[2]. R.MAGRAOUI, M.OUALI, Contribution à la maintenance conditionnelle par l'analyse vibratoire. Contrôle vibratoire des machines tournantes, 10th Mechanical Congress Oujda Maroc, 19 au 22 avril 2011.

[3]. M.OUALI, R.MAGRAOUI, Contribution à la maintenance conditionnelle par l'analyse vibratoire. Défaillances mécaniques et solutions proposées, 10th Mechanical Congress Oujda Maroc, 19 au 22 avril 2011.

[4]. Philippe Arquès. Professeur des Universités. Ecole centrale de Lyon-DIAGNOSTIC PREDICTIF DE L'ETAT DES MACHINES Edition MASSON 1996.

[5]. Francisque SALLES, Claude LESUEUR, Les Vibrations Mécaniques, MASSON et Cie, Paris, 1972.

[6]. Les défauts des machines. Les défauts des engrenages Encyclopédie pour formation en maintenance préventive 1993.

[7]. L. BOURGAIN, R. DART, J. BOURGAIN, Machines tournantes et circuits Pulsés, Dunod, Edition Bordas, France 1988

[8]. L. BOURGAIN, R. DART & J. BOURGAIN, Machines tournantes et circuits pulsés. Applications Industrielles et médicales de l'analyse spectrale, Dunod, Edition Bordas, France 1988.

DYNAMIC BEHAVIOR OF PIEZOELECTRIC BEAMS ELASTIC AND PIEZOELECTRIC CASES

Bouhedma Sofiane[1], Ouali Mohammed[2] , Mahieddine Ali[3]

[1,2] Structural Mechanics Research Laboratory, Mechanical Engineering Department, Blida University, Algeria,

[3] Laboratory of Energy and Smart Systems, University of Khemis Miliana, Theniet El Had road m44225 Khemis Miliana Ain Defla,Algeria

The corresponding author: Bouhedma Sofiane, bouhedmasofiane1990@gmail.com

Abstract:

Piezoelectric materials are subject to a great deal of research in recent years, whether for mechanical purposes for their potential applications in the fields of mechanical engineering, as a tool of control and regulation, the case of active control and vibration analysis, or for technological purposes in electronics such as crystal oscillators areas. They can also be used as actuators as well as vibration sensors.

The application of the piezoelectric effect in the study of the behavior of beams is the subject of our work. We propose to solve the equations of motion obtained by a variational method, applying the NEWMARK approach and based on a finite element discretization. A MATLAB code is developed to simulate and compare the results of a system formed by a piezoelectric and an elastic beam.

Keywords: Piezoelectricity, piezoelectric beams, modal analysis, Variationnal formulation, NEWMARK approach.

Introduction:

The advantage of the piezoelectric materials lies in their physical properties, mainly their ability to generate controllable deformations by application of an electric field and vice versa, converting a mechanical load (deformation) into an electrical signal. This reciprocity of the piezoelectric phenomenon is what allows their use as sensors or actuators.

Currently, the design and the control of piezoelectric structures is the subject of many theses and research works, we mention:

Shen [1] proposed a finite element model based on the Timoshenko beam theory, modeling the beam and the piezoelectric element separately by using beam elements. Donthireddy Chandrashekhara and [2] develop a finite element model for analysis and control of piezoelectric beams form with integrated actuators stuck to the surface. Dettwiler and Al [3] conducted a finite element analysis of multilayer piezoelectric structures comprising actuators and sensors. Legrain and Petitjean [4] perform an experimental study on the behavior of piezoelectric materials. Sun and Huang [5] presented an analytical model of multilayer composite beams including piezoelectric sensors and actuators.

Ishihara and N. Noda [6] studied a surface crack in a piezo-thermo-elastic body due to thermal loading. Liang Wang, Rui-xiang Bai and Chen Haoran [7] studied the static behavior of a crack situated at the interface between the piezoelectric actuator and the elastic beam.

The aim of the present work is to develop a finite element model for the study of piezoelectric actuator beams. This model is based on the first order Kirchoff's theory.

Mathematical formulation:

Piezoelectricity is an electromechanical interaction, as piezoelectric materials are dielectrics which are deformed under the effect of an electric field and polarized under the effect of deformation.

In our case, we consider a beam with length L, width b, thickness h, the density ρ and right section S.

Using Kirchhoff's first order theory, the displacement field is given by:

$$\begin{cases} \mathbf{U(x,y,z,t) = u(x,t) - z.\theta_y(x,t)} \\ \mathbf{V(x,y,z,t) = 0} \\ \mathbf{W(x,y,z,t) = w(x,t)} \end{cases} \quad \mathbf{(1)}$$

And the deformation field:

$$\begin{cases} \varepsilon_x = \frac{\partial u}{\partial x} - z.\frac{\partial \theta}{\partial x} \\ \varepsilon_{xz} = \frac{\partial W}{\partial x} - \theta \end{cases} \quad (2)$$

With: u, v and w are the displacements in the X, Y and Z directions.

The constitutive equations of piezoelectricity, if we neglect the thermal effect can be expressed in the following form:

$$\boldsymbol{\sigma} = \bar{\mathbf{C}}\boldsymbol{\varepsilon} - \bar{\mathbf{e}}^{t}\mathbf{E}$$

$$\mathbf{D} = \bar{\mathbf{e}}\boldsymbol{\varepsilon} + \bar{\boldsymbol{\epsilon}}\mathbf{E} \quad (3)$$

σ, ε, $\overline{C}$, $\overline{e}$, D, $\overline{\epsilon}$, E are respectively the stress (6 × 1), the deformations (6 × 1), the stiffness matrix(6 × 6), the piezoelectric constant matrix (3 × 6), the electric displacement (3 × 1), the permittivity matrix (3 × 3) and the electric field (3 × 1).

By assuming that:

- The stresses: σy, σyz, σxz are negligible compared with σx.
- The upper surface of the beam is free to move in the Z direction, which results in σz=0.
- The electric fields E1 and E2 are negligible in front of E3.

Equations (3) become:

$$\begin{Bmatrix} \sigma_x \\ \sigma_{xz} \end{Bmatrix} = \begin{bmatrix} \widetilde{C}_{11} & 0 \\ 0 & \widetilde{C}_{55} \end{bmatrix} \begin{Bmatrix} \varepsilon_x \\ \varepsilon_{xz} \end{Bmatrix} - \quad - \begin{Bmatrix} e_{31} \\ 0 \end{Bmatrix} E_Z \quad (4)$$

$$\mathbf{D_z} = \tilde{e}_{31}\varepsilon_x + \tilde{\epsilon}_{33}E_Z$$

With :

$$\widetilde{C}_{11} = C_{11} + C_{16}\left(\frac{C_{12}C_{26} - C_{16}C_{22}}{C_{22}C_{66} - C_{26}^2}\right) - C_{12}\left(\frac{C_{12}C_{66} - C_{16}C_{26}}{C_{22}C_{66} - C_{26}^2}\right)$$

$$\widetilde{C}_{55} = C_{55} - \frac{C_{45}^2}{C_{44}} \quad (5)$$

$$\tilde{e}_{31} = e_{31}\left(1 - \frac{C_{16}C_{26} - C_{12}C_{66}}{C_{26}^2 - C_{22}C_{66}}\right)$$

$$\tilde{\epsilon}_{33} = \epsilon_{33} + \frac{C_{66}e_{31}^2}{C_{22}C_{66} - C_{26}^2}$$

The expression of the kinetic energy is:

$$E_c = \frac{1}{2}\rho\int\left[\left(\frac{\partial u}{\partial t} - z\frac{\partial \theta}{\partial t}\right)^2 + \quad + \left(\frac{\partial w}{\partial t}\right)^2\right] d\Omega \tag{6}$$

The potential energy is given by:

$$E_p = \frac{1}{2}\int_{\Omega}(\sigma\varepsilon - ED)\, d\Omega \tag{7}$$

$$E_p = \frac{1}{2}\int_{\Omega}(\tilde{C}_{11}\varepsilon_x\varepsilon_x + \tilde{C}_{55}\varepsilon_{xz}\varepsilon_{xz} - \quad -\tilde{e}_{31}\varepsilon_x E_Z - \tilde{e}_{31}E_Z\varepsilon_x - \quad -\tilde{\epsilon}_{33}E_Z E_Z).\, d\Omega \tag{8}$$

The vector of external forces:

$$W_{ext} = \int_A\left(wp_z + \theta_y m_y + \quad + \phi.D\right).\, dA \tag{9}$$

Where D is the load applied on the surface, p_z is a distributed load and m_y is a pair of linear intensity.

Finite element formulation:

For our study, the interpolation functions are chosen as follows:

$$N_1 = 1 - \frac{x}{L_e}, \quad N_2 = 2\frac{x^3}{L_e^3} - 3\frac{x^2}{L_e^2} + 1 N_3 = \frac{x^3}{L_e^2} - \frac{x^2}{L_e} + x, \quad N_4 = \frac{x}{L_e} N_5 = 3\frac{x^2}{L_e^2} - 2\frac{x^3}{L_e^3}, \quad N_6 = \frac{x^3}{L_e^2} - \frac{x^2}{L_e},$$

$$N_7 = 6\frac{x^2}{L_e^3} - 6\frac{x}{L_e^2}, \quad N_8 = 3\frac{x^2}{L_e^2} - 4\frac{x}{L_e} + 1, \quad N_9 = -6\frac{x^2}{L_e^3} + 6\frac{x}{L_e}, \quad N_{10} = 3\frac{x^2}{L_e^2} - 2\frac{x}{L_e}$$

L_e : elementary length.

These functions form the interpolation matrix N such that: $N =$

$$\begin{bmatrix} N_1 & 0 & 0 & N_2 & 0 & 0 \\ 0 & N_3 & N_4 & 0 & N_5 & N_6 \\ 0 & N_7 & N_8 & 0 & N_9 & N_{10} \end{bmatrix}$$

$N_\Phi = \left[1 - \frac{z}{h} \quad \frac{z}{h}\right]$ is the interpolation matrix for the electric field.

So: $\begin{Bmatrix} u \\ \theta \\ w \end{Bmatrix} = Nq_e$ and $\Phi = N_\Phi \Phi_e$

Where: $q_e \begin{Bmatrix} u_i \\ \theta_i \\ w_i \\ u_j \\ \theta_j \\ w_j \end{Bmatrix}$ and Φ_e are respectively the nodal displacements and the nodal electric potential.

By replacing the displacements by their expressions we obtain:

$$\boldsymbol{E_c = \frac{1}{2}\dot{q}_e^T[M_e]\dot{q}_e} \tag{10}$$

With :

$$[M_e] = \rho \int_\Omega ([N_u]^T[N_u] + \quad +z^2[N_\theta]^T[N_\theta] + [N_w]^T[N_w] - \quad -2z[N_u]^T[N_\theta])\, d\Omega$$

$$\boldsymbol{E_{p\,\text{élastic}} = \frac{1}{2} q_e^t [K_{uu}]_e q_e} \tag{11}$$

With :

$$[K_{uu}]_e = \int_\Omega \begin{bmatrix} \tilde{C}_{11}\begin{pmatrix} \left[\frac{dN_u}{dx}\right]^T \left[\frac{dN_u}{dx}\right] + z^2 \left[\frac{dN_\theta}{dx}\right]^T \left[\frac{dN_\theta}{dx}\right] \\ -2z\left[\frac{dN_u}{dx}\right]^T \left[\frac{dN_\theta}{dx}\right] \end{pmatrix} \\ +\tilde{C}_{55}\left(\left(\left[\frac{dN_w}{dx}\right] - N_\theta\right)^T \left(\left[\frac{dN_w}{dx}\right] - N_\theta\right)\right) \end{bmatrix} d\Omega$$

$$\boldsymbol{E_{p\,piezo} = \frac{1}{2} q_e^T [K_{u\Phi}]\Phi + \quad + \frac{1}{2}\Phi_e [K_{\Phi u}] q_e^T} \tag{12}$$

With: $[K_{u\Phi}] = -\int_\Omega \tilde{e}_{31}\left(\left[\frac{dN_u}{dx}\right]^T [N_\Phi] + \quad +z\left[\frac{dN_\theta}{dx}\right]^T [N_\Phi]\right)\, d\Omega$

$[K_{\Phi u}] = -\int_\Omega \tilde{e}_{31}\left([N_\Phi]^T \left[\frac{dN_u}{dx}\right] + \quad +[N_\Phi]^T \left[\frac{dN_\theta}{dx}\right]\right)\, d\Omega$

$$\boldsymbol{E_{p\,dielect} = \frac{1}{2}\Phi_e^T [K_{\Phi\Phi}]_e \Phi_e} \tag{13}$$

With : $[K_{\Phi\Phi}]_e = -\int_\Omega \tilde{\epsilon}_{31}([N_\Phi]^T[N_\Phi])\, d\Omega$

$$\boldsymbol{\{F\}_e = \int_A \left([N_w]^T p_z + [N_\theta]^T m_y\right) dA} \tag{14}$$

$$\boldsymbol{\{Q\}_e = \int_A \Phi_e^T ([N_\Phi]^T D) dA} \tag{15}$$

Where: $$\boldsymbol{\{f\}_e = \begin{Bmatrix} \{F\}_e \\ \{Q\}_e \end{Bmatrix}} \tag{16}$$

Once the elementary vectors and matrices are defined, we proceed to the assembly step, to express them in global coordinates, to form the global matrices and global vectors representing the entire structure.

$$\begin{bmatrix} [M] & 0 \\ 0 & 0 \end{bmatrix} \begin{Bmatrix} \{\ddot{u}\} \\ \{\ddot{\Phi}\} \end{Bmatrix} + + \begin{bmatrix} [K_{uu}] & [K_{u\Phi}] \\ [K_{\Phi u}] & [K_{\Phi\Phi}] \end{bmatrix} \begin{Bmatrix} \{u\} \\ \{\Phi\} \end{Bmatrix} = \begin{Bmatrix} F \\ Q \end{Bmatrix} \quad (17)$$

To solve these equations, we opt for the Newmark approach, given its simplicity, accuracy and stability. Approximations for the Newmark method are provided by:

$$\dot{u}_{n+1} \cong \dot{u}_n + (1-\gamma)\Delta t\, \ddot{u}_n + \quad +\gamma\, \Delta t\, \ddot{u}_{n+1} \quad (18)$$

$$u_{n+1} \cong u_n + \Delta t.\dot{u}_n + \quad + \left(\frac{1}{2} - \beta\right) \Delta t^2 \ddot{u}_n + +\beta \Delta t^2 \ddot{u}_{n+1}$$

Introducing the numerical scheme (18) in the equations of motion (17) we obtain:

$$\widetilde{M}\ddot{u}_{n+1} = F_{n+1} - C(\dot{u}_n + +(1-\gamma).\Delta t.\ddot{u}_n) - K\left(u_n + +\Delta t.\dot{u}_n + \left(\frac{1}{2} - \beta\right)\Delta t^2\, \ddot{u}_n\right) \quad (19)$$

With :

$\widetilde{M} = M + \gamma.\Delta t.C + \beta \Delta t^2 K$;

$\gamma = \frac{1}{2}$ et $\beta = \frac{1}{6}$

Results :

For the validation of our model

for the study of beams, a MATLAB code is developed. This code takes into account both elastic and piezoelectric case. In order to

perform numerical simulations of an elastic beam bending, we consider a console beam-ie clamped-free with a length L = 0.5m, width b= 0.03m and thickness h = 0.01m. This beam is subjected to the action of a uniformly distributed load over its entire length. The selected material (mild steel) has the following mechanical properties:

Young's modulus: **E = 2.10^{11} N/m^2,** Poisson coefficient: **ν = 0.3** and density : **ρ = 8000 Kg/m^3.**

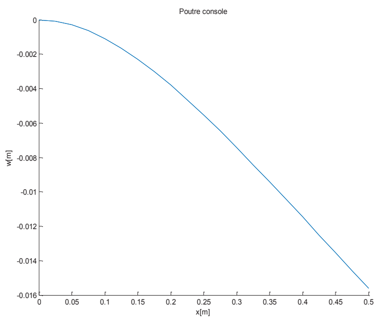

Figure 1: The deflection of the elastic beam

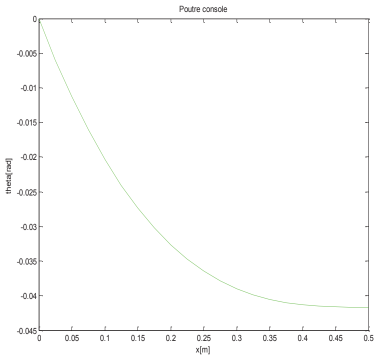

Figure 2: Rotation of the elastic beam.

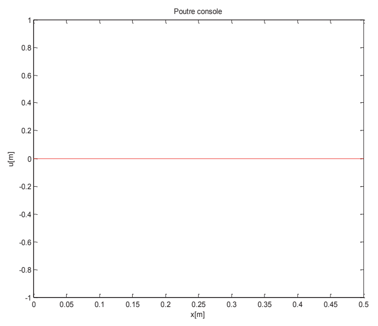

Figure 3: The axial displacement of the elastic beam.

To validate the finite element
model, we proceed to a comparison between analytical eigenvalues and those obtained by finite elements for the first 20 modes.

Modes	Frequencies (exact)	Frequencies (FE)	Relative error(%)
1	202.974704	202.979418	0.002322
2	1272.112568	1271.384009	0.057272
3	3562.310339	3556.908165	0.151648
4	6980.317978	6961.565494	0.268648
5	11538.892984	11489.741877	0.425960
6	17237.111742	17130.495851	0.618525
7	24074.974252	23871.677245	0.844433
8	32052.480512	31699.167162	1.102296
9	41169.630525	40597.153041	1.390533
10	51426.424289	50548.361883	1.707415
11	62822.861804	61534.309574	2.051088
12	75358.943071	73535.556627	2.419602
13	89034.668090	86531.964641	2.810931
14	103850.036860	100502.948007	3.223002
15	119805.049382	115427.715894	3.653714
16	136899.705655	131285.500183	4.100962
17	155134.005680	148055.765653	4.562662
18	174507.949457	165718.399369	5.036762
19	195021.536984	184253.876833	5.521267
20	216674.768264	203643.403014	6.014251

Table 1: Comparison between the analytical and numerical eigenvalues.

This comparison shows that the finite element model is well-chosen as the relative error does not exceed 6% for the 20th mode, and the results are almost identical.

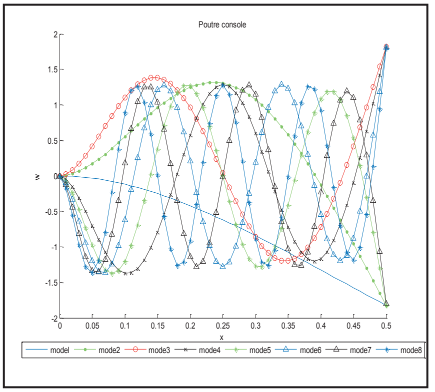

Figure 4: Overlapping 8 eigenmodes of vibration of the elastic beam.

To talk over the dynamic problem, we consider the same beam (forced undamped vibration mode) subjected to the action of a harmonic force F = F.cos (100.t).

The resolution of this problem by the Newmark approach gives the graph (Figure 5), which represents the vertical vibrations of the beam.

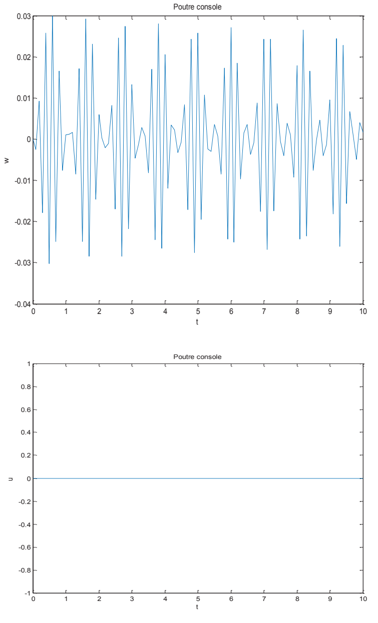

Figures 5 and 6: The vertical and axial vibration and of the elastic beam.

To investigate the piezoelectric case, we consider a beam having the same dimensions as those of the elastic case. This beam is subjected this time to the action of a mechanical load uniformly distributed over the entire length and a difference in electric potential V in the thickness direction. The material of the beam is piezoelectric, it is a piezoelectric ceramic, PZT-4, which has the following mechanical and electrical properties:

Density ρ=7500 Kg/m^3

The stiffness matrix is:

$$C = \begin{bmatrix} 13.90 & 7.78 & 7.43 & 0 & 0 & 0 \\ 7.78 & 13.90 & 7.43 & 0 & 0 & 0 \\ 7.43 & 7.43 & 11.5 & 0 & 0 & 0 \\ 0 & 0 & 0 & 2.56 & 0 & 0 \\ 0 & 0 & 0 & 0 & 2.56 & 0 \\ 0 & 0 & 0 & 0 & 0 & 3.07 \end{bmatrix} .10^{10} \qquad [N/m^2]$$

The matrix of piezoelectric constants is:

$$e = \begin{bmatrix} 0 & 0 & 0 & 0 & 12.7 & 0 \\ 0 & 0 & 0 & 12.7 & 0 & 0 \\ -5.2 & -5.2 & 15.1 & 0 & 0 & 0 \end{bmatrix} \qquad [C/m^2]$$

The matrix of dielectric constants is:

$$\epsilon=\begin{bmatrix} 13.06 & 0 & 0 \\ 0 & 13.06 & 0 \\ 0 & 0 & 11.51 \end{bmatrix} [nF/m]$$

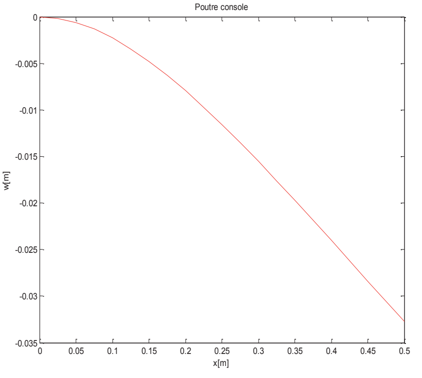

Figure 7: The deflection w of the console beam in actuator mode.

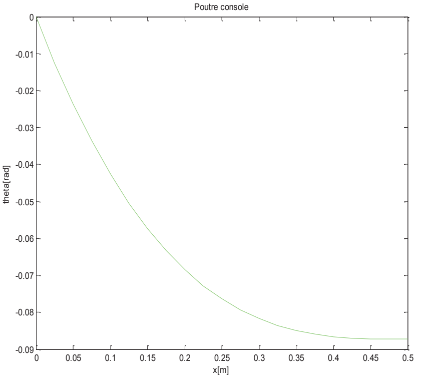

Figure 8: The rotation θ of a console beam in actuator mode.

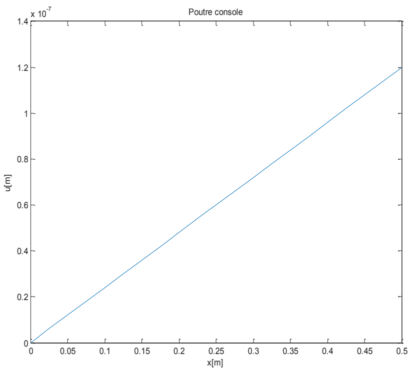

Figure 9: The axial displacement u of a console beam in actuator mode.

The first important finding, we can notice by comparing the results of the elastic and piezoelectric case is that in the later case, the axial displacement u is non-zero, but in linear variation, which results of the application of an electric potential difference between the upper and lower surfaces of the beam.

Turning now to the results of the dynamic problem (ie the forced vibration) without taking into account the structural damping of the beam. The external excitation is harmonic F = F.cos (100.t).

The graph (Figure 10) and (Figure 11) give the vertical and the axial vibrations of the piezoelectric beam.

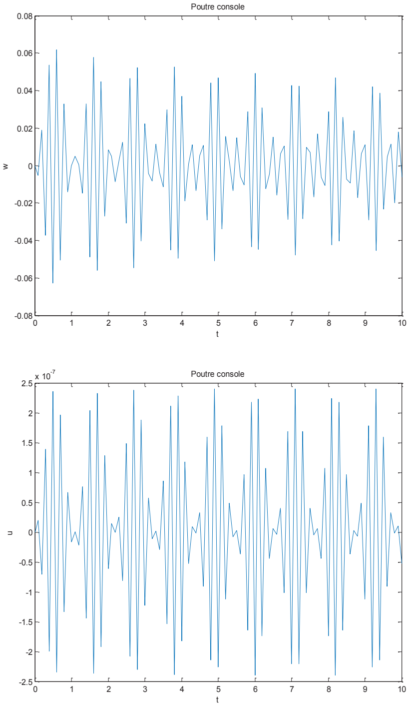

Figure 10.11: The vertical w and the axial u vibrations of the piezoelectric beam.

In order to show the importance of choosing the piezoelectric material on the behavior of the beam, we propose to study the same beam considered in actuator mode, but for different materials: PZT2, PZT-4, PZT-5A, PZT-5H, PZT-7A, PZT8, ZnO and ZnS.

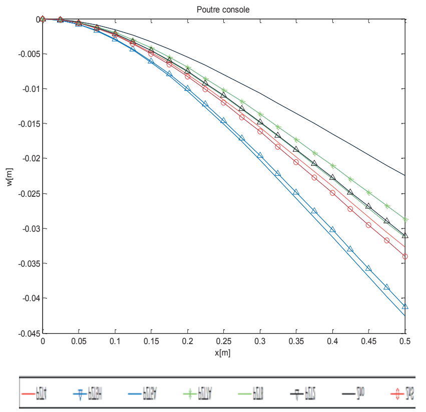

Figure 12: Comparison of the beam deflection in actuator mode for different materials.

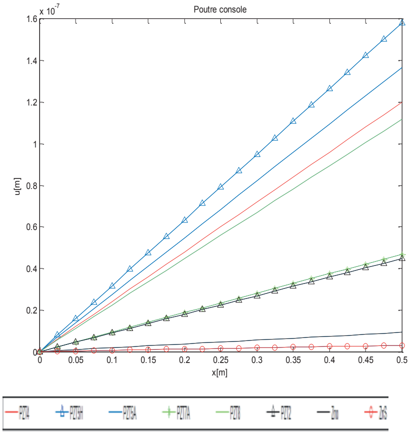

Figure 13: Comparison of the axial displacements of the beam in actuator for different materials.

The graphs (12) and (13) show that the shape of the deflection w and the slope of the axial displacements u differ from piezoelectric material to another, mainly because the mechanical and electrical characteristics are different. Hence we can conclude that each piezoelectric material is intended for a certain class of applications. For example, if the application requires a large deflection and axial movement

PZT-5A and PZT-5H are used instead of using a PZT-2, and so on...

In this section we try to see the influence of the beam's thickness on the static and dynamic behavior of the piezoelectric beam, that's why we consider the same beam, but for different thicknesses.

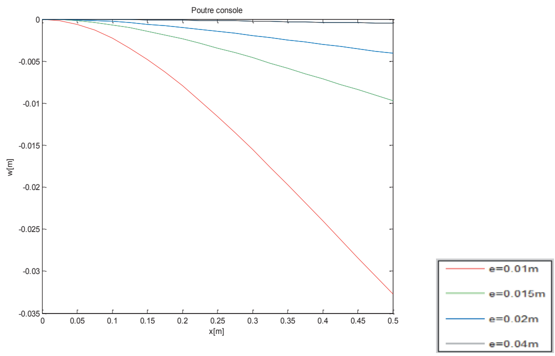

Figure 14: Influence of the thickness on the deflection of the piezoelectric beam.

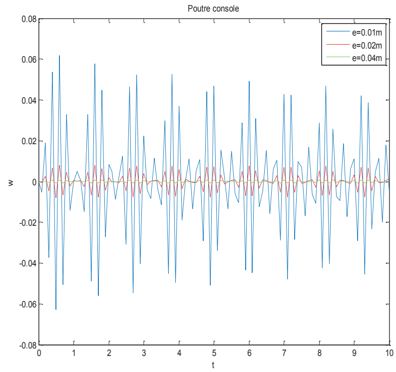

Figure 15: Influence of the thickness on the vertical vibrations of the beam.

It is clear that the choice of the dimensions of the beam is also important because of their impact on the static and dynamic behavior of the beam. For example, if we consider the influence of the thickness, we can simply find that increasing the thickness leads to reduce the deflection in the static case and to reduce the amplitude of the vertical vibrations of the beam in the dynamic case.

Conclusion:

Throughout this work, we study the impact of the application of piezoelectric effect on the behavior of beams and modeling of these beams on the one hand. And on the other hand, we have numerically simulated the behavior of these beams in both elastic and piezoelectric case. A finite element formulation is presented for piezoelectric beams in actuator mode.

References:

[1] **:** M.H.H. Shen, 1995, A new mosdeling technique for piezoelectrically actuated beams, Computers and Structures 57 (3).

[2] **:** P. Donthireddy, K. Chandrashekhara, 1996, Modeling and shape control of composite beams with embedded piezoelectric actuators, Composite structures 35.

[3] **:** D. T. Detwiler, M. H. H. Shen, V. B. Venkayya, 1995, Finite element analysis of laminated composite structures containing distributed piezoelectric actuators and sensors, Finite Elements in Analysis and Design 20.

[4] **:** I. Legrain, B.Petitjean, 1997, Evaluation de céramiques électrostrictives en vue d'une utilisation en tant qu'actionneurs dans le domaine du contrôle actif des vibrations, Rapport ONERA N°9776.

[5] **:** B. Sun, D. Huang, 2001, Vibration suppression of laminated composite beams with a piezoelectric damping layer, Composite Structures 53 437.447.

[6] **:** Masayuki Ishihara, Naotake Noda, May–June 2005 , Control of thermal stress intensity factor in a piezo-thermo-elastic semi-infinite body with an edge crack, European Journal of Mechanics A/Solids, Volume 24, Issue 3, Pages 417-426.

[7] **:** Liang Wang, Rui-xiang Bai , Haoran Chen, January 2013 , Analytical modeling of the interface crack between a piezoelectric actuator and an elastic substrate considering shear effects, International Journal of Mechanical Sciences, Volume 66, Pages 141-148**.**

Induction Machine Modeling Using Finite Element Method under Stator Short-circuit Fault

{ A. BOUZIDA, O. TOUHAMI and R.ABDELLI }
BOUZIDA.UMBB@GMAIL.COM

Introduction

The electrical induction motors are used in 90 % more of the industry applications, and is vital to guarantee their correct functioning. So, it is necessary to have a tool that allows knowing the motor's condition without intervening in the equipment's operation. The stator fails form the 37 % of the electrical motor failures, being the inter-turns short circuit the most common, which reduces the ability of produce a balanced electrical field, causing vibration increase on the machine, and consequently, isolation degradation and motor bearings failure.

Modelling with FEM

To make the study, the software FLUX2D was used; it has a magnetic transitory formulation included, which solves the problem in discrete time points. Various types of problems can beings solved with this software. The study into magneto-transient is appropriate particularly well for our need. The coupling of our magnetic diagram to an electrical circuit and the presence of a tread in the air-gap make it possible to follow the dynamic behaviour of the machine. The software solves the following equation:

$$\sigma_e \frac{d\vec{A}}{dt} + \vec{rot}\left(\frac{1}{\mu rot(\vec{A})}\right) = J + \vec{rot}(\vec{H})$$

- A : Magnetic potential (Weber/m)
- J : Density of current (A/m)
- μ : Magnetic permeability (H/m)
- H : Magnetic field (A/m)
- σ: Electric conductivity (1/Ω.m)
- t : Time(s)

Geometry and Mesh

The numerical simulations in this paper refer to a 2-pole induction motor, 3-phase star connected, Pn = 7.5 kW, Unf = 380 V, frequency, f1n = 50 Hz.

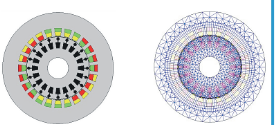

Figure 5: IM geometry and meshing

The machine was simulated for 5 cases: Healthy Machine and machines with inter-turn faults (5 turns, 10 turns, 25 turns and 50 turns are shorted)

Results of Simulation

By calculating the electromagnetic field with FEM analysis, the machine inductances and back EMFs can be obtained. The parameters obtained from the FEM analysis contain the information of the fault location and severity. The different simulation cases are shown.

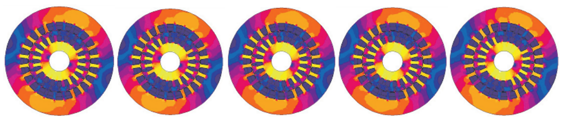

Healthy 5 Spires 10 Spires 25 Spires 50 Spires

The numerical results corresponding to a magnetic flux analysis of the 2D electromagnetic field-circuit problem associated to the induction motor, figures, number of short-circuited turn determines a decrease of the distribution of the field density. Another effect of this type of fault, consists in an important increase with the number turns short-circuited.

Flux Analysis

The gap flows are represented in the following figures, the flux density is depends on the degree of fault. The flux density clearly shows the effect of the defects,

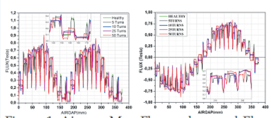

Figure 1: Air-gap Mag-Flux and normal-Flux distribution

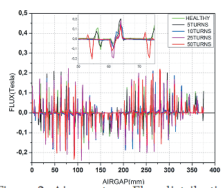

Figure 2: Air-gap tang-Flux distribution

Forces, Torque Analysis

The figures shows the force, torque and the FFT the force in the air-gap for the 5 cases.

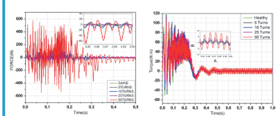

Figure 3: Air-gap X Force and Torque

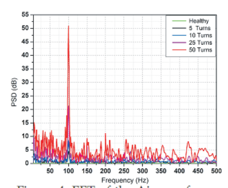

Figure 4: FFT of the Air-gap force

Conclusion

FE analysis is used for describe the Induction Machine with turn fault. The different performances can be determined when the simulation is done. The proposed model is used for studying the machine behaviour under fault condition. The FEM model of the Induction machine has enables to calculate several parameters, the comparison between the various parameters obtained in the case healthy and defective, we note that this method of analysis clearly shows the effect of the defect on the behavior of the machine and one can see the difference in the various signatures like flow, the couple and the force according to the degree of defect.

Bibliography

[1] D. Diaz, M. C. Amaya, A. Paz. : "Inter-turn Short-circuit Analysis in an Induction Machine by Finite Elements Method and Field Tests" *XXth International Conference on Electrical Machines (ICEM), IEEE 2012, Page(s):1757 - 1763.*

[2] J. Seshadrinath, B. Singh, K. Panigrahi. : "Single-Turn Fault Detection in Induction Machine Using Complex-Wavelet-Based Method". In *IEEE TRANSACTIONS ON INDUSTRY APPLICATIONS, VOL. 48, 2012, Page(s):1846-1854.*

[3] M. Arkan, D. Kostic-Perovi, K. P.J. Unsworth. : "Modelling and simulation of induction motors with inter-turn faults for diagnostics-Based Method". In *Electric Power Systems Research, VOL. 75, 2005, Page(s):57-66.*

[4] Ebrahimi, B.M. , Akin, B. , Toliyat, H.A. : "Finite-Element Transient Analysis of Induction Motors Under Mixed Eccentricity Fault ". In *IEEE Transactions on Magnetics, VOL. 44, 2008 , Page(s):66-74.*

ROTOR FLUX ESTIMATION BASED ON ACCURATE ADAPTIVE ALGORITHM FOR FIELD ORIENTED CONTROL INDUCTION MACHINE DRIVES

A. Aibeche, M. Kidouche, H. Akroum and S. Grouni

Laboratory of Applied Automation (LAA), FHC

Faculty of Hydrocarbons and Chemistry

University of M'Hamed Bougara of Boumerdes (UMBB), Boumerdes, Algeria

nababde2001@yahoo.fr, m_kidouche@hotmail.com,

akroum@yahoo.fr, sgrouni@yahoo.fr

Abstract- This paper proposes new architectures for designing accurate adaptive algorithm (AAA) and robust control for quasi exact flux position and magnitude estimation of induction machines over a large speed rang application in direct field oriented control (DFOC). Model of induction machine presents the basic idea based on observer structure, which is composed of voltage model (VM) and current model (CM). But these methods are effects in low speed range and sensitive's of machine parameters. Both observer structures are dominated by a current model at low speeds, and a voltage model at high speeds.

In this paper generalized analysis method based in accurate adaptive algorithm (AAA) is proposed to eliminated and analyze the kinds of the linear flux observers in unified form. The principal objective of this method is to eliminate and reduce the disadvantages of these estimators. The accurate adaptive algorithm (AAA) method is based on the exploitation and the combination between the two preceding models ones while being based on measurements of stator voltages and currents and on the estimate of rotor speed. The performance of the solution proposed has been tested by simulation and by experiments.

Keywords- Induction machine drives, Field oriented control, Stator and rotor flux control.

Laboratory of **A**pplied **A**utomation **(LAA)**
Faculty of Hydrocarbons and Chemistry **(FHC)**
University of **M**'Hamed **B**ougara of **B**oumerdes **UMBB**-Algeria

Rotor flux estimation based on accurate adaptive algorithm for field oriented control induction machine drives

A. Aibeche, M. Kidouche, H. Akroum and S. Grouni

Objective

The speed sensor feedback is replaced by the speed estimate based on the observer and estimate of flux rotor.

The estimate flux rotor is based on the measurements of voltages and currents on motor drives.

Model of induction machine presents the basic idea based on observer structure, which is composed of voltage model (VM) and current model (CM).

Method proposed in this poster is generalized analysis method based in accurate adaptive algorithm (AAA).

The principal objective of this method is to eliminate and reduce the disadvantages of these estimators.

The main reasons of inaccuracy, especially at low speeds, are increased sensitivity against mismatch between models and drive parameters.

The accurate adaptive algorithm (AAA) method is based on the exploitation and the combination between the two preceding models ones while being based on measurements of stator voltages and currents and on the estimate of rotor speed.

Induction Motor Model

The d-q dynamic model of the induction machine with the reference frame fixed to the stator is given by:

$$\begin{cases} v_{dqs}^{s} = R_s i_{dqs}^{s} + \dfrac{d\lambda_{dqs}^{s}}{dt} \\ 0 = R_r i_{dqr}^{s} - j\omega_r \lambda_{dqr}^{s} + \dfrac{d\lambda_{dqr}^{s}}{dt} \end{cases} \quad \text{and} \quad \begin{cases} \lambda_{dqs}^{s} = L_s i_{dqs}^{s} + L_m i_{dqr}^{s} \\ \lambda_{dqr}^{s} = L_r i_{dqr}^{s} + L_m i_{dqs}^{s} \end{cases}$$

Where:

$\lambda_{dr}^{s}, \lambda_{qr}^{s}$ are d-axis and q-axis rotor flux linkages in stator reference frame,

$\lambda_{ds}^{s}, \lambda_{qs}^{s}$ are d-axis and q-axis stator flux linkages in stator reference frame,

ω_r is rotor speed.

Open loop-flux observers & estimators

There are two basics topologies for open-loop flux observers as dictated by the measured states/inputs and corresponding flux model. These two have been referred to as the current model and the voltage model [1].

For field orientation it is necessary to know magnitude $|\lambda_r|$ and angle θ_{λ} of rotor flux. Since λ_r is not measured we use open loop observer to estimate it.

Current Model open-Loop Estimators

The current model of the induction motor can be written as:

$$\begin{cases} \dfrac{d\hat{\lambda}_{dr}^{s,c}}{dt} = \dfrac{\hat{L}_m}{\hat{\tau}_r} i_{ds}^{s} - \dfrac{1}{\hat{\tau}_r}\hat{\lambda}_{dr}^{s,c} + (\omega_s - \omega_r)\hat{\lambda}_{qr}^{s,c} \\ \dfrac{d\hat{\lambda}_{qr}^{s,c}}{dt} = \dfrac{\hat{L}_m}{\hat{\tau}_r} i_{qs}^{s} - \dfrac{1}{\hat{\tau}_r}\hat{\lambda}_{qr}^{s,c} - (\omega_s - \omega_r)\hat{\lambda}_{dr}^{s,c} \end{cases} \Rightarrow \begin{cases} \dfrac{d\hat{\lambda}_{dr}^{s,c}}{dt} = \dfrac{\hat{L}_m}{\hat{\tau}_r} i_{ds}^{s} - \dfrac{1}{\hat{\tau}_r}\hat{\lambda}_{dr}^{s,c} - \omega_r \hat{\lambda}_{qr}^{s,c} \\ \dfrac{d\hat{\lambda}_{qr}^{s,c}}{dt} = \dfrac{\hat{L}_m}{\hat{\tau}_r} i_{qs}^{s} - \dfrac{1}{\hat{\tau}_r}\hat{\lambda}_{qr}^{s,c} - \omega_r \hat{\lambda}_{dr}^{s,c} \end{cases}$$

The rotor flux angle and magnitude estimated by the current model

$$\hat{\theta}_{\lambda}^{c,m} = \tan^{-1}\left(\frac{\hat{\lambda}_{qr}^{s,c}}{\hat{\lambda}_{dr}^{s,c}}\right), \left|\hat{\lambda}_r^{c,m}\right| = \sqrt{(\hat{\lambda}_{dr}^{s,c})^2 + (\hat{\lambda}_{qr}^{s,c})^2}$$

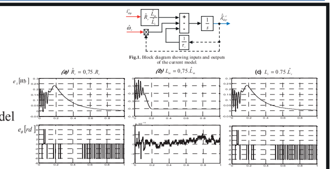

Fig.1. Block diagram showing inputs and outputs of the current model

(a) $\hat{R}_r = 0.75\,R_r$ (b) $\hat{L}_m = 0.75\,\hat{L}_m$ (c) $\hat{L}_r = 0.75\,\hat{L}_r$

The resulting estimator requires measured rotor speed as well as measured stator current as input, as indicated in the simplified block diagram in Fig.1. The estimator, referred to as the current model has good properties at low frequencies but is sensitive to parameter errors at high frequencies (Jansen et al, 1994a).

Where $(\hat{R}_r, \hat{L}_r, \hat{L}_m)$ are estimated parameters of dynamic model? The variation effects are calculated by the signals errors as follows: $e_{\lambda} = |\lambda_r| - \left|\hat{\lambda}_r^{c,m}\right|, e_{\theta} = \theta_{\lambda} - \hat{\theta}_{\lambda}^{c,m}$

voltage Model open-Loop Estimators

The voltage model of the induction motor can be written as:

$$\begin{cases} \hat{\lambda}_{dr}^{s,v} = \left(\dfrac{\hat{L}_s\hat{L}_r - \hat{L}_m^2}{\hat{L}_m}\right) i_{ds}^{s} + \dfrac{\hat{L}_r}{\hat{L}_m}\hat{\lambda}_{ds}^{s,v} \\ \hat{\lambda}_{qr}^{s,v} = \left(\dfrac{\hat{L}_s\hat{L}_r - \hat{L}_m^2}{\hat{L}_m}\right) i_{qs}^{s} + \dfrac{\hat{L}_r}{\hat{L}_m}\hat{\lambda}_{qs}^{s,v} \end{cases} \quad and \quad \begin{cases} \hat{\lambda}_{ds}^{s,v} = \int\left(v_{ds}^{s} - \hat{R}_s i_{ds}^{s}\right)dt \\ \hat{\lambda}_{qs}^{s,v} = \int\left(v_{qs}^{s} - \hat{R}_s i_{qs}^{s}\right)dt \end{cases}$$

The rotor flux angle and magnitude estimated by the current model

$$\hat{\theta}_{\lambda}^{v,m} = \tan^{-1}\left(\frac{\hat{\lambda}_{qr}^{s,v}}{\hat{\lambda}_{dr}^{s,v}}\right), \left|\hat{\lambda}_r^{v,m}\right| = \sqrt{(\hat{\lambda}_{dr}^{s,v})^2 + (\hat{\lambda}_{qr}^{s,v})^2}$$

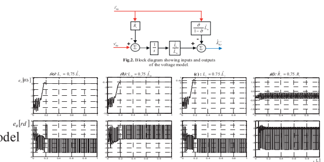

Fig.2. Block diagram showing inputs and outputs of the voltage model

Since the voltage model is essentially an integrator without feedback, it is sensitive to offset and drift errors. Thus a major problem with this open-loop observer is that it lacks feedback necessary for convergence. In practice, a low pass integrator is often used to provide stability.

The resulting estimator requires measured stator current and voltage as input, as indicated in the simplified block diagram in Fig.2. The voltage model is sensitive to parameter stator resistance.

Where $(\hat{R}_s, \hat{L}_r, \hat{L}_s, \hat{L}_m)$ are estimated parameters of dynamic model? The variation effects are calculated by the signals errors as follows: $e_{\lambda} = |\lambda_r| - \left|\hat{\lambda}_r^{v,m}\right|, e_{\theta} = \theta_{\lambda} - \hat{\theta}_{\lambda}^{v,m}$

Proposed method "accurate adaptive algorithm for field oriented control" The accurate adaptive algorithm can be written as:

$$\begin{cases} \hat{\lambda}_{dr}^{s,AAA} = \left(\dfrac{L_sL_r - L_m^2}{L_m}\right) i_{ds}^{s} + \dfrac{L_r}{L_m}\hat{\lambda}_{ds}^{s,v} \\ \hat{\lambda}_{qr}^{s,AAA} = \left(\dfrac{L_sL_r - L_m^2}{L_m}\right) i_{qs}^{s} + \dfrac{L_r}{L_m}\hat{\lambda}_{qs}^{s,v} \end{cases}, \begin{cases} \hat{\lambda}_{ds}^{s,v} = \int\left(u_{ds}^{s} - R_s i_{ds}^{s} - u_{comp-ds}\right)dt \\ \hat{\lambda}_{qs}^{s,v} = \int\left(u_{qs}^{s} - R_s i_{qs}^{s} - u_{comp-qs}\right)dt \end{cases}$$

Where

$$\begin{cases} u_{comp-ds} = K_p\hat{e}_{ds}^{s} + \dfrac{K_p}{T_I}\int \hat{e}_{ds}^{s}dt \\ u_{comp-qs} = K_p\hat{e}_{qs}^{s} + \dfrac{K_p}{T_I}\int \hat{e}_{qs}^{s}dt \end{cases} \quad and \quad \begin{cases} \hat{e}_{ds}^{s} = \hat{\lambda}_{ds}^{s,v} - \hat{\lambda}_{ds}^{s,c} \\ \hat{e}_{qs}^{s} = \hat{\lambda}_{qs}^{s,v} - \hat{\lambda}_{qs}^{s,c} \end{cases}$$

$\hat{\lambda}_{ds}^{s,v}, \hat{\lambda}_{qs}^{s,v}$ are d-axis and q-axis stator flux estimated in stator reference frame using voltage model.

$\hat{\lambda}_{ds}^{s,c}, \hat{\lambda}_{qs}^{s,c}$ are d-axis and q-axis stator flux estimated in stator reference frame using current model.

The rotor flux angle and magnitude estimated by the AAA model $\hat{\theta}_{\lambda}^{AAA,m} = \tan^{-1}\left(\dfrac{\hat{\lambda}_{qr}^{s,AAA}}{\hat{\lambda}_{dr}^{s,AAA}}\right), \left|\hat{\lambda}_r^{AAA,m}\right| = \sqrt{(\hat{\lambda}_{dr}^{s,AAA})^2 + (\hat{\lambda}_{qr}^{s,AAA})^2}$

-The principal objective of this method is to eliminate and reduce the disadvantages of these estimators.

-The accurate adaptive algorithm (AAA) method is based on the exploitation and the combination between the two preceding models

-ones while being based on measurements of stator voltages and currents and on the estimate of rotor speed.

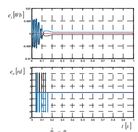

$\hat{R}_s = R_{sn}$; $\hat{R}_s = 0.5 * R_{sn}$ Estimated; $\hat{R}_s = 1.5 * R_{sn}$ Estimated

Fig.? Accurate adaptive algorithm for field oriented control. Parameter deviation from nominal R_s

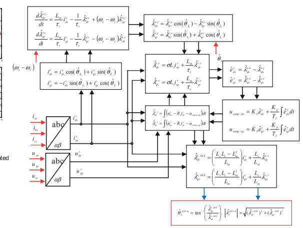

ACTUATION USING PIEZOELECTRIC BIMORPH BEAMS UNDER THE EFFECTS OF STRUCTURAL DAMPING

ZEMIRLINE Adel[1, a], OUALI Mohammed[2, b] and MAHIEDDINE Ali[3, c]

[1] Laboratory of "Mécanique Physique et Modélisation Mathématique" University Yahia Fares of Medea, Algeria,

[2] Laboratory of Research « Structures » Department of mechanic, Faculty of engineering sciences, University Saad Dahleb, Blida Algeria,

[3] Department of science, technology and informatic. University centre of Khemis Miliana, Algeria.

[a] zemirline.adel@yahoo.com, [b] oualimohammed@yahoo.fr, [c] mahieddine.ali@gmail.com

Keywords: Piezoelectricity, Beam, structural damping

Abstract.

Recently, many researches are devoted to using piezoelectric materials to eliminate the vibrations and also to correct the deformations in the structures. Essentially, these structures are made of beams and plates (intelligent structures or smart structures). They are also used in the actuation field (piezoelectric bimorph actuators). In this paper, we study and analyze the dynamic behavior of bimorph beams by taking into account the effects of structural damping, shear deformation and piezoelectricity. We establish a numerical model in direct relationship with the studied cases. The present results are confronted with those of the literature.

Introduction

The use of so-called piezoelectric materials contributed positively in the improvement of active vibration control and in the design of new actuators. J. H. Yim and S. Y. Cho[1] presented a study on the damping behavior of a laminate composed of two piezoelectric layers and a core of viscoelastic material. They investigate the influence of the thickness and the length of the core of viscoelastic on the structural damping coefficient. J. Cheng, et all [2] used a higher order theory shear deformations to model and analyze a laminate composed of a superposed of piezoelectric layers with random polarization, based on the principle of Hamilton generalized they deduced the fundamental equations of piezoelectric composites. J. M. Simões Moita, et all [3] have addressed the problems of forced vibrations and resonances in structures (beams and plates) composed of piezoelectric layers serving as the piezoelectric actuators and sensors, based on a theory of a higher order deformation. A finite element models are proposed for the calculation of displacements. A. Mukherjee and A. Saha Chaudhuri [4] demonstrated the effect of large deformations on the piezoelectric materials and structures subjected to loads varying in time. The equation of Von Karman and Tiersten law is adopted in the analysis of deformations of beams, and finite element modeling based on the theory of first-order of shear deformation is used.

In the present work, we study the dynamic behavior of bimorph beam subjected to a sinusoidal electric field to produce a specific actuation.

Theoretical study

The piezoelectric equations are:

$$\begin{cases} \sigma_p = Q_{pq}\varepsilon_{pk} - e_{pk}E_k \\ D_i = e_{iq}\varepsilon_q + \bar{\varepsilon}_{ik}E_k \end{cases} \tag{1}$$

$\sigma, Q, e, E, D, \bar{\varepsilon}$ Respectively are the stress, elastic coefficient, electric field, electric displacement coefficient and permittivity. The relations between the displacements and deformations in case of beams are: [1, 5, 6]

$$\begin{cases} \varepsilon_x = u_{,x} - z\psi_{,x} \\ \gamma_{xz} = w_{,x} - \psi \end{cases} \tag{2}$$

Where are deformations and *w* axial, rotation and vertical displacement of the medium fibre. Taking into account the relationship between the matrix of the piezoelectric coefficients [e] and dielectric coefficients [d] and by replacing (Eq1) in this latest we obtain:

$$\{\sigma\} = [Q](\{\varepsilon\} - [d]\{E\}) \tag{3}$$

$$\begin{Bmatrix} \sigma_x \\ \gamma_x \end{Bmatrix} = \begin{bmatrix} \overline{Q}_{11} & 0 \\ 0 & \overline{Q}_5 \end{bmatrix} \left(\begin{Bmatrix} \varepsilon_x \\ \gamma_y \end{Bmatrix} - \begin{Bmatrix} d_3 \\ 0 \end{Bmatrix} E_3 \right) \tag{4}$$

The expressions of the kinetic energies and deformations in this case are respectively denoted by *T* and *U* [5,7,10,11].

$$T = \frac{1}{2}\rho\int \{\dot{u} \;\; \dot{w} \;\; \dot{\psi}\} \cdot [\overline{T}] \cdot \begin{Bmatrix} \dot{u} \\ \dot{w} \\ \dot{\psi} \end{Bmatrix} b_p dx$$

$$U = \frac{1}{2}\int_V (\varepsilon\sigma - DE)dV = U_{Elas} + U_{Piezo} + U_{Diélec}$$

We consider a bimorph in antiparallel configuration **[**5**,** 11**].** This means that the electric field applied on both layers have the same direction, and the poling of the top layer have the same orientation with the electric field. The poling of the bottom layer is in the opposite orientation of the electric field. We consider the following scheme (Fig 1 [5])

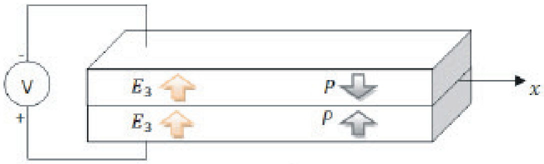

Figure1 : antiparallel configuration

Finite element formulation:

We define interpolation functions as continuous functions with polynomial type like:

$$\{u_i \quad u_j\}^t = [N_u]\{q\}\,;\{w_i \quad w_j\}^t = [N_w]\{q\}\,;\{\psi_i \quad \psi_j\}^t = [N_\psi]\{q\}$$

$$\phi^B = [N_\phi^B]\{\phi_1 \quad \phi_2 \quad \phi_3\}^t\,;\phi^T = [N_\phi^T]\{\phi_1 \quad \phi_2 \quad \phi_3\}^t$$

Where, the exponent t denotes the transpose T,B denotes the top and bottom layer, and N_i the shape functions. Finally, we have these matrices:

$$T = \frac{1}{2}\{\dot{q}\}^t[M_{uu}]\{\dot{q}\} \tag{5}$$

$$U_{Elas} = \frac{1}{2}\{u\}^t[K_{uu}]\{u\} \tag{6}$$

$$U_{Piezo} = \frac{1}{2}\{q\}^t[K_{u\phi}]\{\phi\} + \frac{1}{2}\{\phi\}^t[K_{\phi u}]\{q\} \tag{7}$$

$$U_{Diéle} = \{\phi\}^t[K_{\phi\phi}]\{\phi\} \tag{8}$$

Equation of motion:

By using the Lagrange formalism we obtain the equations of motion which can be written in matrix form:

$$[M]\cdot\{\ddot{q}\}+[C]\{\dot{q}\}+[K]\cdot\{q\}=\{F\} \tag{9}$$

$[M]$, $[K]$, $[C]$and $\{F\}$

and respectively are inertia, rigidity, dissipation matrices and force vector.

$$[M] = \begin{bmatrix}[M_{uu}] & [0]\\ [0] & [0]\end{bmatrix} \qquad [K] = \begin{bmatrix}[K_{uu}] & [K_{u\phi}]\\ [K_{\phi u}] & [K_{\phi\phi}]\end{bmatrix}$$

Results

We use MATLAB software for our various calculations. NEWMARK method is used for solving the system of equations of motion, the results are obtained and compared to those of G. Smits [11] for the analytic solution and M. Ouali, A. Zemirline [5]for the numeric solution. By comparing the results it is assumed that the program developed is exploitable.

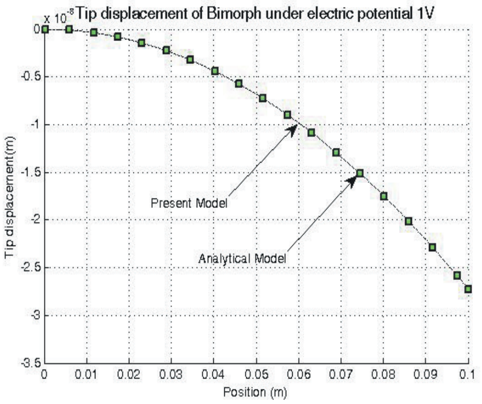

Figure 2 a: comparison of results for vertical displacement.

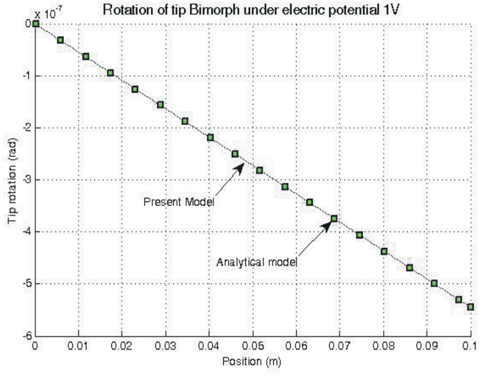

Figure 2 b: comparison of results for rotation

We consider a cantilever bimorph composed with two layers made of a PVDF see Figure 3 and table 1 for physical properties and geometric configuration, . To study the actuation of the bimorph we apply a sinusoidal electric field on the top and bottom electrodes like:) and) where is the signal dephasing:

PVDF properties	
ρ	$1800\ [\mathrm{Kg/m^3}]$
E_1, E_2	$2 * 10^9 [\mathrm{N/m^2}]$
G_{12}	$7.75 * 10^8 [\mathrm{N/m^2}]$
ν	0.29
d_{31}	$2.2 * 10^{-11} [\mathrm{C/N}]$
$\bar{\bar{\varepsilon}}_{11}$	$1.62 * 10^{-11} [\mathrm{F/m}]$
$\bar{\bar{\varepsilon}}_{22}$	$1.62 * 10^{-11} [\mathrm{F/m}]$
$\bar{\bar{\varepsilon}}_{33}$	$1.62 * 10^{-11} [\mathrm{F/m}]$

Table.1 PVDF properties

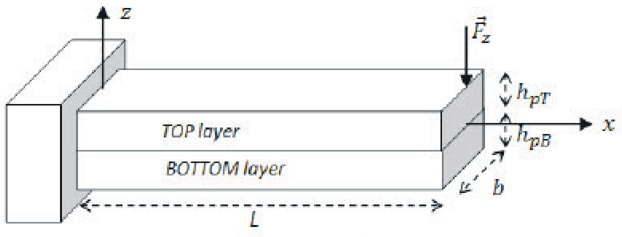

Figure3 : Dimension of Bimorph.

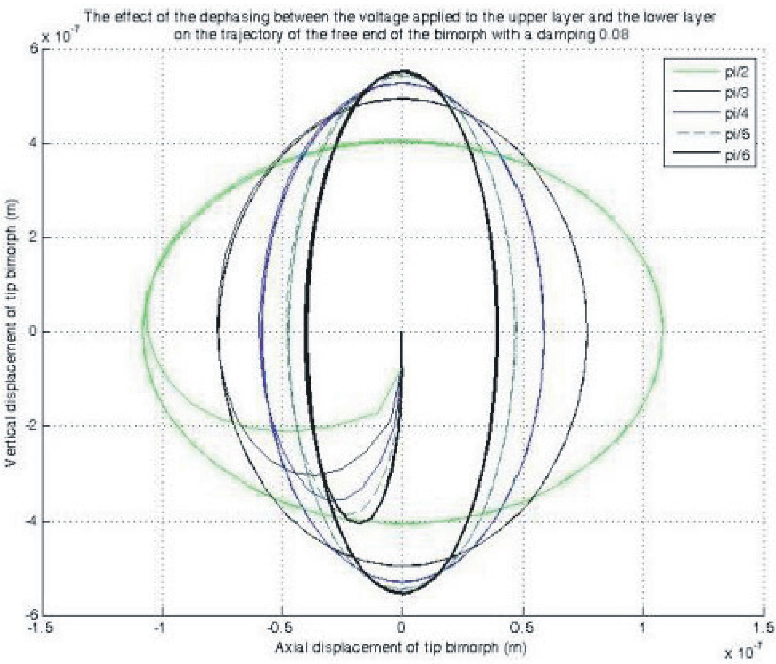

Figure.4 a : effect of dephasing between upper and lower applied voltage on the trajectory of the tip bimorph in case of 0.08 structural damping coefficient

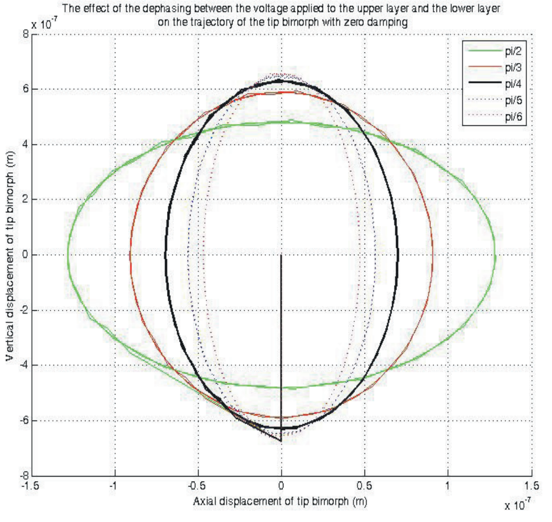

Figure.4 b: effect of dephasing between upper and lower applied voltage on the trajectory of the tip bimorph without structural damping coefficient.

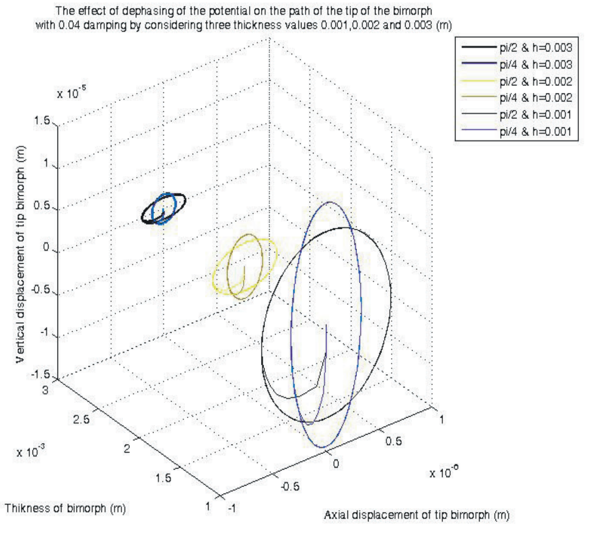

Figure.5 effect the thickness of the beam with the consideration of 2 values of dephasing on the trajectory of the tip bimorph.

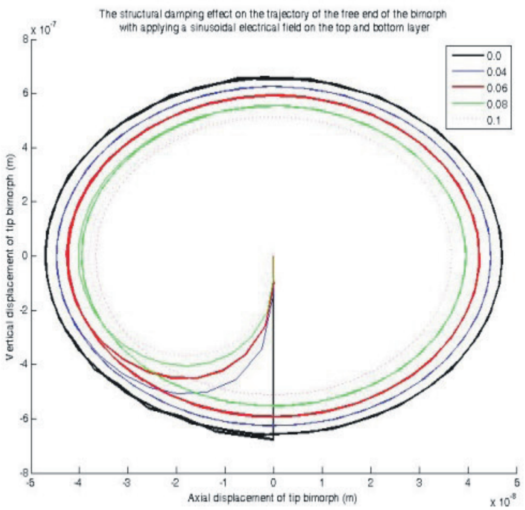

Figure 6, the trajectory of tip beam with structural damping coefficient.

Conclusion

We present in this paper the dynamic behaviour of the bimorph beams with the effects of: structural damping, shear deformation and piezoelectricity. A finite element model has been developed for a beam composed by tow piezoelectric layers subjected to a sinusoidal electric field. The results obtained are confronted with those of the literature.

It seen clearly the effect of the signal dephasing on the trajectory of the tip beam with and without structural damping (Fig 4 a/b), we can make several form of trajectory by changing dephasing value. We can obtain better actuation since the thickness of beam is as well as smaller; this can feel in the Fig 5. In Fig 6, the trajectory of tip beam decreases when the structural damping increase which induce an actuation lost.

References

J. H. Yim, S. Y. Cho, A study on material damping of 0_ laminated composite sandwich cantilever beams with a viscoelastic layer *Composite Structures* 60 (2003) 367–374.

J. Cheng, B. Wang A theoretical analysis of piezoelectric/composite anisotropic laminate with largeramplitude deflection effect, Part I: Fundamental equations. *International Journal of Solids and Structures* 42 (2005) 6166–6180.

J. M. Simões Moita, C. M. M. Soares Active control of forced vibrations in adaptive structures using a higher order mode *Composite Structures* (2005). ISSN 0263-8223

A. Mukherjee et A. Saha Chaudhuri Nonlinear dynamic response of piezolaminated smart beams *Computers and Structures* 83 (2005) 1298–1304.

M. Ouali,A. Zemirline,A. Mahieddine, Application of piezoelectricity on sandwich beams under the effect of structural damping**,** *Advanced Materials Word Congress*, Cesme Izmir, Turkye, September 16-19 ,2013.

A. Mahieddine, J. Pouget, M. Ouali. Modeling and analysis of delaminated beams with integrated piezoelectric actuators *C. R. Mecanique Académie des sciences*. 338 (2010) 283–289.

J. Courban Théorie de l'élasticité *techniques de l'ingénieur*, traité science fondamentales. A 305-(1-31).

A. Mukherjee, A. Saha Chaudhuri Nonlinear dynamic response of piezolaminated smart beams (2005). *Computers and Structures* 83, 1298–1304.

A. Mahieddine, M. Ouali. Analysis of delaminated composite plates*, Advanced Materials Research Vol. 686 (2013) pp 104-108, (2013) Trans Tech Publications.*

A. Mahieddine, M. Ouali. Modeling and analysis of beams with delamination, *Int. J. Model. Simul. Sci. Comput.* 01, 435 (2010), Volume 01, Issue 03, September 2010.

J. G. Smits, S. I. Dalke. The constituent equations of piezoelectric bimorphs *Sensors and Actutators* A, 28 (1991) 41-61

ANALYSIS METHODS FOR THE DETERMINATION OF ENERGIES ACTIVATION AND THE STUDY OF THE PRECIPITATION REACTIONS IN AL-CU ALLOYS

H. Bensouyad

Département de Médecine Dentaire, Faculté de Médecine, Université Constantine 3, Algérie

E-mail: ben_hanine@yahoo.fr

Abstract

The kinetics of transformation (precipitation and dissolution of the precipitates) is always allied to the concepts of energies activation and about the order of reaction,; The interest of this study is justified by the existence of a significant number of methods of isoconversionnelle analysis, more or less sophisticated like that of Kissinger-Akahira-Sunose (KAS) [1-2], Ozawa-Flyn-Wall (OFW) [3-4] and that of Boswell [5], which makes difficult the choice of a method particular. The goal of the use of these models of analysis would be to find a description proportioned of the development of the reaction according to time and temperature. In this work we have interested by the influence of the heating rates on the non isothermal transformations in Al- 4,5 % Cu. For this the samples of this alloys have heated with different rates (V = 0.5, 1, 2, 3, 4, 5, 6, 7 °C/ min) from room temperature until 520°C using the differential scanning calorimetry (DSC) and we will calculate the energy activation of the precipitated phases b and b' by various isoconversionelles methods.

Keywords: Precipitation Innovation, calorimetry, energy activation, order of reaction n, isoconversionelles methods.

1. Introduction

Differential scanning calorimetry (DSC) have been applied extensively to the analysis of light metals, especially Al based alloys. Differential scanning calorimetry is used for analysis of solid state reactions, such as precipitation, homogenisation, devitrivication and recrystallisation; and solid–liquid reactions, such as incipient melting and solidification, are studied by differential scanning calorimetry. In producing repeatable calorimetry data on Al alloys, sample preparation, reproducibility and baseline drift need to be considered in detail. Calorimetry can be used effectively to study the different solid state reactions and solid–liquid reactions that occur during the main processing steps of Al based alloys solidification, homogenisation, precipitation). Quantitative analysis of the kinetics of reactions is assessed through reviewing the interrelation between activation energy analysis methods, equivalent time approaches, impingement parameter approaches, mean field models for precipitation, the Johnson–Mehl–Avrami–Kolmogorov model, as well as novel models which have not yet found application in calorimetry. Differential scanning calorimetry (DSC) represents a rapid qualitative and quantitative means for precipitate characterization in aluminium alloys, this technique can improve understanding of the thermodynamics and kinetics of the precipitation processes. In the present work a qualitative as well as quantitative interpretation has been obtained of the precipitates developed in supersaturated Al-Cu solid solutions. In this work we were interested to study the kinetics of anisothermal precipitation of the phase's b and b' in alloy Al-4,5 % weight. Cu where each one of these phases can be detected according to the heat treatment applied and selected measurement technique.

2. Materials and experimental methods:

In this work we used the analysis calorimetric differential (DSC) (apparatus SETARAM 131) which makes it possible to measure the releases and absorptions of flow of energy of a material during a thermal cycle which consists a heating from 20°C at 520°C with various rates (V=0.5, 1, 2, 3, 4, 5, 6, 7 °C/min) followed by a holding of 5–10 min at this temperature and a cooling until room temperature, with the same rates .

The sequence of precipitation in alloys of the system Al-Cu is [1-2]:

Supersaturated solid solution (S.S.S) $\rightarrow$ Zones G.P. $\rightarrow$ Phase θ'' $\rightarrow$ Phaseθ' $\rightarrow$ the equilibrium cycle θ (Al_2Cu)

Where q' and q'' is the metastable phases of transition

2.1. Kinetic theory:

The theory of this work is based on the equation of kinetics:

$$\frac{d\alpha}{dt} = f(\alpha) * k(T) \rightarrow (1) \qquad\qquad k = k_0 \exp\left(-\frac{E_a}{RT}\right) \rightarrow (2)$$

Where: E_a is the energy activation of the reaction, k_0 the exponential pre factor and R the gases constant.

To calculate E_a, we will use the following isoconversionnelle method:

2.1.1. Method of Kissinger-Akahira-Sunose (KAS) :

This method rests on the assumption according to which, during the rise in temperature, the reaction passes by a maximum before decreasing [1, 2], it based to the following relation:

$$\ln\left(\frac{T_p^2}{V}\right) = \frac{E_a}{RT_p} + c \qquad (3)$$

Where $$c = \ln\left(\frac{E_a}{Rk_0}\right) \qquad (4)$$

2.2. Determination of the order of reaction (n) by the Matusita Method's:

Starting from the traditional equation of Johnson-Mell-Avrami-Kolmogorov (JMAK) Matusita and Sakka [6] found that the equation of kinetics becomes then:

$$\ln\left[\ln(1-\alpha)^{-1}\right] = -n.\ln V + Const \qquad (7)$$

Where the transformed fraction a is given by the relation:

$$\alpha = {S_T}/{S} \qquad (8)$$

Where: S is the total surface of the peaks and S_T is the surface partial of the peaks.

3. Results and discussion:

The DSC Curves obtained during the heating with various rates of the homogenized and quenched samples (fig.1) show two endothermic peaks and an exothermic peak which present three effects respectively related on dissolution of zones G.P, the formation and dissolution of the phases q' and q result already observed by other authors [7,8]. Because we now during the formation of a phase, the variation of the flux are exothermic, during dissolution the variation is b endothermic and the surface of the peak represents an enthalpy of formation (or of dissolution). Each phase has an enthalpy and a temperature of formation which depends on the scanning rate.

The first endothermic peak appears in the interval [93-241°C] a peak exothermic split appears in the interval [241-378 ° C] with a maximum located around 349 ° C, which is due to the precipitation of two phases (q 'and q) this peak followed directly from a peak endothermic split in the interval of temperature [378-514 ° C] with two minimum located around 405 ° C and 483 ° C, represents the dissolution of these two phases q 'and q. the increase of the heating rate leads to the increase in the amplitude of the various peaks, with a shift of the thermo-grams towards the high temperatures.

The curves of DSC obtained for the various heating rates present three effects related to dissolution of zones G.P., the formation and the dissolution of the phases q' and q.

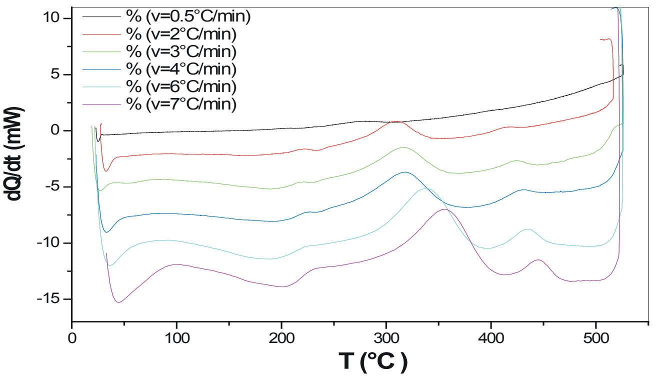

Fig.1. Curves DSC of alloy Al- 4,5% Cu homogenized, quenched and heated with various rates

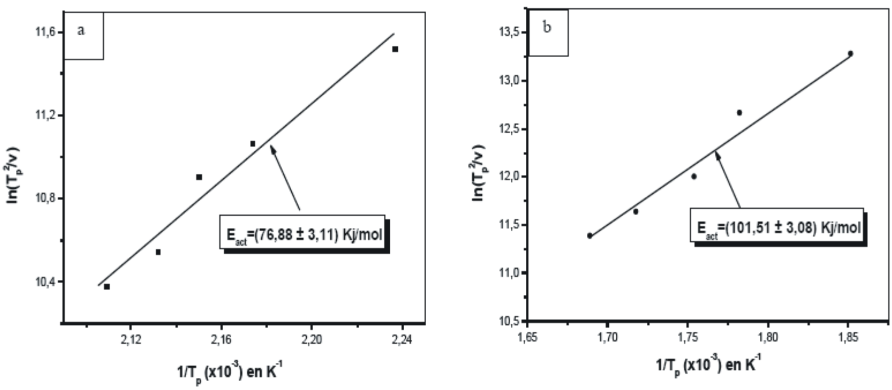

Fig. 2. Curves of Kissinger due to: (a) dissolution of G.P. zones and (b) formation of *q and q.*

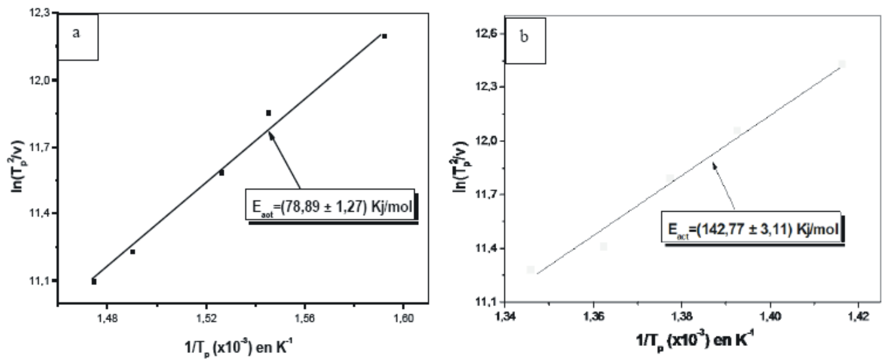

Fig. 3. Curves of Kissinger due to: (a) dissolution of *q* and (b) dissolution of *q*

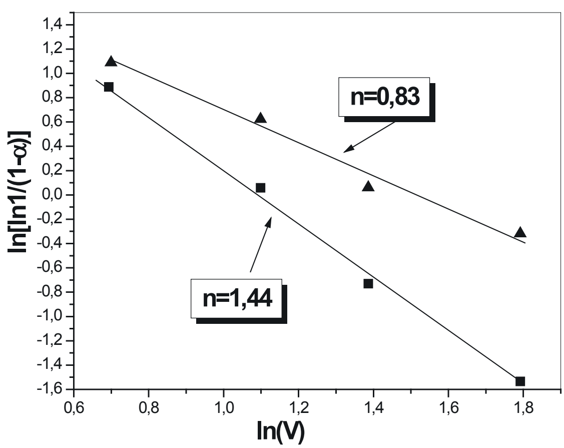

Fig.4. Order of reaction n due to: (▲) dissolution of G.P. zones and (■) formation of q and q.

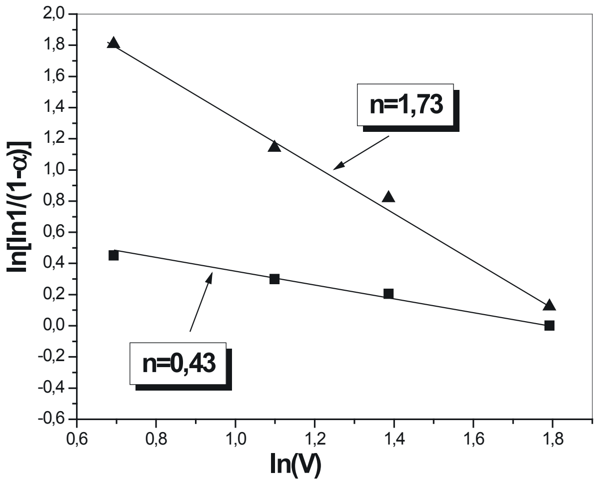

Fig.5. Order of reaction n due to: (▲) dissolution of q and (■) dissolution of q'

4. Conclusion:

The study of the kinetics of precipitation made it possible to illustrate the following conclusions:

- Peaks of precipitation and dissolution of the phases (q' and q) are shifted towards the high temperatures with an increase in their amplitude;
- The increase in the width of the peaks with the increase of the heating rate testifies to the increase of the quantity of precipitates formed during the anisotherme annealing;
- The shift of the peaks is due to the fact that precipitation takes seat with difficulty and this shift can be explained by delays of the formation and dissolution of the phases;
- For the formation of the phases q' and q we have found that the E_{act} obtained is of (101,51 ± 3,08) Kj/mole and for the order n=1,44 ; this value close to 1,5 indicates that the mechanism of precipitation occurs everywhere through alloy, and that the precipitates grow in all the directions, in more this value of n suggests that this type of precipitation believes on the existing pre germ;
- For the dissolution of the phases q' and q it was found that the E_a obtained for this process is of (78,89 ± 1,27) Kj/mol for q' and (142,77 ± 3,11) Kj/mol for q ; this energy is consumed for the dissociation of the large precipitates and the migration of the atoms of aqueous solution in the matrix; and for the order n of reaction is equal to 1,73 for q and 0,43 for q; this values suggests that the speed of dissociation is constant and also affirm that copper diffuses and dissolves through all the matrix .

In parallel, it seems that the use of the energy activation connects for the estimate of the parameters is indeed very interesting.

5. References:

[1] H. E. Kissinger, Analyt. Chem,.Vol. 29, p 1702 (1957).

[2] T. Akahira and T. Sunose, Trans. Joint Convention of Four Electrical Institutes, p. 246 (1969).

[3] T. Ozawa, J. Therm. Anal. Vol. 2, p 301 (1970).

[4] H. Flynn and L. A. Wall J. Polym. Sci., Vol 4, p. 323 (1966).

[5] P. G. Boswell, J. Thermal Anal., Vol. 18, p 353 (1980).

[6] Kazumasa Matusita and Sumio Sakka, Journal of Non-Crystalline Solids, Vol 38 et 39.

[7] M. Bouchear, PhD Thesis State, University Mentouri-Constantine, Algeria (2000).

[8] R. Mechiakh Thesis Magister, University Mentouri-Constantine, Algeria (2005).

MODEL-BASED ROBUST TRAJECTORY CONTROL OF 6-DOF STEWART PLATFORM

Dr. Mohammad Al-Khedher

Mechatronics Engineering Department

Faculty of Engineering Technology, Al-Balqa' Applied University

P.O.Box 15008, Amman 11134, Jordan

Email: mohalkhedher@hotmail.com

***Abstract*:** A 6-DOF Stewart platform is designed and constructed as a parallel mechanism that consists of a rigid body moving plate, connected to a fixed base plate through six independent kinematics legs. The mechanism is implemented to achieve high precision tracking performance for an external control command using an accurate orientation sensor. A Reference trajectory is generated based on the feedback sensing elements of each actuator based on inverse kinematic and inverse dynamic models, several control schemes are implemented to achieve highest performance of the controller and the system. To ensure the reliability of the control model a virtual environment of the system has been built to verify the physical limits of the body motion. The hardware structure is tested and showed high performance and accuracy.

***Keywords*:** Stewart platform; Robust Control; Model-based control; Virtual model; Modeling and simulation.

***Bio*:** Mohammad A. Al-Khedher, Associate Professor, Head of Mechatronics Department at Al-Balqa Applied University, received his BSc in Mechatronics Engineering from JUST, Jordan, MSc in MechatronicsnEngineering from American university of Sharjah, UAE and PhD in Mechanical Engineering from Washington State University, USA. He joined Al-Balqa Applied University in 2007. His research interests are: Robotics, intelligent systems, nanotechnology and MEMS.

I. Introduction

A parallel robot is a closed kinematics chain where all legs are connected by a parallel connection. Parallel kinematic manipulators have better performance compared to serial robots that consist of a number of serial rigid links. The serial structure suffers from several disadvantages such as low precision and low power-to-weight-ratio. The parallel robot architecture eliminates these disadvantages by giving a high degree of accuracy, high operation speeds or accelerations, high load capacity, high rigidity, and high stiffness [1, 2].

A well-known parallel robot is Stewart platform. The Stewart platform is basically a 6-Degree of freedom mechanism as shown in figure 1. It is a parallel mechanism that consists of a rigid body moving plate, connected to a fixed base plate through six independent kinematics legs. These legs are identical kinematics chains, couple the moveable upper and the fixed lower platform by universal or spherical joints for the upper. Each leg contains a precision ball-screw assembly and a DC-motor. Thus, length of the legs is variable and they can be controlled separately to perform the motion of the moving platform [3]. This work aims to design, develop and control a Stewart platform through the study the Stewart platform mechanics and kinematics. The entire platform model will be simulated in MATLAB.

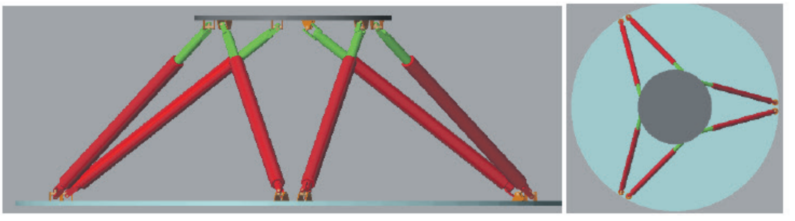

Figure 1. Stewart platform Mechanism, lateral and vertical views.

II. Structure Description

A Stewart platform consists of an upper and lower plates, the lower plate is usually bigger than the upper one, six legs connected between them. The leg subsystem has an upper and lower parts connected by a prismatic joint. The prismatic joint is actuated by the given force from the controller. Moreover, in order to observe the errors, a joint sensor is attached to the joint. There are also 6 spherical joints which connect the leg to the base and top plates. Also, 6 prismatic joints connect the upper to the lower legs.

The linear actuators have an internal mechanism that allows changing the length of each individual leg. The desired position and orientation of the mobile platform is achieved by combining the lengths of the six legs, transforming the six transitional DOF into three displacement vector and three orientation angles [4].

III. Kinematics Analysis

The motion analysis of the Stewart platform is achieved by using inverse kinematic analysis to move it to a desired position and direction. To move top platform from one position to another, to reach the desired position and orientation, the control algorithm will give the orders to generate the required motion for each leg actuator.

As shown in figure (2), positions of the base and the platform are uniquely defined by the coordinates of the six joints that connect them with links. The six points are usually chosen to form an irregular hexagon in one plane, figure (3). [5]

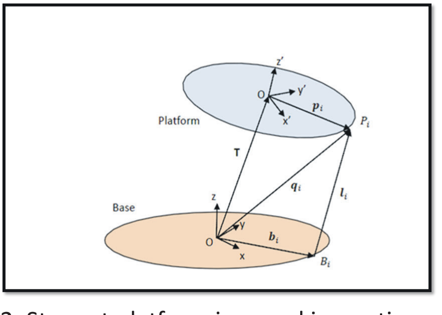

Figure 2. Stewart platform inverse kinematics analysis.

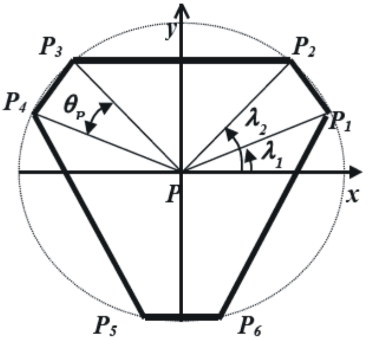

Figure 3. The base and the platform as hexagon-shaped structure.[6]

In figure (3), we define the platform coordinate system (**P)** and base coordinate system (**B)**. The $\mathbf{p}_i$ vector represents the position of joint connecting the top platform to the i-th link, with respect to **P**. ($\mathbf{b}_i$**)** Vector describes the joint position of the i-th actuator connected to the base. All links are between upper platform and base have length $\mathbf{L}_i$. [6]

The transformation vector between the stationary base and the platform is:

$$\mathbf{q}_i = \mathbf{H}\,\mathbf{p}_i \tag{1}$$

where: **H** is the transformation matrix:

$$\mathrm{H} = \begin{bmatrix} \mathbf{R}_{3x3} & \mathbf{T}_{3x1} \\ 0_{1x3} & 1 \end{bmatrix} \tag{2}$$

where **R** denotes a rotation matrix and **T** a translation vector. Three angular displacements define the orientation of the platform with respect to the Base and thus **R**: rotate an angle ψ (yaw) around the z-axis, rotate an angle θ (pitch) around the y-axis, rotate an angle φ (roll) around the x-axis. The rotation matrix of the platform relative to the base is: [7]

$$ {}_B^P R = R_z(\psi).R_y(\theta).R_x(\varphi) $$

$$= \begin{pmatrix} cos\psi cos\theta & -sin\psi cos\varphi + cos\psi sin\theta sin\varphi & sin\psi sin\varphi + cos\psi sin\theta cos\varphi \\ sin\psi cos\theta & cos\psi cos\varphi + sin\psi sin\theta sin\varphi & -cos\psi cos\varphi + sin\psi sin\theta cos\varphi \\ -sin\theta & cos\theta sin\varphi & cos\theta cos\varphi \end{pmatrix} \tag{3}$$

Consider the radius of the platform $\mathbf{r}_P$, and the angle between the first two joints is θ_P. In the same way, $\mathbf{r}_B$ is the radius of the base, and θ_B the angle between the first two joints in the base. As in figure (3), finding λ_i and Λ_i for i=1,2,...,6 , we obtain: [8]

$$\Lambda_i = 60^o \cdot i - \frac{\theta_B}{2}; \quad \lambda_i = 60^o \cdot i - \frac{\theta_P}{2} \quad \text{for i} = 1,3,5 \tag{4}$$

$$\Lambda_i = 60^o \cdot i + \frac{\theta_B}{2}; \quad \lambda_i = 60^o \cdot i + \frac{\theta_P}{2} \quad \text{for i} = 2,4,6 \tag{5}$$

Therefore:

$$\mathbf{p}_i = [r_P \cos\lambda_i \quad r_P \sin\lambda_i \quad 0 \quad 1]^T \tag{6}$$

$$\mathbf{b}_i = [r_B \cos\Lambda_i \quad r_B \sin\Lambda_i \quad 0 \quad 1]^T \tag{7}$$

The inverse kinematics can be formulated so as to determine required actuator lengths for a given position of the platform with respect to the base. The length of the link $\mathbf{L_i}$ are calculated as: $\mathbf{L_i}=\mathbf{q_i}-\mathbf{b_i}$. [9]

IV. Computer Aided Design of the Stewart Platform

The platform is virtually designed in SolidWorks environment to simulate and optimize the model parameters. This model is translated into MATLAB using Simmechanics toolbox. The drive and control algorithms are accomplished by Matlab software, the resulted control command are performed in the solidworks model as shown in figure (4).

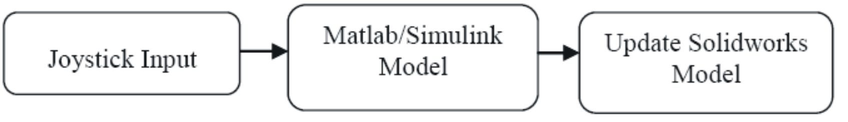

Figure 4. Simulation eviroment

The entire mechanical structure of the Stewart platform is designed using SolidWorks as shown in figure(5).

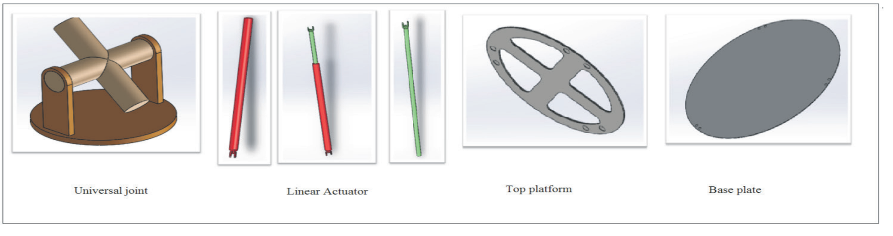

Figure 5. Stewart Platform main components.

Figure (6) shows Stewart platform after assembling all components together.

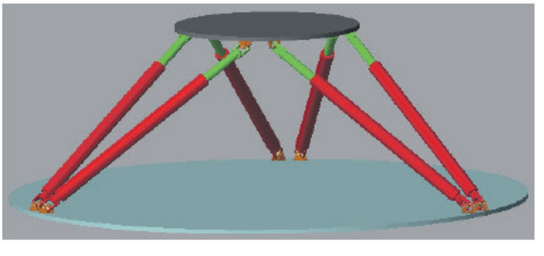

Figure 6. Assembled Stewart platform.

V. Modeling and Simulation of Physical Plant

In this study, the entire modeling and simulation is achieved by using SimMechanics toolbox in Matlab. SimMechanics is a block diagram modeling environment for the engineering design and simulation of rigid body machines and their motions, using the standard Newtonian dynamics of forces and torques. In the SimMechanics, it is possible to model and simulate mechanical systems by specifying bodies and their mass properties, their possible motions, kinematic constraints, and coordinate systems, and initiate and measure body motions. Also, Matlab is used to control the movement of the platform according to the Joystick command signal, figure (6).

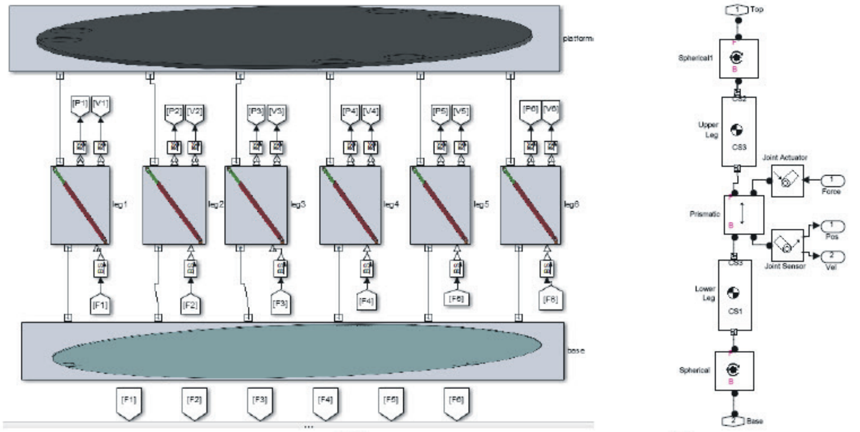

(a) (b)

Figure 7. (a) Simmechanics model of the Stewart Platform. (b) One leg detailed model.

VI. Controller Design

A controller is designed to control the platform to move from an initial position to a desired position and orientation. It will generate required forces for each linear actuator. Position and trajectory control of the platform can be reduced to leg position control after inverse kinematic and path planning algorithms[10]. The control error $\mathbf{E_r}$ for each leg length is calculated as:

$$\mathbf{E_{ri} = q_i - b_i - ln_i = Hp_i - b_i - ln_i} \qquad (8)$$

Where $\mathbf{ln_i}$: nominal (reference) distance between the top and base attachment points.

Control algorithms designed in Matlab Simulink environment with using "target for use with Arduino hardware" library. The figure below shows our control algorithm.

A simple PID controller calculates proportional, integral and derivatives of the body sensor inputs and desired ones as:

$$\mathbf{F_i = K_p . E_r + K_i . \int E_r + K_d . dE_r/dt} \qquad (8)$$

The output of the controller $\mathbf{F_i}$ applied to the physical plant as actuating forces as shown in figure (8).

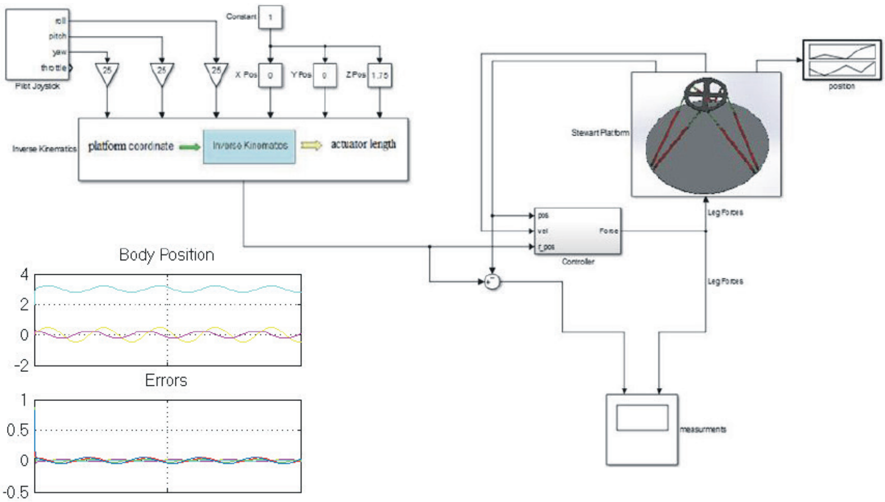

Figure 8. A closed loop system of Stewart platform using inverse kinematics and PID controller.

VII. Hardware Implementation

The mechanical structure of Stewart platform is designed to achieve flexibility in the 6 degrees of freedom. The dimensions of the platform and the base are chosen such that the whole mechanism will be easy to move [11]. The platform and base are made out of iron material for rigidity, the base is 45.8 cm in radius and 6 cm thick and the platform is 24.3cm in radius and 7.5cm thick, figure (9).

Figure 9. Assemebled structure of stewart platform.

Universal joints, with 2 DOF, connect each actuator to the base plate, and spherical joints,with 3 DOF, connect the actuators to the platform. Table(1) shows a summary of the hardware specification in the chosen model.

Table 1. The hardware design specifications for the Stewart Platform.

Degrees- of- freedom	6
Number of joints and type	6 universal 6 spherical 6 prismatic
Translation accuracy	5 mm
Translation range	x-axis ±0.2m y-axis ±0.22m z-axis 0.5 - 0.81 m
Rotation range	x-angle ±20^{o} y-angle ±20^{o} z-angle ±50^{o}

The control and power circuits included as PC with Matlab environment, Arduino Mega 2560, 6 H-bridge, UM6-LT Orientation Sensor, 12VDC wall adapter, 5v adapter, USB to serial adapter.

VIII. Simulation Results

The visualization of Simmechanics model shows the motion of the platform from different views. The Stewart platform is tested using a real flight simulator to verify the model mechanics and control capabilities as shown in figure (10), it shows the motion of the Stewart along with the motion of an air plane, and both controlled using a joystick. We used Microsoft X plane for flying trainers.

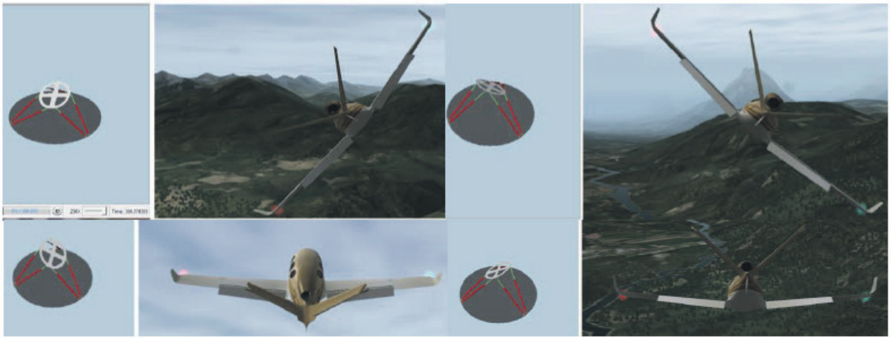

Figure 10. Several positional cases of Stewart platform verified by a real flight simulator.

Conclusion

In this research, A Stewart Platform manipulator is designed, simulated, implemented and controlled. The Stewart Platform has better precision and stiffness if compared to conventional serial manipulators. The inverse kinematics is derived and simulated to achieve accurate positioning. The platform position is calculated in terms of actuators linear extension.

The entire model is simulated and controlled using Matlab software using a PID controller. The visualization of the resulted model is achieved by linking soildworks 3D model with Matlab using Simmechanics toolbox. The hardware is implemented to validate the simulation results. The control circuit included microcontrollers to command the linear actuators using Matlab- Arduino interface. The results were remarkable, we achieved accurate positioning of the platform compared to the modeling results and visualized model.

References:

[1] Tsai L.W., Robotic Analysis: The Mechanics of Serial and Parallel Manipulators, John-Wiley & Sons, New York, 1999.

[2] Merlet J.P., Parallel robots (2nded.), Springer, France, 2006.

[3] Dasgupta B.,and Mruthyunjaya T.S, "The Stewart platform manipulator: A review", Mechanism and Machine theory, Vol. 35, pp. 15-40, 2000.

[4] Fitcher E.F., "A Stewart Platform-Based Manipulator: General Theory and Practical Construction", the International Journal of Robotic Research, Vol 5 No 2, pp. 157-182, 1986.

[5] Geike T., and McPhee J., "Inverse dynamic analysis of parallel manipulators with full Mobility", Mechanism and Machine Theory, 38, pp. 549–562, 2003.

[6] Lazarevic Z., "Feasibility of a Stewart Platform with Fixed Actuators as a Platform for CABG Surgery Device", Master's Thesis, Columbia University, Department of Bioengineering, 1997.

[7] Lou Y., Liu G., Xu J., and Li Z., "A general approach for optimal kinematic design of parallel manipulators," In Proceedings of IEEE International Conference on Robotics and Automation, pp. 3659-3664, 2004.

[8] McAcree P.R., and Daniel R.W., "A Fast, Robust Solution to the Stewart Platform Forward Kinematics", Journal of Robotic Systems, vol. 13(7), pp. 407-427, 1996.

[9] Nguyen C.C., Antrazi S.S., Zhou Z-L, and Campbell Jr C.E., "Adaptive Control of a Stewart Platform-Based Manipulator", Journal of Robotic Systems, vol. 10(5), pp. 657-687, 1993.

[10] Pugazhenthi S., Nagarajan T., and Singaperumal M., "Optimal trajectory planning for a hexapod machine tool during contour machining", Journal of Mechanical Engineering Science, vol. 216, pp.1247-1257, 2002.

[11] Gosselin C., "Determination of a workspace of 6-DOF parallel manipulators", Journal of Mechanical Design, vol. 112, pp. 331–336, 1990.

IMAGE GUIDED STEERABLE PROBE PATH PLANNING

Minou Kouhsoltani [1], Sohrab Khanmohammadi [2]

[1] Faculty of Electrical and Computer Engineering,University of Tabriz, Tabriz, Iran;

Email : kouhsoltani@tabrizu.ac.ir

[2] Faculty of Electrical and Computer Engineering,University of Tabriz, Tabriz, Iran;

Email : khan@tabrizu.ac.ir

Abstract: With the recent advances in medical imaging modalities, minimally invasive surgeries (MIS) for performing percutaneous procedures are developing increasingly that give benefits of reduced trauma, decreased morbidity, less pain and shorter recovery time. The MIS requires the insertion of surgical tools such as needles, electrodes and catheters inside the vessels and colons. The tool should precisely approach anatomical structures based on preoperative medical images, while avoiding sensitive tissues and arteries. Steerable catheters are routinely deployed in the treatment of cardiac arrhythmias. The complicated surgical procedure is time consuming and requires high accuracy and dexterity of surgeon, which additionally exposes the patient as well as the interventionalist to the ionizing radiation. With the help of medical robots stable motions with good geometric accuracy can be achieved. In this paper, an Image guided path planning method is developed for steering the catheter inside the artery based on the geometric constraints of the workspace and pre-operative 2D MRI image. Due to the distinct characteristics of the catheter and workspace, Rapidly-exploring Random Trees method is elaborated for path planning of catheter. The results verify the good performance of the proposed method.

Keywords: Rapidly-exploring random tree method, path planning, workspace determination, catheter.

1. Introduction

Recent advances in medical imaging modalities enabled interventionalists to deploy Minimally Invasive Surgeries (MIS) for various disease diagnoses and treatments which result in reduced trauma, faster patient recovery and less blood loss. These procedures require insertion of needles and catheters inside the body for tissue biopsy, neurosurgery, electrolytic ablation and so forth. Cardiac catheters are applied for ablation, pacing and blocking ruptured blood vessels [1,2]. Currently, catheter path planning is usually performed manually based on pre-operative MRI, ultrasound, fluoroscopy X-ray images by a surgeon. Therefore, there is a tendency toward pre-operative path planning methods which can help the surgeon to conduct an optimal navigation of the catheter. To the authors' knowledge, there is very limited literature dealing with path planning of probes and catheters due to the complex constraints of the environment and probes. In [3] motion planning problem is formulated as a dynamic system in which the initial and final configurations represent the boundary values and conditions; therefore, the planning problem is transformed into solving a list of constraints, while minimizing cost functions (total potential energy of the deformable robot). The planner checks for possible collisions between the robot and the obstacles during each simulation step. An algorithm is applied to detect collisions between the deformable model and stationary environment. A potentially colliding set of overlapping primitives using set based Computations is computed. The algorithm uses 2.5D overlap tests between arbitrary objects and checks for the existence of a separating surface along a view direction. The algorithm is implemented in performing path planning of catheters in liver chemoembolization. This method is computationally too expensive and takes hours for simulation. For path planning of electrode arrays in cochlear implant surgery [4,5], the authors have assumed when the bent electrode array shape matches the scala tympani curve, there will be no contact between the bent electrode and the external wall of the scala tympani. Therefore after segmenting the image and simplifying the model by exploiting an optimization algorithm the path is extracted. The authors in [6] have applied Fast Marching Methods (FMM) for nano capsule navigation. Fast Marching's curvature bound is too conservative to be adopted in real applications [7]. In contrast to the aforementioned methods, Rapidly-exploring Random Tree (RRT) can satisfy geometric and nonholonomic constraints while computing the path quickly [6].

This paper proposes an image based path planning algorithm for steerable catheters. Section II discusses steerable catheter path planning method. In section III, workspace is determined. In section IV, simulation results are provided.

2. Steerable Catheter Path Planning

Robot path planning is the process of determining a collision free path connecting the initial and target configurations while avoiding the obstacles and satisfying the physical and geometric constraints. The goal is to navigate the tip of catheter to the target configuration, q_T, while avoiding collision with the arteries and staying within the curvature bound and workspace.

2.1 RRT based Path Planning

In this paper, Rapidly-exploring Random Tree is adopted for steering the catheter. The significant feature of this method in contrast to deterministic and probabilistic roadmap planners [9] is the ability of searching high-dimensional spaces quickly that have both algebraic constraints (originated from obstacles) and differential constraints (originating from nonholonomy and dynamics). The idea behind this method is to bias the searching toward the state space, and gradually pull the search towards them. The RRT-based algorithms work on the following procedure. Initially, the entry point is added as a first vertex to the tree. In the second step, the algorithm explores a free state space (i.e. the general form of configuration space, and encodes both configuration and velocity). Moreover, the fixed obstacle region, Q_o, is assumed to be avoided. The states in the Q_o can be the states outside the curvature bound or no-go areas. Each vertex and edge of the generated path will correspond to Q_{free}, the complement of Q_o. In each iteration, a random state, q_{rand}, is sampled over Q_{free}. In the next step, the nearest vertex already in the RRT, q_{near}, to the given sample configuration, q_{rand}, is adopted. This results in a motion toward q_{rand} with a distance metric that is a fixed incremental distance, ε. If the new state, q_{new}, which is along the segment connecting q_{near} with q_{rand}, is in the free space, it will be added as a vertex to the tree. An edge is also added from q_{near} to q_{new}. This loop will be repeated until it reaches the target point. The resulting RRT construction algorithm is depicted in Fig. 1.

```
BUILD-RRT (q_init, K)
    τ. init (q_init)
    for k = 1 to K do
    q_rand ←RANDOM_CONFIG()
    Connect (τ, q_rand)
    Return τ
```

```
Connect (τ, q)
    q_near ←NEAREST_NEIGHB (τ, q)
    if NEW_CONFIG (q, q_near, q_new)
    τ. add_vertex (q_new)
    τ. add_edge (q_new)
    if q_new = q then
    Return Reached;
    else
    Return Advanced;
    Return Trapped;
```

Fig. 1: Basic RRT construction algorithm

3. Workspace Determination

For robotic catheter navigation, an accurate path planning method is required. Toward applying the method, the workspace should be determined. Once the workspace is formed, the developed path planning algorithm is tested on it. The aortogram in lateral projection is provided as the workspace, which is a grey scale image of size 460X614 (as depicted in Fig. 2(a)). The image is segmented in order to provide the no-go areas (obstacles) that are wall of the arteries [10]. Canny filter is adopted for detecting the edges and for noise reduction Gaussian filter along with thresholding is applied. Fig. 2(b) depicts the segmented image.

(a)

(b)

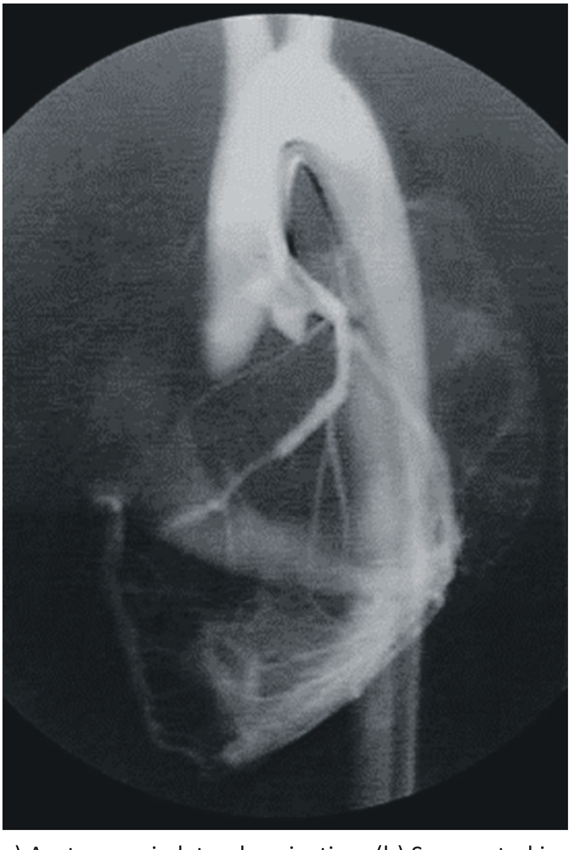

Fig. 2: (a) Aortogram in lateral projection, (b) Segmented image

4. Simulation Results

Once the configuration space on the aortogram is formed, the developed RRT path planning algorithm is tested on it. Fig. 3 shows the result of proposed path planner being applied to a grey scale aortogram in lateral projection. For this algorithm, the inputs are the start and target positions. Minimum curvature radius is selected to be 35mm. The result verifies the good performance of the algorithm in highly constrained and complex environment.

The algorithm has been implemented using MATLAB 7.11.0 (2010b), ran on Intel® core™ 2 Duo CPU T5500 (1.66 GHz) processor.

5. Conclusion

This paper proposes an image based automatic path planner for cardiac catheterization. Since the superior performance of RRT path planning method has been proved [8], this method is adopted for path planning of the catheter. Automatic steering of catheter is based on medical imaging; therefore, for configuration space determination, image segmenting seemed to be necessary. Edge detection, noise reduction and thresholding were performed over the image. Future work will focus on path planning based on 3D CT/MRI images, additionally complete catheter ablation path planning from femoral vein to cardiac ventricle/atrial will be performed, and it will be verified experimentally. In order to be able to extend the algorithm in three dimensional space, C++ can be useful in increasing is efficiency. Testing different entry points for catheter insertion and accordingly different path planning algorithms will allow the surgeon to consider all possible situations more precisely.

Fig. 3: Result obtained using RRT based path planner

References

[1] Kesner, S. B., Howe, R. D., 2012, Motion compensated catheter ablation of the beating heart using image guidance and force control, In Proc. of ISER June, pp. 1-12.

[2] Yu, X., 2009, The research and realization of brain surgery path planning system, The Ninth International Conf. on Electronic Measurement & Instruments ICEMI.

[3] Gayle, R., Segars, P., Lin, M.C. and Manocha, D., 2005, Path planning for

deformable robots in complex environments, In Robotics: Science and Systems, pp.225-232.

[4] Zhang, J., Wei, W., Manolidis, S., Roland, J. T. Jr., Simaan, N., 2008, Path planning and workspace determination for robot-assisted insertion of steerable electrode arrays for cochlear implant surgery, int. conf. medical image computing and computer assisted intervention, pp. 692-700.

[5] Zhang, J., 2010, Design of steerable electrode arrays and optimal insertion path planning for robot-assisted cochlear implant surgery, Ph.D. dissertation, Univ. Columbia.

[6] Folio, D., Dahmen, C., Wortmann, T., Zeeshan, M. A., Shou, K., Pan´e, S., Nelson, B.J., Ferreira, A. and Fatikow, S., 2011, MRI magnetic signature imaging, tracking and navigation for targeted micro/nano-capsule therapeutics, In IROS, pp.1297-1303.

[7] Cabomi, C., 2011, Curvilinear path planning for a steerable flexible neuro-surgical probe, M.Sc. dissertation, Univ. Poliiecnico di Milano.

[8] Lavalle, S. M., 1998, Rapidly-exploring random trees: a new tool for path planning.

[9] Siegwart, R. and Nourbakhsh, I.R., 2004, Introduction to autonomous mobile robots, Massachusetts Institute of Technology.

[10] Gonzalez, R. C. and Woods, R. E., Digital image processing, 2008, 3rd ed., New Jersey: Pearson Prentice Hall.

A REAL TIME RT-LAB BASED DISCRETE SPACE VECTOR MODULATION SCHEME FOR INDUCTION MOTORS FED

A. Idir[1] & M. Kidouche[1]

[1]Applied Automation Laboratory, F.H.C., University of Boumerdes, 1 Av. de l'Independance, 35000 Boumerdes, Algeria , e-mail: idir_ah@ yahoo.fr

Abstract

In this paper, we present a Real Time Discrete Space Vector Modulation (DSVM) Scheme of an induction motor using RT-Lab Software and Matlab/Simulink environment. In DSVM technique, new voltage vectors are synthesized by applying three standard voltage space vectors for three equal time intervals at each sampling period. To illustrate the performances of this control scheme, real time simulation results are presented.

Key words: Induction Machine**,** Real Time Simulation, Discrete Space Vector Modulation, RT-Lab.

Introduction

Over the years, it has been increasingly acknowledged how important and essential the tools of real-time simulation and testing in all industries are. These tools are no longer a luxury in modern system design, especially in electric motor drives and power electronics, whose applications are found in an ever increasing number in all sectors [1]. The cost constraint has led design and test engineers to fully recognize the importance of real-time simulation, and it is now widely used by high-tech industries as an essential and powerful tool to prototype complex engineering systems in a cost-effective and secure manner, while reducing the time-to-market [2].

A drive system that consists of a motor controlled by a power electronics converter is a complex nonlinear system. The major research areas in electrical drives include high-level modeling of the integrated motor drive, new converter-inverter topologies, control algorithms, performance optimization, and fault tolerant controllers. Thus, performing system-level testing which is one of the major subsystems in developing a complex product in a comprehensive and cost effective way, need real-time (RT) simulations [3].

The inverters are used to convert the dc voltage into ac voltage with controlled voltage and frequency. The waveform of the output voltage depends on the switching states of the six switches. Many applications of inverters face three major requirements and limitations [4-7].

There are several techniques of switching the inverter switches such as the six step inverter, hysteresis current controller, sinusoidal pulse width modulation, and space vector pulse width modulation. Each technique has its own advantages and disadvantages. Importance of SVPWM technique leads to recent utilization of parallel three phase Inverters using SVPWM technique [8,9]. The modulation principle of DSVM is based on SVPWM, which is to acquire the wanted voltage vector through basic voltage synthesis. The difference to DSVM is the time of application need no computation, each one exert a third of a period.

This paper presents a Real time simulation of Discrete Space Vector Modulation (DSVM) Scheme of an induction motor using RT-Lab Software and Matlab/Simulink environment. In DSVM technique, new voltage vectors are synthesized by applying three standard voltage space vectors for three equal time intervals at each sampling period. To illustrate the performances of this control scheme, real time simulation results are presented.

2. Real Time Simulation Platform

Fig.1 below shows the concept of digital real-time simulation of an induction motor drive system. The drive system developed includes an induction motor. The test bench is also equipped with a semikron inverter fed by the DC voltage issued to a bridge rectifier output connected to the three-phase AC supply 400/230V-50 Hz, RT-Lab Target (16 Analog input(OP5340),16 Analog output(OP5330), 32 Digital I/O (OP5311-5312)) and a personal computer with MATLAB/Sirnulink/RT-Lab software to design a simulate induction machine control. The simulator uses the following communication link (Ethernet connection (100 Mb/s) between the hosts and target PC‟s).

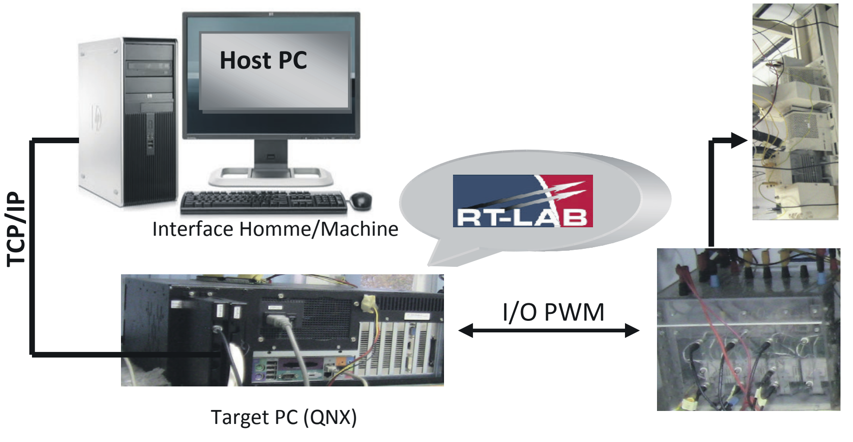

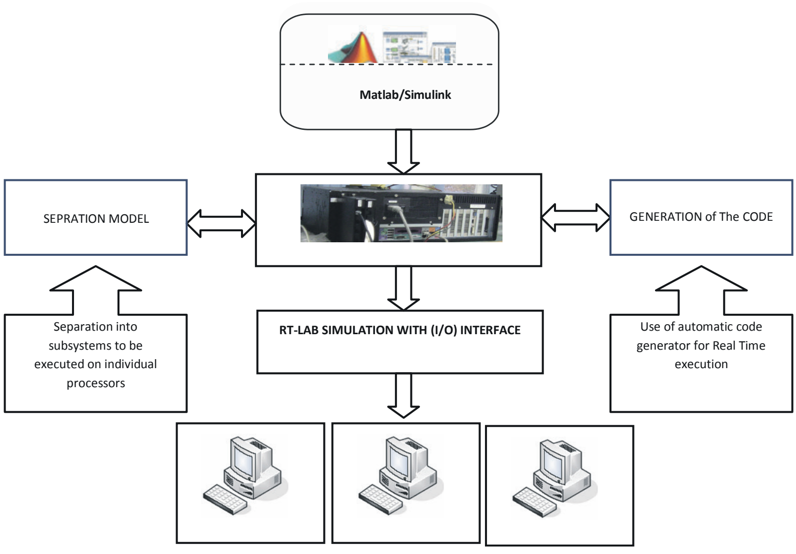

Fig. 2. Principle of Real-time Simulation using RT-Lab

4.Principle of Discrete Space Vector Modulation

The modulation principle of DSVM is based on SVPWM, which is to acquire the wanted voltage vector through basic voltage synthesis. The difference to DSVM is the time of application need no computation, each one exert a third of a period.

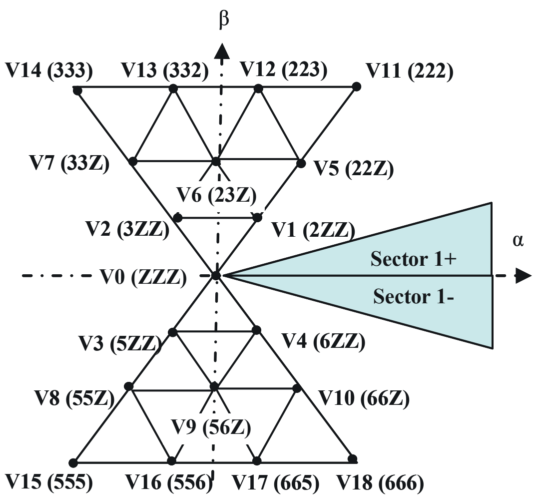

Fig. 3. The DSVM voltage vector of first sector

In DSVM, the 5 voltage vectors are permuted and combined with 3 in a group, and 19 voltage vectors are formed in this way, as illustrated in Figure 3. Each crossing point is the end of the synthesized voltage vectors. "23Z"is the vector synthesized by V2, V3 and 0 vectors. Thus there are many optional voltage vectors synthesized with DSVM method, far more than the eight basic voltage vectors in traditional method.

5. Induction Motor Model

The plant that this paper deals with is an induction motor, a highly nonlinear system. Its model described in the stator direct and quadrature frame *(d-q)* is given by equation (1).

$$\begin{cases} \frac{di_{ds}}{dt} = -\left(\frac{1}{T_s\sigma} + \frac{R_r(1-\sigma)}{L_r\sigma}\right) i_{ds} + \omega_s i_{qs} + \frac{(1-\sigma)}{L_m\sigma}\omega_r\varphi_{qr} + \frac{1}{\sigma L_s}V_{ds} \\ \frac{di_{qs}}{dt} = -\left(\frac{1}{T_s\sigma} + \frac{R_r(1-\sigma)}{L_r\sigma}\right) i_{qs} - \omega_s i_{ds} + \frac{(1-\sigma)}{L_m\sigma}\omega_r\varphi_{dr} + \left(\frac{R_r(1-\sigma)}{L_m L_r\sigma}\right)\varphi_{qr} + \frac{1}{\sigma L_s}V_{qs} \\ \frac{d\varphi_{dr}}{dt} = \frac{R_r L_m}{L_r} i_{ds} - \frac{R_r}{L_r}\varphi_{dr} + \omega_{sl}\varphi_{qr} \\ \frac{d\varphi_{qr}}{dt} = \frac{R_r L_m}{L_r} i_{qs} - \frac{R_r}{L_r}\varphi_{qr} + \omega_{sl}\varphi_{dr} \\ \frac{d\omega_r}{dt} = \frac{L_m}{L_r}\frac{P}{J}\left(i_{ds}\varphi_{qr} - i_{qs}\varphi_{dr}\right) - \frac{C_r}{J} - \frac{f}{J}\omega_r \end{cases} \tag{1}$$

In this case, the induction motor develops an electromagnetic torque expressed as follows

$$T_e = p.\frac{L_m}{L_r}(\varphi_{dr} i_{qs} - \varphi_{qr} i_{ds}) \tag{2}$$

d, q : axes corresponding to the asynchronous reference axes in Park model, L_s, L_r R_s,, R_r and L_m are: stator and rotor main inductances, resistances and mutual inductance respectively. *J* is the rotor inertia moment, *σ* dispersion factor. i_{ds}, φ_{dr} , i_{qs}, φ_{qr} are *d*-axis stator current, rotor flux and *q* -axis stator current, rotor flux, and *p* is the number of pole pairs, ω_s is the angular speed.

6.Real Time Simulation of Dsvm for an Induction Motor

Fig. 4 below give the real time model of Discrete Space vector modulation (DSVM) for an Induction Motor Drive (IM) as implemented in RT-Lab environment. RT-Lab allows to model a subsystem in MATLAB simulink environment with some own rules and perform automatic code generation and transfer of the simulink model for the FPGA implementation.

Fig. 4 shows also the subsystem modelled for the present controller. Subsystem named "*SS_Induction_Motor*" contains the simulink model of the induction motor and the inverter RT-Events model.

Subsystem named "*SM_DSVM*" contains the discrete space vector modulation generator control model,while subsystem named "*SC_data_acquisition*" represent the model for user interface for online data acquisition.

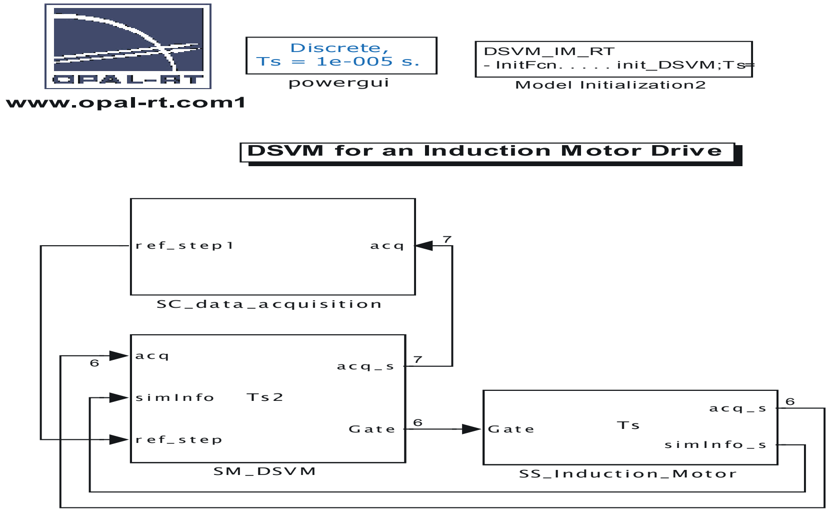

Fig. 4. RT-Lab real time simulation graphic model of DSVM of an IM

Fig. 5, Fig. 6 and Fig. 7 below give the details of master, slave#1 and slave#2 block diagrams respectively as implemented in RT-Lab environment.

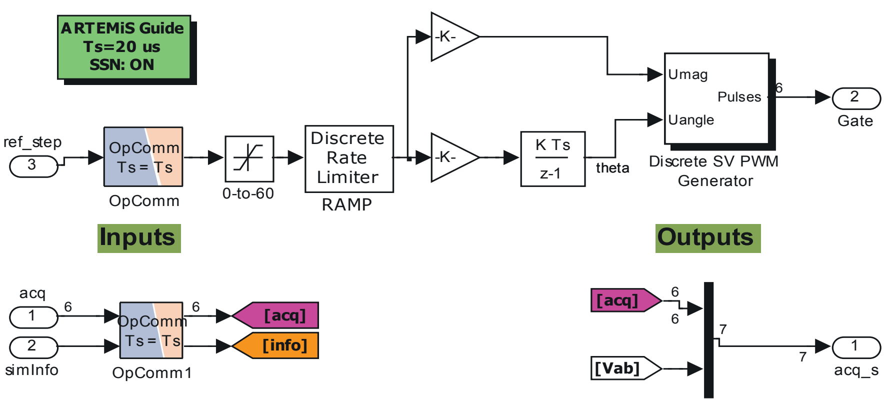

Fig. 5. Details of Subsystem Master block: SM_DSVM

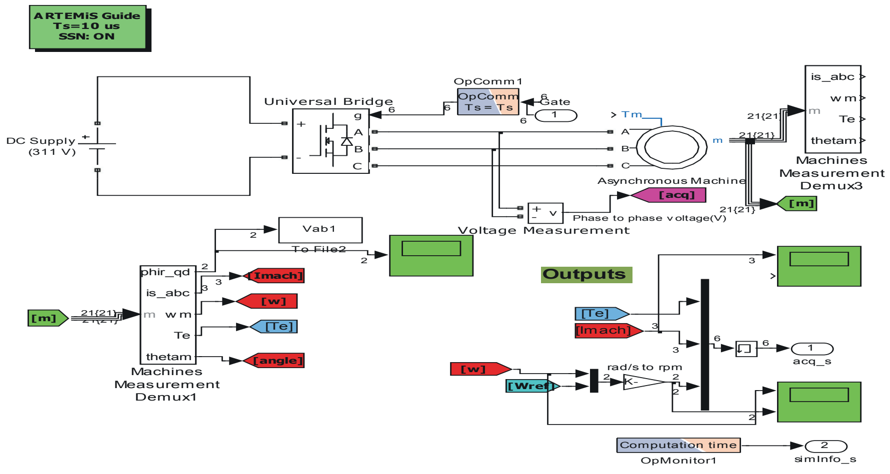

Fig. 6. Details of Slave Subsystem block: SS_Induction_Motor

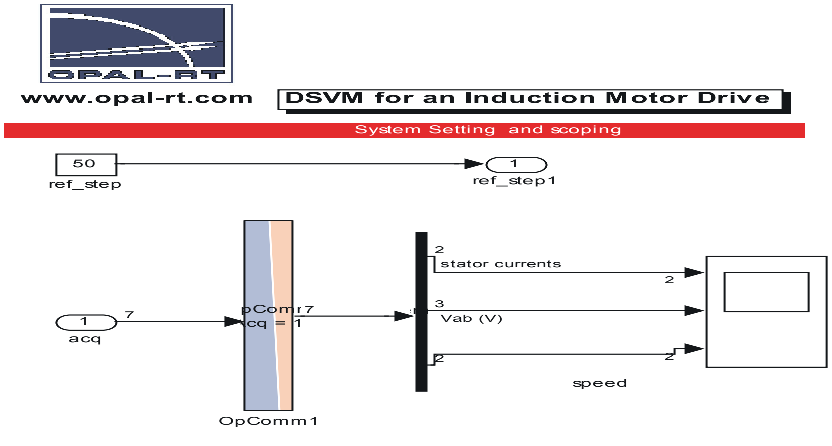

Fig. 7. Details of slave block: SC_data_acquisition

7. Real Time Simulation Results

The control algorithm has been implemented using RT-Lab software package. Satisfactory results are obtained with a fixed time step of 1.

Fig. 8, and Fig. 9 respectively, show the real time simulation of phase to phase voltage and flux.

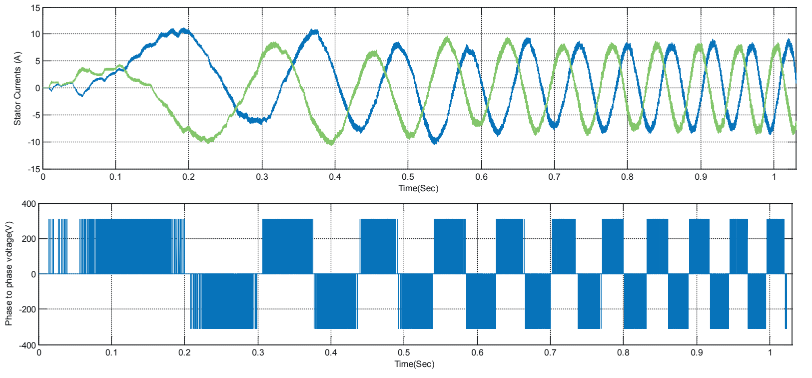

Fig. 8. Real time simulation: a) Stator currents b)Phase voltage waveforms

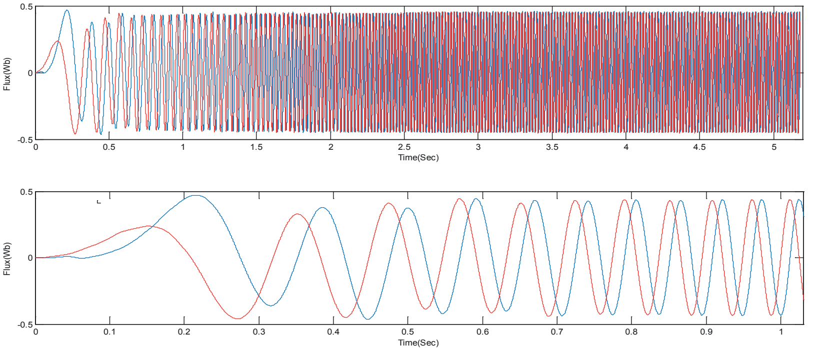

Fig. 9. Real time simulation of Flux

Fig. 10 shows the real time simulation of stator currents

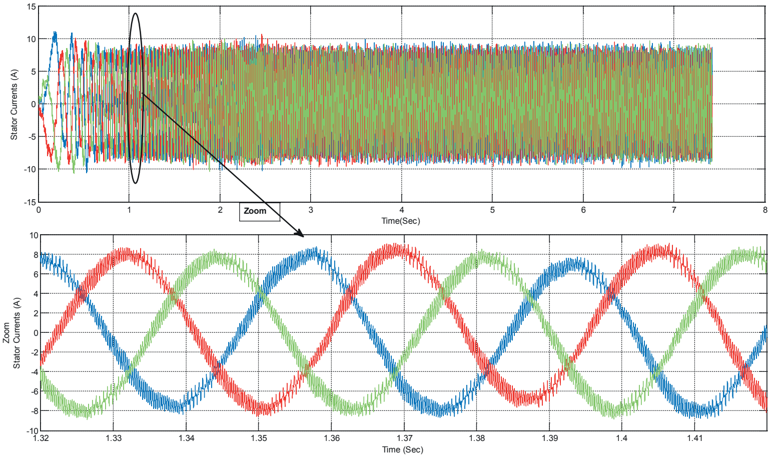

Fig. 10. Real time simulation of current measurements: i_{sa}, i_{sb}, i_{sc}

The curves of currents show the good response of currents

In this paper, we present a Real Time Discrete Space Vector Modulation (DSVM) Scheme of an induction motor using RT-Lab Software and Matlab/Simulink environment. In DSVM technique, new voltage vectors are synthesized by applying three standard voltage space vectors for three equal time intervals at each sampling period. To illustrate the performances of this control scheme, real time simulation results are presented.

8. Conclusion

The paper presented the real time simulation of DSVM of an induction motor using RT-Lab Software and Matlab/Simulink environment. Real time simulations are required by hardware in the loop applications and their use allows rapid prototyping of high performance induction machine. The Use of RT-Lab is much time saving in developing a control model for the practical electric motor drives and offer great easy and flexibility.

References

S. Abourida, J. Belanger, real-*time platform for the control prototyping and simulation of power electronics and motor drives*, Proceedings of the Third International Conference on Modeling, Simulation and Applied Optimization Sharjah,U.A.E January 20-22 2009.

M. Ouhrouche, R. Beguenane , A.M. Trzynadlowski, J.S. Thongam and M. Dube-Dallaire, *a pc-cluster based fully digital real-time simulation of a field oriented speed controller for an induction motor*, International Journal of Modelling and Simulation. Paper number 205-4346 (revised)

A. Osama Mohammed and Y. Abed Nagy , *Real-timesimulation of electric machine drives with hardware-in-the-loo*p, COMPEL: The International Journal for Computation and Mathematics in Electrical and Electronic Engineering, Vol. 27 Iss: 4 2008,pp. 929 - 938

Bose, B. K., *Modern Power Electronics and AC Drives*, Prentice Hall PTR, 2002.

Rashid, M. H., *Power Electronics Handbook*, Academic Press, 2001.

Mohan, N., First Course on Power Electronics and Drives, MNPERE, 2003.

Vas, P., *Electrical Machines and Drives a Space-Vector Theory Approach*, Oxford University Press, 1992.

H. R. Pouya and H. Mokhtari, *Control of Parallel Three-phase Inverters Using Optimal Control and SVPWM Technique*, Proc. of IEEE International Conference on Industrial Electronics ISIE, Seoul, Korea, July 2009.

E. Hendawi, F. Khater and A. Shaltout, *Analysis, Simulation and Implementation of Space Vector Pulse Width Modulation Inverter*, Proceedings of the 9th WSEAS International Conference on applications of electrical engineering.

M. Harakawa, H. Yamasaki, T. Nagano, S. Abourida, C. Dufour, J.Belanger, *Real-Time Simulation of a Complete PMSM Drive at 10 µsTime Step*, Presented at the International Power Electronics Conference, 2005 (IPEC 2005), Niigata, Japan, 2005

D. Zaldivar, E. Cuevas, M.A. Pérez-Cisneros, J. H. Sossa, J. G. Rodríguez, E. O. Palafox, *An educational fuzzy-based control platform using LEGO robots*, International Journal of Electrical Engineering Education, Volume 50, Number 2 / April 2013

J. Makwana, A. Mishra, P. agarwal and S.P Srivastava, *Implementation of low cost* *switched reluctance motor drive using RT-Lab*, International Journal of Engineering Science & Advanced Technology, Volume-2, Issue-4, 772 – 780 (2012)

M. Ouhrouche, N. Léchevin and S. Abourida, *RT-Lab Based Real-Time Simulation of a Direct Field-Oriented Controller for an Induction Motor*, Proceedings of the 7th International Conference on Modeling and Simulation of Electric Machines, Converters and Systems, Montreal, Canada, Aug18-21, 2002.

[S. Beaulieu, M. Ouhrouche, C. Dufour and P.F. Allaire: *Real-time Modeling and Simulation of an Active Power Filter* Proceedings of Ninth IASTED International Conference on Power and Energy Systems – PES'2007, Clearwater, Florida, USA, January 3-5, 2007.

M. Ouhrouche, R. Beguenane and M. Dube-Dallaire, *Real-time Simulations: A New Powerful Tool for Rapid Prototyping of High Performance Induction Machine Controllers*, Proceeding of the IASTED International Conference on Applied Modeling and Simulation, Rhodes, Greece, June 28-30, 2004.

Bo Fan, Guanghui Shi , Yixin Yin , Cunfa Fu , Juwei Zhang , *Study on Torque Ripple Reduction of Direct Torque Control System Based on DSVM*, 2011 International Conference on Electronic & Mechanical Engineering and Information Technology

S. Abourida, *Real-Time PC-Based Simulator of Electric Systems and drives*, Proceedings of APEC'2002.

C. Dufour, S. Abourida and J. Belanger, "Real-Time Simulation of Induction Motor IGBT Drive on a PC-Cluster, Proceedings of the International Conference on Power Systems Transients (ICPST'03), Hong Kong, 2003

I. Boldea, *Control issues in adjustable speed drives,* IEEE Industrial Electronics Magazine, Vol. 2, No. 3, Sept. 2008, pp. 32 - 50.

L. Meng, S. Yang, L. Wang, V. Liu and F. Peng , *Hardware-In-Loop Test for Automatic Voltage Regulator based on dentification Mode,* 15th International Power Electronics and Motion Control Conference, ECCE Europe, Novi Sad, Serbia, EPE-PEMC 2012

Domenico Casadei, Giovanni Serra, Angelo Tani. Implementation of A Direct Torque Control Algorithm for Induction Motors Based on Discrete Space Vector Modulation [J]. IEEE Transactions on Power Electronics, 2000, 15(4): 769 - 777.

D. Veera 3 and Dr. T. Brahmananda Reddy,Implementation of Discrete Space Vector Modulation Based Direct Torque Control of Induction Motor for Reduced Ripple: A Sliding Mode Control Approach, International journal of advanced scientific and technical research Issue 2 volume 4, August 2012

MP3 FILE IDENTIFICATION BASED ON CONCURRENCE ORDER OF METADATA

Youngseok Lee, Jongweon Kim*

Department of Electronics, Chungwoon University

Depaprtment of Copyright Protection, Sangmyung University*

113, Sukgol-ro, Nam-gu, Incheon, Korea

20, Hongjimun-2gil, Jongno-gu, Seoul, Korea*

Abstract

In this paper we investigated applicability of metadata to identify music contents in MP3 file. Metadata in MP3 include information associated with music contents such as a table of Hoffman code, scale factors, stereo types.

We considered music contents in MP3 file as a function of metadata. Our idea is reasonable since music contents in MP3 file are controlled by characteristics of in metadata.

In order to identifying a MP3 file, we used a concurrence order of metadata. We assumed that MP3 files with other music contents have other concurrence orders in their metadata. In experiments, we extracted metadata from MP3 files and rearranged metadata as column vector of matrix. The rearranged metadata were analyzed various numerical analyses such as singular value decomposition, tensor analysis and differential method.

I. Introduction

Music identification is the most typical application of audio searching technique. Bu comparing the characteristics of an unknown music query fragment. Usually transmitted from mobile phones on the wireless telecommunication network or from personal computers on the Internet, with those previous calculated and stored in characteristics database, matching results and related metadata are returned. Metadata in music file must represent music contents to differentiate from each other.

Currently, many researches have insisted on various methods for identifying music contents. Perhaps the most common method used is to identify the type or name of a file by the fingerprints in music contents (Heydari 2002). This is an extremely unreliable method, as any user or application can change or delete fingerprints any time. As a result, some users are able to conceal files from system administrators simply by renaming them to a filename with a different extension. While this doesn't conceal the existence of a file, it can conceal the nature of a file and can prevent it from being opened by the operating system

Especially MP3 files take up most of music file in world music markets which are regardless of its legal or illegal. According to the recent report in [ ], about 90% of the music contents is traded by an MP3 file type in music market whether it is online or off line. Therefore the identification of MP3 file plays important role of a music searching, a storage indexing and a tracking of illegal distributions (Wei Li, Yaduo Liu 2010)

In this paper we investigated applicability of metadata to identify music contents in MP3 file. Metadata in MP3 include information associated with music contents such as a table of Hoffman code, scale factors, stereo types. We considered music contents in MP3 file as a function of metadata. Our idea is reasonable since music contents in MP3 file are controlled by characteristics of in metadata.

The remained paper is organized as follows. Section 2 introduces the basic principles of MPEG Layer-3, bit stream data format and metadata structure. Section 3 details the steps of our experiment to identify MP3 file. Experimental results on occurrence order of metadata in a MP3 file are given in Section 4. Section 5 concludes this paper and point out possible ways of future research.

II. MP3 File Structure

A simplified illustration of MPEG Layer-3 encoder is shown in Figure 1.

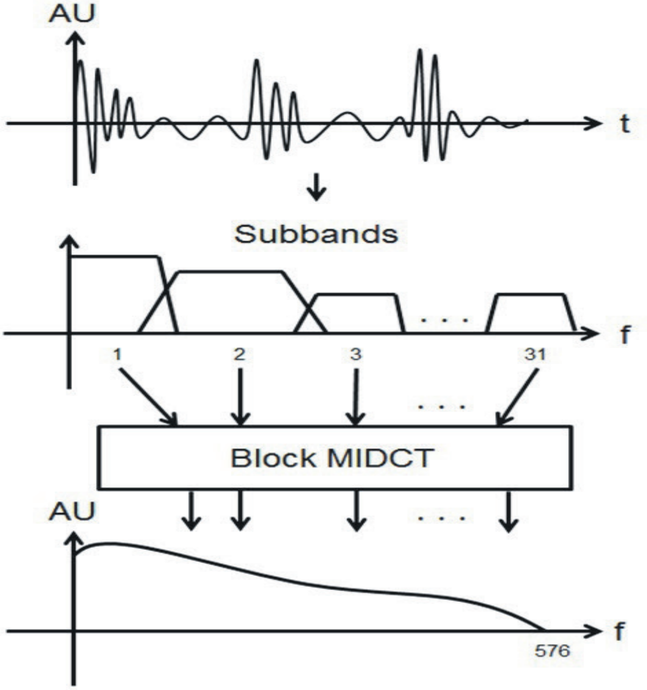

Figure 1. Simplified frequency transformation of MPEG Layer-3 encoder

The input PCM signal is mapped into 32 equal bandwidth subbands through a polyphase filter bank, which simulate the critical bands in the human auditory system (HAS). The sub-band outputs are further subdivided by MDCT transform using long or short window to provide better spectral resolution. The long window allows greater frequency resolution for audio signals with stationary characteristics, while the short window provides better time resolution for transients.

Combined with other adjuvant techniques including psychoacoustic model, scale factor, *Huffman* coding, quantization etc, the final compressed bit stream is generated. Figure 1 displays the frame format of MP3 bit stream, and each frame has two granules to exploit further redundancies.

II.1 OVERALL STRUCTURE OF MP3 FILE FORMAT

Within an MPEG audio file, there is no main header, as an MPEG audio file is just built up from a succession of smaller parts called frames. Each frame is a data block with its own header and audio information as in Figure 2.

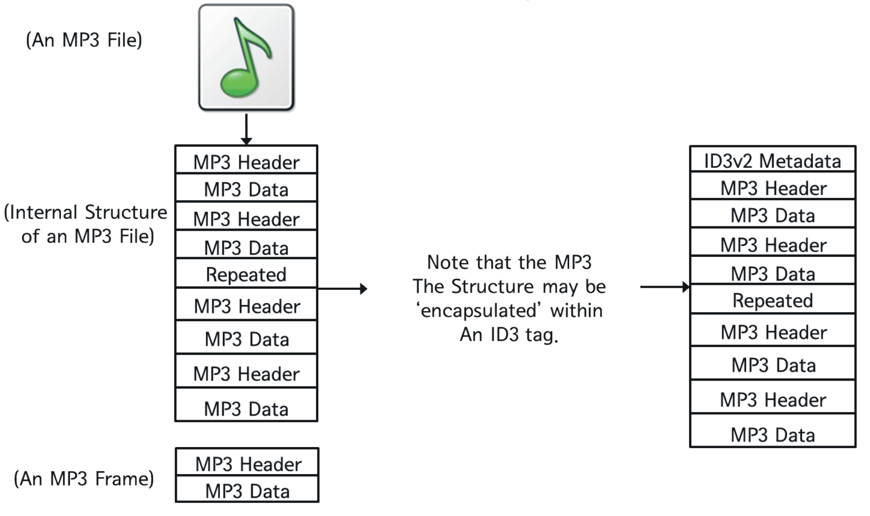

Figure 1. Simple structure of MPEG audio Layer-3 file

In the case of Layer I or Layer II, frames are totally independent from each other, so ONE can cut any part of an MPEG audio file and play it correctly. The player will then play the music starting from the first full valid frame it will find. However, in the case of Layer III, frames are not always independent. Due to the possible use of the *'byte reservoir'*, which is a kind of internal buffer, frames are often dependent of each other. In the worst case, 9 input frames may be needed before being able to decode one single frame. If one needs to retrieve information about an MPEG audio file, you might simply locate the first frame, and retrieve information from its header. Information within other frames should be consistent with the first one, except for the bitrate, as you might be retrieving information from a variable bitrate (VBR) file.

In a VBR file, the bitrate can be changed in each frame. It can be used, as an example, to keep a constant sound quality during the whole file, by using more bits when the music is more complex and thus requires more bits to be encoded with a similar quality. The frame header including metadata itself is 32 bits (4 bytes) length. The first twelve bits (or first eleven bits in the case of the MPEG 2.5 extension) of a frame header are always set to 1 and are called 'frame sync'. Frames may also feature an optional CRC checksum. It is 16 bits long and, if it exists, immediately follows the frame header. After the CRC comes the audio data. By re-calculating the CRC and comparing its value to the sored one, you can check if the frame has been altered during transmission of the bit stream.

II. 2 Structure of Metadata In *Sideinfo* of MP3 File

The side information part of the frame consists of information needed to encode the main data. The size depends on the encoded channel mode. If it is a single channel bit stream the size will be 17 bytes, if not, 32 bytes are allocated. The different parts of the side information are presented in Table 1 and described in detail below.

Table 1. Metadata in *sideinfo* of MPEG audio Layer-3 file

Bit allocation	Single Channel	Dual Channel
Main_data_begin	9	9
Private_bits	5	3
Share	4	4+4
Information for granule		
Part2_3_length	12	12+12
Big_values	9	9+9
Global_gain	8	8+8
Scalefac_compress	4	4+4
Window_switching	1	1+1
For normal blocks		
Table_select	3*5	3*5+3*5
Region0_count	4	4+4
Region1_count	3	3+3
Preflag	1	2
Scalefac_scale	1	2
Count1_table_select	1	2
Subtotal for first granule	59	118
Subtotal for second granule	59	118
Total number of bits	136	256
Total number of byte	17	32

The length of each field will be specified in parenthesis together with the fieldname above the actual description. If one length value is written the field size is constant. If two values are specified the first value will be used in mono mode and the second will be used for all other modes, thus these fields are of variable length. All tables below will assume a mono mode. The tables will change depending on mode since separate values are needed for each channel.

Using the layer III format there is a technique called the bit reservoir which enables the left over free space in the main data area of a frame to be used by consecutive frames. To be able to find where the main data of a certain frame begins the decoder has to read the *main_data_begin value*. The value is as a negative offset from the first byte of the synchronization word. Since it is 9 bits long it can point $(2^9-1) \times 8=4088$bits. This means that data for one frame can be found several previous frames. Note that static parts of a frame like the header, which is always

32 bytes, are not included in the offset.

III. Proposed Method

The overall structure of proposed method is shown following as Figure 3.

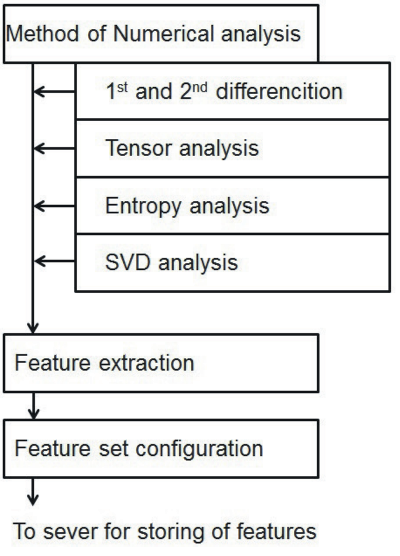

Figure 3. Overall structure of proposed method

In Figure 3, we extracted the metadata from *sideinfo* blocks in MP3 file and then rearranged the metadata on matrix from at first. The rearranged metadata were analyzed some numerical analyses such as differential method, singular value decomposition (SVD), tensor analysis and entropy analysis as in Figure 4.

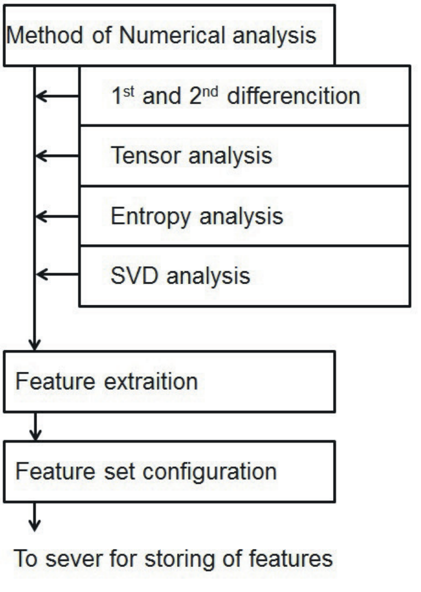

Figure 4. Representation details of numerical analysis stage in Figure 3

In the numerical analysis stage, the differential method represents metadata to differentiated matrix and analyzes its characteristics such as the sign of slope, local maxima and local minima.

SVD analyzes singular values of metadata matrix. SVD is a factorization of a real or complex matrix, with many useful applications in signal processing and statistics (VASIL KOLEV 2010). Formally, the singular value decomposition of an *m×n* real or complex matrix *M* is a factorization of the form

$$M = U\Sigma V^* \quad (1)$$

Where *U* is a *m×m* real or complex unitary matrix, Σ is an *m×n* rectangular diagonal matrix with nonnegative real numbers on the diagonal, and *V** (the conjugate transpose of *V*, or simply the transpose of '*V*' if '*V*' is real) is an *n×n* real or complex unitary matrix. The diagonal entries $\Sigma_{i,I}$ of Σ are known as the singular values of *M*. The *m* columns of *U* and the *n* columns of *V* are called the left-singular vectors and right-singular vectors of *M*, respectively.

A tensor can be represented as a multi-dimensional array of numerical values (P. Comon 2009). The *order* (also *degree* or *rank*) of a tensor is the dimensionality of the array needed to represent it, or equivalently, the number of indices needed to label a component of that array. For example, a linear map can be represented by a matrix, a 2-dimensional array, and therefore is a 2nd-order tensor. A vector can be represented as a 1-dimensional array and is a 1st-order tensor. Scalars are single numbers and are thus 0th-order tensors. Tensors are used to represent correspondences between sets of geometric vectors. For example, the metric tensor **T** takes a vector **v** as input and produces the metric $\mathbf{T}^{(v)}$ on the surface normal to this vector for output thus expressing a relationship between these two vectors.

IV. Exprtimental Results

We conducted the experiment in accordance to the procedure of Figure 3. Firstly, the metadata were rearranged to a matrix form. Figure 5 shows the example of a rearranged metadata on a matrix form. The elements of metadata matrix are binary number, which are shown the bit '1' to white and bit '0' to black in Figure 5.

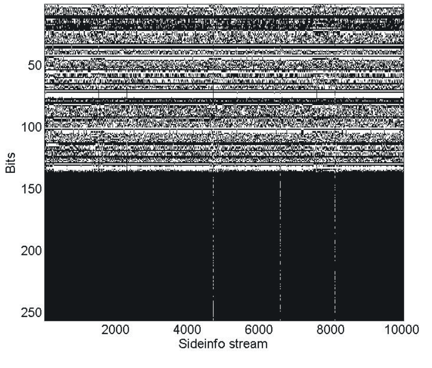

Figure 5. Example of a rearranged metadata on a matrix form

The number of column in metadata matrix is 256 and 136 in cases that the MP3 file is the stereo and mono type, respectively. The number of row depends on the number of metadata in the MP3 file. In MP3 files which used for extracting the metadata, the most metadata had mono type with the exception of some parts. Therefore the below of 156th bit in metadata matrix were bit '0' which were black color in Figure 5.

In SVD analysis of the metadata matrix, the metadata matrix was decomposed as in (1). All of 236 MP3 files were used to SVD analysis had full rank having 256 singular values. Figure 6 shows the curves of singular values by different MP3 files. In the figure, the horizontal axis is the index of metadata and the vertical axis is the logarithm scaled singular values. One can observe that the curves of logarithm-scaled singular values are clearly distinguishable.

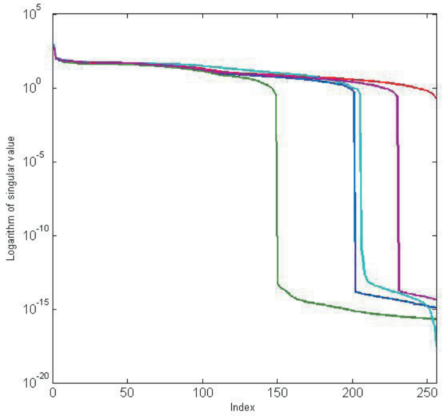

Figure 6. Curves of singular values of rearranged metadata by different MP3 files

This result means that the logarithm- scaled singular values may be possibly used for the identification of MP3 file. Another result of SVD analysis was related with some singular values Arranged in order of values. Value-ordered singular values that are dominant components in SVD, are different from each other MP3 file.

We tried to construct the metadata matrix to multidimensional array called tensor. Our intention was to identifying the particular MP3 file through the tensor analysis. The metadata tensor which constitutes to the integration of metadata matrix of mp3 files, is illustrated conceptually in Figure 7.

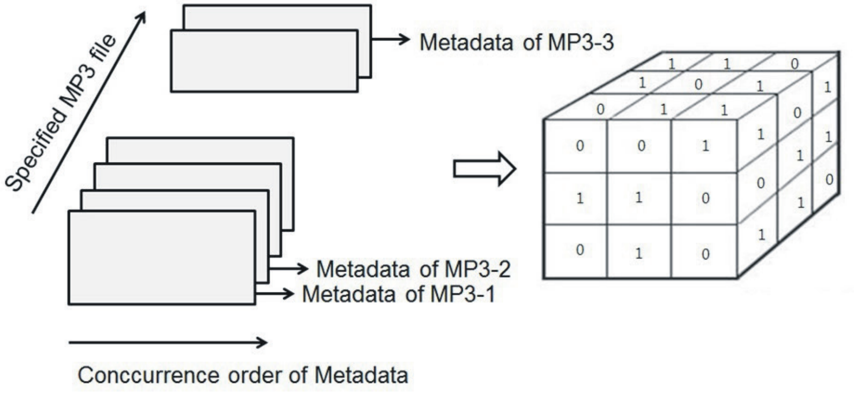

Figure 7. Multidimensional array structure of a rearranged metadata

V. Conclusions and Further Studies

Our experiments are in progress. The experimental results in this paper a part of identifying MP3 file based on the metadata. Through our experiment, we confirmed possible the identification of MP3 file. The further research focuses on the rest tensor analysis and entropy analysis of metadata to identify MP3 file.

Acknowledgement

This research project was supported by Ministry of Culture, Sports and Tourism (MCST) and from Korea Copyright Commission in 2013.

References

Heydari, M.M. and M.H., 2002. Content Based File Type Detection Algorithms. In *Proceedings of the 36th Hawawii International Conference on System Sciences*. Hawaii, USA: IEEE Computer Society, p. 10.

P. Comon, X.L. and A.L.F. de A., 2009. Tensor Decompositions, Alternating Least Squares and other Tales. *Journal of Chemometrics*, 23, p.31.

VASIL KOLEV, K.T. and M.T., 2010. SINGULAR VALUE DECOMPOSITION OF IMAGES FROM SCANNED PHOTOGRAPHIC PLATES. In Ž. M. M. K. Tsvetkov, M. S. Dimitrijević, K. Tsvetkova, O. Kounchev, ed. *Proceedings of the VII Bulgarian-Serbian Astronomical Conference*. Chepelare, Bulgaria: Astron. Soc., p. 27.

Wei Li, Yaduo Liu, X.X., 2010. Robust Audio Identification for MP3 Popular Music. In *SIGIR'10*. Geneva, Switzerland: ACM, p. 8.

AIRS CLASSIFIERS IN HANDWRITING RECOGNITION

Hamid Seridi[1], Hocine Merabti [1], Med Nadjib Kouahla [1]

[1]LabSTIC, 8 mai 1945 University, Guelma, Algeria

{seridihamid, kouahla.nadjib }@yahoo.fr

mrabti.dr@gmail.com

Abstract

This article presents a new variant of artificial immune recognition system (AIRS) devoted to solve problems of multi-classes writing recognition and to improve the recognition rate. This approach is mainly based on selecting appropriate methods of feature extraction statistical and structural, and an adequate similarity distance. To evaluate the performances of the proposed scheme, tests are performed on recognition of digits and letters.

Keywords: Artificial Immune System (AIS); handwritten recognition; Artificial Immune Recognition System (AIRS).

Introduction

Biology provides many sources of inspiration in the field of artificial intelligence and pattern recognition [1]. Inspired by the properties of immune systems [2-3], such as memory and adaptation, we propose different models to detect and recognize complex shapes like digits and handwriting.

In our case, we are interested in the use of artificial immune system (AIS) for handwritten character recognition. To overcome difficulty of the handwritten character recognition [4] which is due to the change in writing styles from one hand to another, we use different metric distances to measure similarity between features to determine best classifier.

The rest of this paper is organized as follows. Section 2, presents briefly natural immune system (NIS), followed by artificial immune recognition system (AIRS). Section 3 is devoted to the experimentation and discussion of the results obtained by this approach. Finally, last section presents our conclusion.

Natural Immune System (NIS)

The immune system is responsible for the human body's defense against the foreign pathogens [5]. Human body's defense is provided by an army of cells and molecules working together to eliminate the antigen [6], and it is also able to adapt to changing antigens, to recognize them and to remember [7].

Artificial Immune Recognition System (AIRS)

AIRS is a supervised learning algorithm inspired from immune system metaphors. The training phase is composed of four essential successive stages. These last are initialization, memory cell identification and ARB generation, resources allocation and competition, introduction of candidate memory cell [7].

Initialization

This step consists of preparing the data, seeding of initial memory cells and initial ARBs (Artificial Recognition Ball) population. During initialization, all the training data (antigens) are normalized. In our case, four distances are used [8, 9]:

Euclidean Distance[1]

$$d(x,y) = \sqrt{\sum_{i=1}^{n}(x_i - y_i)^2} \tag{1}$$

Canberra Distance[2]

$$d(x,y) = \sum_{i=1}^{n} \frac{|x_i - y_i|}{|x_i + y_i|} \tag{2}$$

Squared Chords Distance

$$d(x,y) = \sum_{i=1}^{n} \left(\sqrt{x_i} - \sqrt{y_i}\right)^2 \tag{3}$$

Chi- square Distance[3]

$$d(x,y) = \sqrt{\sum_{i=1}^{n} \frac{(x_i - y_i)^2}{|x_i + y_i|}} \tag{4}$$

An affinity threshold is used to control the quality of the memory cells [10]. This threshold is the average affinity value of all antigens and is calculated using the following equation:

$$affinity\ threshold = \frac{\sum_{i=1}^{n}\sum_{j=i+1}^{n} affinity\ (ag_i, ag_j)}{\frac{n(n-1)}{2}} \tag{5}$$

Where n is the number of learning data (antigens), ag_i and ag_j are two antigens, and represents similarity distance between the feature vectors of these two antigens. The affinity threshold is used to control the quality of the memory cells, which are kept in the system [11]. The last treatment is to initialize all memory cells and population of ARBs (Artificial Recognition Ball). This is done by randomly selecting examples from the set of training vectors.

Memory cell identification and ARB generation

The first operation of this stage is the identification of memory cell and the generation of ARB. For each antigen, *ag*, of the testing set introduced in the system;

---

1 Euclidean distance is our perception of the principle intuitionistic ball. However, given that the ball depends on a radius and the radius depends on the distance metric used, a ball can take many strange forms.

2 It is better to „normalize“ its vectors to non-negative values before using the Canberra distance or distance of chi-square.

3 See note 2.

find memory cell,, which has the highest antigen stimulation according to the following formula:

$$mc_{match} = argmax_{mc \in MCag.c} stimulation\,(ag, mc) \tag{6}$$

With

$$stimulation\,(ag, mc) = 1 - affinity\,(ag, mc) \tag{7}$$

Once has been identified, it is used to generate news ARBs (cloning) to be placed in the population of pre-existing ARBs. Each ARB is a mutated clone of and the number of clone for this cell is calculated according to the algorithm described in [7].

Allocation of resources and competition

The aim of this step is to develop a good candidate memory cell to properly classify a given antigen, *ag*. This is done by adding more information to ARBs, their classes and resources. Then, the resources of ARBs with small stimuli and ARBs without resources are removed from the population [7].

This process of allocation of resources is repeated until average stimulation, $s_{i,}$ for each subset of the class of AB is higher than the affinity threshold:

$$s_i = \frac{\sum_{j=1}^{|AB_i|} ab_i * stim}{|AB_i|}, abj \in AB_i \tag{10}$$

At this point, the population consists only of ARBs which are the most stimulated by the given antigen, *ag*, and are finally ready for the final stage of learning.

Introduction of a candidate memory cell

After the stage of learning, a candidate memory cell is chosen among the remaining ARBs and if it is stimulated by the training antigen, *ag*, it is added to the set of memory cells [5]. Once the learning phase is complete, the classification of test examples is performed by K-means. This process continues until all the antigens were presented to the system.

Handwriting Recognition System

Database

In our study we focus on the classification of digits and letters, taken from the MNIST data-base [12], and samples of handwritten letters [13]. Figure 1 shows a set of images from the used database.

(a) (b)

Figure 1. Samples of data. (a). A sample of digits of the database (MNIST), (b). A sample of handwritten letters.

Coding Data

Some preprocessing operations are performed on the images of digits (letters) to reduce the effects of noise, followed by the extraction of feature vectors representing each digit (letter). In what follows, a description of the proposed system is given [14].

Preprocessing

Preprocessing operations prepare the image of digits (letters) for the later stages of the recognition process. Practically these preprocessing include: thresholding, smoothing, dilation, erosion, standardization, localization, and the skeletonization.

Extraction of Primitives

In our approach, we consider 31 features: 28 statistical features and 3 structural features.

Classifier

The last step is to classify the data with AIRS using the four distances, and evaluate its performance by comparing it with other conventional classifiers: K Nearest Neighbors (KNN), Multi-Layer Perceptron (MLP) and Radial Basis Function (RBF).

Experimental Results

In order to evaluate the proposed classifier for digits (letters), the database is divided into two parts. The first part is composed of an image set for learning classifiers (10000 images of digits and 60 images of the letters), while the second part consist of an image set for testing classifiers (6000 images of digits and 60 images of letters). We initialize AIRS system parameters, the corresponding values were empirically determined; those which give best recognition rate are shown in Table I. Tests carried out with the four distances: (EUC (Euclidean), CHI (Chi-square), CAN (Canberra), COR (Squared Chords)) on the all data set are presented in table II.

Table I. Parameter Selection for Airs (Handwritting Recognition)

AIRS parameters	Values
Clonal rate	30
Mutation rate	0.25
Hypermutation rate	15
Affinity threshold scalar	0.01

Table II. Performances of Proposed Classifiers With Differents Distances.

Classifiers with	Recognition rate (%)	
	Digits	*Letters*
KHI	85.85	84.56
CAN	91.05	88.87
COR	81.57	82.23
EUC	82.44	86.66

Table II shows that the classifier with CAN distance is better than the others, the results obtained with EUC, COR and KHI are not satisfactory although all the features were used. To improve the recognition rate in the cloning step, the mutation is a permutation of 5% in features vector. Table III shows that there is a significant improvement in recognition rates using permutation instead of mutation in the cloning phase.

Table III. Performances of Proposed Classifiers With Permutation.

Classifiers With	Recognition rate (%)	
	Digits	*Letters*
KHI	92.91	90.12
CAN	96.34	95.55
COR	92.11	90.78
EUC	94.67	94.53

To validate this approach, a comparison is made with other classifiers such as: traingdx standard algorithms of Multi-Layer Perceptron (MLP), newrb of Radial Basis Function (RBF) and also the classifiers K Nearest Neighbors (KNN) using a set of 12 structural and geometric characteristics [15]. Table IV shows that our approach presents good recognition rate for both case digits (96.64%) and letters (95.55%) compared to others.

Table IV. Manuscript Handwriting Recognition Using Mlp, Rbf And K-Nearest Neighbor (KNN) Classifiers.

Classifiers	Performance (%)	
	digits	***Letters***
RBF (newrb)	71.80	50
K-Nearest Neighbors (KNN)	74.74	82.48
MLP (traingdx)	80	69.63
CAN	96.34	95.55

Figure 2 and 3 show respectively the effect of varying the number of clone in the interval [40, 1000] and the number of initial antibody (ARB) in the interval [10, 800] on the rate of recognition during the learning phase. Notice that the increase of these two parameters, the rate of recognition and computation time increases at the same time. This improvement in the recognition rate is mainly due to the diversity of the population which change its characteristics according to antigens presented at its input.

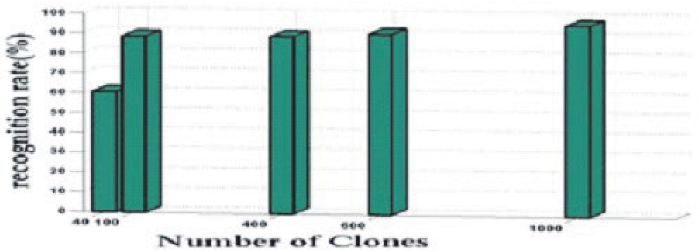

Figure 2. The variation of recognition rate according to the number of clones.

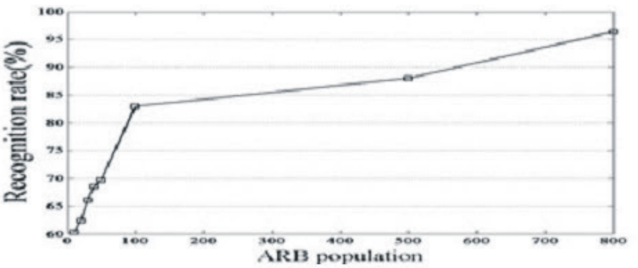

Figure 3. The variation of recognition rate according to the initialization antibodies.

Conclusion

In this paper we proposed a bio-inspired approach based on the extraction of different characteristics, choice of a similarity distance and an appropriate cloning method (mutation, permutation) to improve the performance of the classifier in terms of reducing computation time and accuracy quality. Test carried out on data set, show that proposed model has a high recognition rate compared to those provided by MLP, RBF and KNN.

References

De Castro, L.N., 2012. Fundamentals of Natural Computing. Slides of Complete Course. Book.

De Castro, L.D. and Timmis, J.I., 2002. Artificial Immune Systems: A Novel Paradigm for Pattern Recognition. Artificial Neural Networksin Pattern Recognition, L. Alonso, J. Corchado, C. Fyfe, 67-84, University of Paisley.

Lingjun, M. Peter, V. D. P, and Haiyang, W. A., 2005. Comprehensive benchmark of the artificial immune recognition system (AIRS). Proc. advanced data mining and applications ADMA, Chine, vol. 3584, pp. 575-582.

Timmis, J., August 2000. Artificial immune systems. A novel data analysis technique inspired by the immune network theory. PhD thesis, Department of Computer Science, University of Wales, Aberystwyth. Ceredigion. Wales.

Aickelin, U. and Dasgupta, D., 2010. Artificial Immune Systems. Chapters 13.To appear in (updated) edited volume on Search Methodologies: Introductory Tutorials in Optimization and Decision Support Techniques. University of Memphis, Memphis, TN 38152, USA.

Hofmeyr, S. A. and Forrest, S., 2000. Architecture for an artificial immune system. Evolutionary Computational Journal 7(1): 45-68.

Watkins, A.B., 2001. AIRS. A resource limited artificial immune classifier. Master Thesis on computer sciences, Mississippi state university, 92 pages.

Kokare, M. TENCON 2003. Comparison of similarity metrics for texture image retrieval. Conference on Convergent Technologies for the Asia-Pacific Region (Volume: 2).

Olivier LaBarre, M., July 2002. On www.uqtr.uquebec.ca/~biskri/Personnel/mol/RD.doc.

Kodaz, H. Özşenb, S. Arslana A, and Güneş, S. 2009. Medical application of information gain based artificial immune recognition system (AIRS): Diagnosis of thyroid disease. Journal of Expert systems with applications, Vol. 36, 3086-3092.

Watkins, A., 2005. Exploiting immunological metaphors in the development of serial, parallel, and distributed learning algorithms. PhD thesis at the University of Kent.

Lecun, Y. 1998. On http://yann.lecun.com/exdb/mnist/.

Dileep Gaurav, D. 2009. Feature extraction for character recognition on http://www.mathworks.com/matlabcentral/fileexchange/24624-feature-extraction-for-character-recognition.

Vamvakas, G. Gatos, B, and Perantonis, S. J., 2010. Handwritten character recognition through two-stage foreground sub-sampling. Pattern Recognition, Vol. 43, Issue 8, pp. 2807-2816.

Nebti, S. and Boukerram, A., March 2012. Handwritten characters recognition based on nature-inspired computing and neuro-evolution. Applied Intelligence, the International Journal of Artificial Intelligence, Neural Networks, and Complex Problem-Solving Technologies, ISSN 0924-669X, Vol 22, N° 2.

USING GAUSSIAN MIXTURE MODELS AND HSV COLOR SPACE FOR BACKGROUND SUBTRACTION

FAROU Brahim[1,2,a], SERIDI Hamid[2,b] and AKDAG Herman[3,c]

[1]Computer Science Department, Badji Mokhtar University, Annaba, Algeria

[2]LabSTIC, Guelma University, POB 401, 24000 Guelma, Algeria

[3]LIASD, Paris 8 University, 93526 Saint-Denis, France

[a]farou@ymail.com, [b]seridihamid@yahoo.fr, [c]Herman.akdag@ai.univ-paris8.fr

Keywords: Video surveillance, Mixture of Gaussians, Modeling the background, image processing.

Abstract. We present in this paper a system for detecting moving objects in video surveillance. We used a new approach for background substraction based on Gaussian mixtures and the HSV color space. On the one hand, the RGB space does not represent the influence of light on color because it affects all three components. On the other hand, local variations, variations in brightness as well as the complexity of the background influence on the performance of GMM. It is in this perspective that we have proposed an approach that will significantly reduce the brightness variations by focusing luminosity on a single component of the HSV space. To overcome the problem of local variation, we divide the image into equal size areas and calculate a change index for each area. Finally, only the parts that have significant change will be updated in the background model. Tests carried out on several public and personal video database showed that the proposed approach gives better performance and a low execution time than a simple GMM.

Introduction

Automatic detection and tracking of moving object is very important task for human computer interface, video communication, and security and surveillance system application. The Current surveillance systems infrastructures offer only the possibility to capture, save and distribute videos [1] to be treated manually by a specialist in the detection of anomalies and suspicious human behavior. The used methods to solve the problem of the video surveillance in its different levels [2,3], are namely, segmentation, detection, recognition and tracking of moving objects. This process begins first with the extraction of objects that do not belong in the background [4]. The method most commonly used is the modeling of the environment [5].

In the literature these approaches are divided into three parts: extraction methods of the background based on the comparison between the current image and the image of reference [6], the temporary difference that permits to cutting the video into a set of fragments separated in a lapse of constant time and the use of the optical flow estimating movements using a set of points similar to an object through several fragments [6,7]; the second step is to classify objects extracted from the first step using techniques such as contours detection and specific descriptors of an object [6,7]; the last step is the tracking of objects across the scène.

The contributions made in recent years in this area revolve around two main axes: the features used for image representation and the methods used for modeling the background. Some others works based on hybrid methods (features / characteristics, features/models and models/styles) have also contributed to the improvement of video surveillance.

[8] have used the pixels probabilities to measure the characteristics of low texture and modeling of local states with invariant scales and an adaptive learning of the background for a multi-modal representation. [9] proposed an improved modeling of the background using an approach based on the region and sparse as model characteristics of the background. An adjustment of the algorithm is performed depending on the dense regions and smooth textured scenes. Another region-based approach was proposed in [10] where two regions of motion are constructed. The first is a subtraction between the current frame and it's adjacent and the second is a subtraction between adjacent of the next frame. The difference between the regions of movement and the intersection of neighboring regions is calculated to select the candidate regions. The update is performed for regions having stable probabilities among the selected regions. [11] proposed a block modeling combining colors and textures to represent the background. [12] proposed a similar work with integrating a local binary pattern, RGB color space, Sobel filter as characteristics and the Choquet's fuzzy integral to reduce uncertainty effects. [13] used an orthogonal transformation of non-separable wavelets information frames for modeling the background with a set of post processing to eliminate shadows and noise. Another use of wavelets is proposed [14], where each region of the model-based region is represented by multi resolution wavelets with K Gaussian mixtures. For a representation and a direct adaptation of the background from a compressed video [15] have used the discrete cosine transform and AC coefficients. A non-parametric approach proposed by [16] where they applied a condensation algorithm to minimize the number of samples used for modeling the probability density of the background. The detection of moving objects is provided by Markov random fields. [17] proposed an extension of nonparametric models based on spatio-temporal modeling of the background, they used 3x3 blocks centered on the pixel in question and calculated the density of the core relative to 9 neighbors of that pixel. Other approaches have been proposed for modeling the background such as the sequential density approximation [18], the median filter on several levels with a codebook [19] and Bayesian decision [20,21] . In [20] the posterior probability of observing a pixel as background or foreground is estimated from the frequency of application of the pixel, whereas in [21] propose a Bayesian framework using spectral and spatial-temporal for modeling the background. The background is represented by the most significant characteristics for each pixel. The Bayesian classification, in both approaches, will classify each new fragment in the two classes (foreground and background) based on the main feature. Gaussian mixtures are among the most widely used methods for modeling the environment [22]. They are efficient if the video does not contain any local variation where changes in light [22]. However, learning a cluttered background and with multiple moving objects remains the major problem of this method [22,23]. The work of [24] showed that GMM offers a compromise between extraction quality and execution

time compared to other methods for extracting the background. In [25] the authors proposed a model of the background based on mixtures of Gaussian and used a real parallel to the implementation of this method on images of 1024x1280 pixels resolution at a rate greater than 30 frames per second (fps). To eliminate the problem of sudden changes in brightness, [26] proposed two different models of the background, the first when the environment is bright and the other when it is dark by using an analyzer for brightness to choose the most appropriate model for the extraction of moving objects. Another model is proposed in [27] using as features of tensor fields instead of the color space that are used in the GMM. For modeling the background [28] proposed hybridization between Gaussian mixtures and k-means approach. This model is based on the collection of intensities of each pixel, where each intensity is analyzed by a mixture of Gaussians which is then divided into two clusters by the k-means method. Another hybridization was proposed in [29] which aims to eliminate problems caused by camera motion by using fuzzy logic type 2 for treating uncertainty generated by the GMM during the modeling of the background. The combination of background models and adaptive Gaussian mixtures is proposed in [30]. The first model detects changes in the fine textures in the background using a motion detection algorithm, while the second models the background using a selective algorithm for estimating the movement hierarchy. Work as those proposed in [31,32] apply an alpha rate adaptive learning GMM allowing to solve the problem of coefficient updating GMM which greatly influences the performance of the method.

In this paper, we will focus on the detection of moving objects in video surveillance through a fixed camera using GMM. To overcome the problems of local variation and variation in brightness, first, proposed system allows segmentation of the original image, extracted from the video into several zones. Each zone will be assigned to one thread that will monitor the behavior of the area based on the analysis of histograms. Only segments that have undergone a change will be updated by the GMM.

Proposition

Pretreatment. This phase transforms the captured video into a set of frames where each frame is a sequence of video. Images from the video are RGB, but this representation is not adequate due to the influence of light on the description of objects [33]. For this we made a transfer to the HSV model recognized to be the closest model of human perception and ensures a better result since the brightness affects only one component [33].

Segmentation. This part of the system is operable only in the initialization phase of the system. Each frame is divided into N segments of equal size to minimize local variations. The choice of the number of segments depends on the initial size of the images, the environment, and the field of use. On segmentation imposes a decrease in performance and sub segmentation a decrease in quality which implies that the choice of the number of segments must be a compromise between performance and quality.

Treatment. This block contains the bulk of our work, it creates a very stable model of the background due to hybridization between the individual capabilities of threads lookouts and the power of mixtures of Gaussians.

We use multithread approach to accelerate the operations and to simplify actions. In fact, each thread will have the role of monitoring the behavior of the area to which he was assigned. For each zone, we create and save the histogram of the latter in his memory. Thus each new treatment, the agent can detect changes in the area by comparing the current state of the histogram with the state memorized.

First, we will create and save the histogram of each zone. Then, in each new treatment, we calculate and compare the current state of the histogram with the memorized state. If the comparison is greater than a certain threshold T, a signal will be triggered indicating the detection of a change in the area.

In the literature, there are several methods to measure the similarity (dis-similarity) between two probability distributions P and Q [34,35], the most used are the Bhattacharyya distance (Formula 1,2)

$$D_B(p,q) = -ln\big(BC(p,q)\big) \tag{1}$$

Where

$$BC(p,q) = \textstyle\sum_{x\in X} \sqrt{p(x)q(x)} \tag{2}$$

Gaussian Mixture Models. This section briefly describes a mixture of the Gaussians-based background subtraction method proposed in [36]. This method describes the probability of observing a pixel value, X_t , at time *t* as (6).

$$P(X_t) = \textstyle\sum_{i=1}^{k} w_{i,t}\, \eta\, (P_t\, , \mu_{i,t}\, , \Sigma_{i,t}) \tag{3}$$

where *K* is the number of Gaussians, which is usually set to be between 3 and 5; ,and are weight, mean and the covariance matrix of the *i*-th Gaussian in the mixture at time *t*, respectively. For computational efficiency, red, green and blue pixel values are assumed to be independent and have the same variances. To update this model, the following on-line K-means approximation is used [36,37]. Every new pixel value is checked against the *K* Gaussian distributions to determine whether this value is within 2.5 standard deviation of one of them. If none of the distributions includes this pixel value, the least probable distribution is replaced with a distribution that's mean; variance and weight are set to the current pixel value, pre-determined high variance and low weight, respectively. The weights of the *K* distributions at time *t* are updated as (4).

$$w_{k,t} = (1-\alpha)\cdot\, w_{k,t-1} +\, \alpha\, M_{k,t} \tag{4}$$

where α is a learning rate, and is 1 for the distribution which includes the current pixel value within its 2.5 standard deviation and 0 for the other distributions. After updating the weights, they are renormalized to make their summation become one. The parameters of the distribution which includes the current pixel value within its 2.5 standard deviation are updated as (5) (6).

$$\mu_{k,t} = (1 - \varphi_k) \cdot \mu_{k,t-1} + \varphi_k \cdot P_t \quad (5)$$

$$\sigma_{k,t}^2 = (1 - \varphi_k) \cdot \sigma_{k,t-1}^2 + \varphi_k \left(P_t - \mu_{k,t}\right)^T \left(P_t - \mu_{k,t}\right) \quad (6)$$

$$\varphi_t = \alpha\, \eta(P_t / \mu_k \sigma_k) \quad (7)$$

where is a learning factor for adapting distributions. The parameters of the other distributions remain the same. To decide whether is included in the background distributions, the distributions are ordered by the value of   and the first *B* distributions which satisfy (8) are chosen as the background distributions.

$$\beta = \arg\min\left(\textstyle\sum_{k=1}^{b} w_{k,t} > B\right) \quad (8)$$

where *B* is a measure of the minimum portion of the data that should be accounted for by the background. If is within 2.5 standard deviation of one of these *B* distributions, it is decided as a background pixel.

Post-processing

Post-processing can correct errors in the previous step. Indeed, the extraction of the background leaves a large number of noise and holes, which influence on segmentation algorithms and system behavior. For this we have proposed morpho mathematics operations as post processing. Expansion allows filling the holes left inside objects, while erosion removes unwanted points generated by the presence of dust or a tiny change in brightness is not detected by the agents. Figure1 shows that this is necessary for enhancing images after the extraction of the background to better detect the edges of objects and simplifying other system tasks.

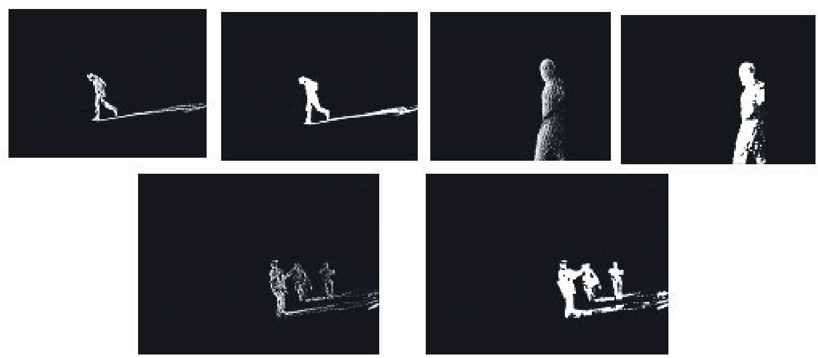

Fig.1. results of morpho-mathematics operations.

Detection of moving objects

We performed a localization of objects by analyzing histograms of horizontal and vertical projection. Using an iterative process, we try at each step to segmenting the image in parts according to the number of peaks between two minima in the histogram. We apply the same process to each part until attain a non-segmental part. Each peak between two minimums represents a moving object.

Experiments and Results

The algorithms presented in this paper are implemented in Java on a computer with an Intel Core i5 2.67 GHz power and 4GB of memory capacity.

This section seeks to highlight the results obtained from tests carried out on the basis of videos. The videos used are different from the context, the light intensity, fluctuations in the abundance of objects, number and type of people, movements caused by the active elements of nature such as wind, clouds, dust the noise and jostling movements of the camera.

a) b)

Fig.2. System results in a complex external environment. a) Shows the original image. b) Shows the image after extraction of the background.

Fig 2 was taken to a house in the mountains where there is a large movement of wind and frequent stirring of the trees and the appearance of flying objects and animals. Figure 2 shows that the system gives very good results in natural environments where the brightness and the effects of wind and dust influence on other extraction approaches.

(c) (d)

Fig.3. Results of the system in a simple and partially dark environment. c) Shows the original image. d) Shows the result of the extraction of the background.

Figure3 was taken in the hallway of a house with a very low light. This figure shows the effectiveness of our system partially dark environments with very large variations in brightness caused by the reflection of light in a narrow environment. Parts of the body not affected by the light remain undetected, but the quality of the contours allows us to retrieve the object in motion.

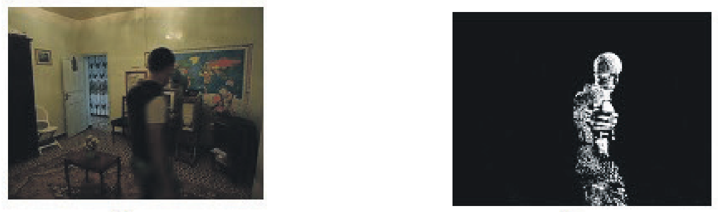

e) f)

Fig.4. System results in an administrative environment.
e) Shows the original image. f) Shows the result of the application of our approach image.

Figure4 was taken in a house with a decoration similar to office administration. It shows that the system is also efficient in administrative environments where multiple stationary objects share space with employers.

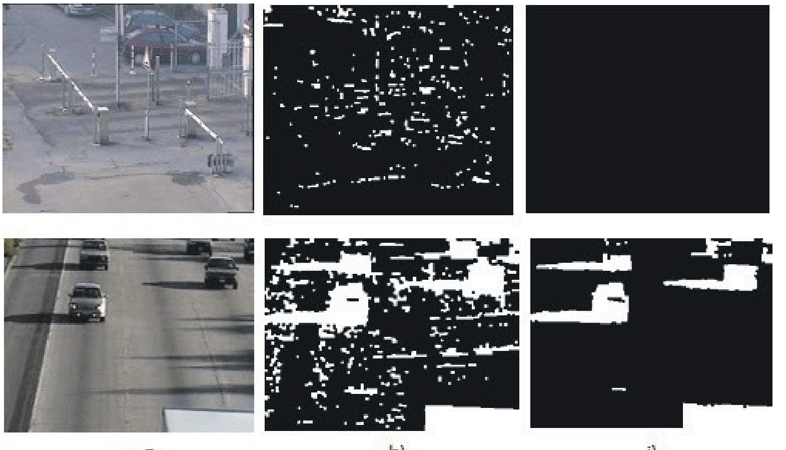

g h) i)

Fig.5. Comparison between the extraction of the background with normal GMM and our system. g) Original image. h) Results of the extraction of the background using a GMM model. i) Results of the extraction of the background with our system.

Figure5 clearly shows the contribution of our approach compared to the use of a simple GMM. Indeed, the image (Fig. 5h) shows a set of unprocessed pixels even after a post treatment step. This set comes from the fact that local variations in brightness have influenced the model where weak GMM.

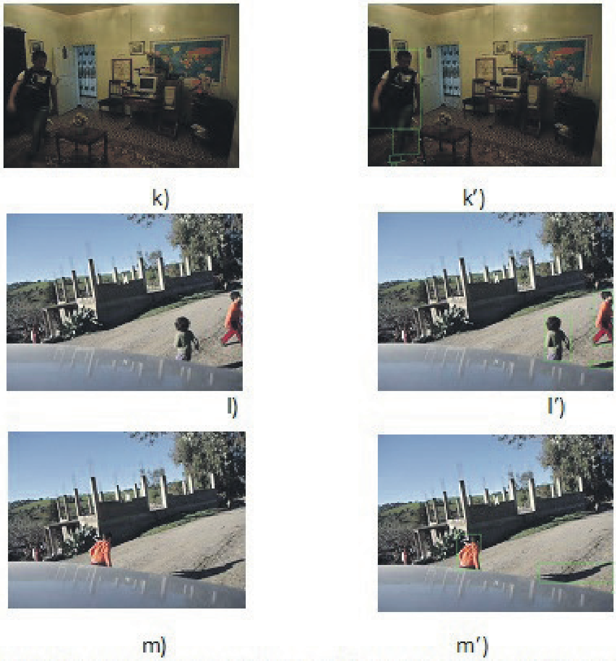

Fig.6. Result of monitoring a moving individual in a complex environment with random movements. k, l, m) the original images. k `,` l, m `) tracking objects

(Figures 6k) and (Fig. 6m) shows the tracking of a moving individual through the system. (Figures 6l) shows the tracking of several individuals. The division of the individual terminal triangle in the figure (Fig. 6k) is caused by the localization algorithm of points that constitute one segment. False detections are clearly presented in the figure (Fig. 6m) or the system detects the shadow of a person as an object in motion

Conclusion

We present in this paper a system for extracting moving objects using Gaussian mixture models preceded by segmentation into interest areas where each zone is monitored by a thread. Thread executes an algorithm for comparing histograms of areas for which they are assigned. The segmentation of image in a set of areas is due to the major default of Gaussian mixture models i.e. local variations and variations in brightness. We can say that our system has obtained encouraging results as compared to a pure modeling with GMM, but there is still some way to go to get a perfect system similar to a human being. As perspective, we will try to eliminate shadows for better performance and new ideas.

References

[1] Jin-Cyuan Lai; Shih-Shinh Huang; Chien-Cheng Tseng; , "Image-based vehicle tracking and classification on the highway," Green Circuits and Systems (ICGCS), 2010 International Conference on , vol., no., pp.666-670, 21-23 June 2010 doi: 10.1109/ICGCS.2010.5542980

[2] Bishop, A.N.; Savkin, A.V.; Pathirana, P.N.; , "Vision-Based Target Tracking and Surveillance With Robust Set-Valued State Estimation," Signal Processing Letters, IEEE , vol.17, no.3, pp.289-292, March 2010 doi: 10.1109/LSP.2009.2038772

[3] Woo, H.; Jung, Y.; Kim, J.; Seo, J.; , "Environmentally Robust Motion Detection for Video Surveillance," Image Processing, IEEE Transactions on , vol.PP, no.99, pp.1-1, 0 doi: 10.1109/TIP.2010.2050644

[4] Zhen Li; Zhiqiang Wei; Bo Yin; Xiaopeng Ji; Ruobing Shan; , "Pedestrian Detection Based on a New Two-Step Framework," Education Technology and Computer Science (ETCS), 2010 Second International Workshop on , vol.3, no., pp.56-59, 6-7 March 2010 doi: 10.1109/ETCS.2010.160

[5] Hedayati, M.; Zaki, W.M.D.W.; Hussain, A.; , "Real-time background subtraction for video surveillance: From research to reality," Signal Processing and Its Applications (CSPA), 2010 6th International Colloquium on , vol., no., pp.1-6, 21-23 May 2010 doi: 10.1109/CSPA.2010.5545277

[6]Gyu-Jin Kim; Ki-Yeol Eom; Moon-Hyun Kim; Jae-Young Jung; Tae-Ki Ahn; , "Automated measurement of crowd density based on edge detection and optical flow," Industrial Mechatronics and Automation (ICIMA), 2010 2nd International Conference on , vol.2, no., pp.553-556, 30-31 May 2010 doi: 10.1109/ICINDMA.2010.5538248

[7]Saleemi, Imran; Hartung, Lance; Shah, Mubarak; , "Scene understanding by statistical modeling of motion patterns," Computer Vision and Pattern Recognition (CVPR), 2010 IEEE Conference on , vol., no., pp.2069-2076, 13-18 June 2010 doi: 10.1109/CVPR.2010.5539884

[8]Yuk, J.S.-C.; Wong, K.-Y.K.; "An efficient pattern-less background modeling based on scale invariant local states"; Advanced Video and Signal-Based Surveillance (AVSS); 2011 8th IEEE International Conference on Digital Object Identifier: 10.1109/AVSS.2011.6027338, pp 285 – 290, 2011

[9]Uzair, M.; Khan, W.; Ullah, H.; ur Rehman, F., "Background modeling using corner features: An effective approach", Multitopic Conference, 2009. INMIC 2009. IEEE 13th International; Digital Object Identifier: 10.1109/INMIC.2009.5383113, pp 1 – 5, 2009

[10] Tao Lei; Yangyu Fan; Liandong Li, "The Algorithm of Moving Human Body Detection Based on Region Background Modeling", Computer Network and Multimedia Technology, 2009. CNMT 2009. International Symposium on; Digital Object Identifier: 10.1109/CNMT.2009.5374792, pp1 – 4, 2009

[11]Chih-Yang Lin; Chao-Chin Chang; Wei-Wen Chang; Meng-Hui Chen; Li-Wei Kang, "Real-Time Robust Background Modeling Based on Joint Color and Texture Descriptions", Genetic and Evolutionary Computing (ICGEC), 2010 Fourth International Conference on Digital Object Identifier: 10.1109/ICGEC.2010.159, pp 622 – 625, 2010

[12] Azab, M.M.; Shedeed, H.A.; Hussein, A.S., "A new technique for background modeling and subtraction for motion detection in real-time videos", Image

Processing (ICIP), 2010 17th IEEE International Conference on Digital Object Identifier: 10.1109/ICIP.2010.5653748, pp 3453 - 3456, 2010

[13] Dongfa Gao; Zhuolin Jiang; Ming Ye, "A New Approach of Dynamic Background Modeling for Surveillance Information", Computer Science and Software Engineering, 2008 International Conference on Volume: 1 Digital Object Identifier: 10.1109/CSSE.2008.601, pp850 – 855, 2008

[14]Mendizabal, A.; Salgado, L., "A region based approach to background modeling in a wavelet multi-resolution framework", Acoustics, Speech and Signal Processing (ICASSP), 2011 IEEE International Conference on Digital Object Identifier: 10.1109/ICASSP.2011.5946557, pp929 – 932, 2011

[15]Weiqiang Wang; Jie Yang; Wen Gao, "Modeling Background and Segmenting Moving Objects from Compressed Video", Circuits and Systems for Video Technology, IEEE Transactions on Volume: 18, Issue: 5 Digital Object Identifier: 10.1109/TCSVT.2008.918800, pp670 - 681, 2008

[16]Xingzhi Luo; Bhandarkar, S.M.; Wei Hua; Haisong Gu, "Nonparametric Background Modeling Using the CONDENSATION Algorithm", Video and Signal Based Surveillance, 2006. AVSS '06. IEEE International Conference on Digital Object Identifier: 10.1109/AVSS.2006.81, pp 3, 2006

[17]Vemulapalli, R.; Aravind, R., "Spatio-temporal nonparametric background modeling and subtraction", Computer Vision Workshops (ICCV Workshops), 2009 IEEE 12th International Conference on Digital Object Identifier: 10.1109/ICCVW.2009.5457574, pp 1145 - 1152, 2009

[18]Huan Wang; Ming-Wu Ren; Jing-Yu Yang, "Background Modeling Method Based on Sequential Kernel Density Approximation", Pattern Recognition, 2008. CCPR '08. Chinese Conference on Digital Object Identifier: 10.1109/CCPR.2008.44, pp 1 – 6, 2008

[19]Jie Ma; Shutao Li, "Moving Target Detection Based on Background Modeling by Multi-level Median Filter", Intelligent Control and Automation, 2006. WCICA 2006. The Sixth World Congress on Volume: 2 Digital Object Identifier: 10.1109/WCICA.2006.1713948, pp 9974 – 9978, 2006

[20]Shaoqiu Xu, "Dynamic Background Modeling for Foreground Segmentation", Computer and Information Science, 2009. ICIS 2009. Eighth IEEE/ACIS International Conference on Digital Object Identifier: 10.1109/ICIS.2009.102, pp 599 - 604, 2009

[21]Liyuan Li; Weimin Huang; Irene Yu-Hua Gu; Qi Tian, "Statistical modeling of complex backgrounds for foreground object detection", Image Processing, IEEE Transactions on Volume: 13 , Issue: 11 Digital Object Identifier: 10.1109/TIP.2004.836169, pp 1459 – 1472, 2004

[22]Jin Yu; Xuan Zhou; Feng Qian, "Object kinematic model: A novel approach of adaptive background mixture models for video segmentation," Intelligent Control and Automation (WCICA), 2010 8th World Congress, Digital Object Identifier: 10.1109/WCICA.2010.5554402, pp.6225-6228, 2010

[23]Lijing Zhang; Yingli Liang, "Motion Human Detection Based on Background Subtraction," Education Technology and Computer Science (ETCS), 2010 Second International Workshop, vol.1 Digital Object Identifier: 10.1109/ETCS.2010.440, pp.284-287, 2010

[24]Hedayati, M.; Zaki, W.M.D.W.; Hussain, A., "Real-time background subtraction for video surveillance: From research to reality," Signal Processing and

Its Applications (CSPA), 2010 6th International Colloquium, Digital Object Identifier: 10.1109/CSPA.2010.5545277, pp.1-6, 2010

[25]Xuejiao Li; Xiaojun Jing, "FPGA based mixture Gaussian background modeling and motion detection", Natural Computation (ICNC), 2011 Seventh International Conference on Volume: 4 Digital Object Identifier: 10.1109/ICNC.2011.6022578, pp 2078 – 2081, 2011

[26] Fan-Chieh Cheng; Shih-Chia Huang; Shanq-Jang Ruan, "Illumination-Sensitive Background Modeling Approach for Accurate Moving Object Detection", Broadcasting, IEEE Transactions on Volume: 57 , Issue: 4 Digital Object Identifier: 10.1109/TBC.2011.2160106, pp794 – 801, 2011

[27]Caseiro, R.; Henriques, J.F.; Batista, J., "Foreground Segmentation via Background Modeling on Riemannian Manifolds", Pattern Recognition (ICPR), 2010 20th International Conference on Digital Object Identifier: 10.1109/ICPR.2010.871, pp 3570 - 3574, 2010

[28]Charoenpong, T.; Supasuteekul, A.; Nuthong, C., "Adaptive background modeling from an image sequence by using K-Means clustering", Electrical Engineering/Electronics Computer Telecommunications and Information Technology (ECTI-CON), 2010 International Conference, pp 880 – 883, 2010

[29]El Baf, F.; Bouwmans, T.; Vachon, B., "Fuzzy statistical modeling of dynamic backgrounds for moving object detection in infrared videos", IEEE Computer Society Conference on Computer Vision and Pattern Recognition Workshops, 2009. CVPR Workshops 2009, Digital Object Identifier: 10.1109/CVPRW.2009.5204109, pp 60 - 65, 2009

[30]Doulamis, A.; Kalisperakis, I.; Stentoumis, C.; Matsatsinis, N., "Self Adaptive background modeling for identifying persons' falls", 5th International Workshop on Semantic Media Adaptation and Personalization (SMAP) 2010, Digital Object Identifier: 10.1109/SMAP.2010.5706861, pp 57 - 63, 2010

[31]Jiangming Kan; Keyi Li; Jun Tang; Xiaofeng Du, "Background modeling method based on improved multi-Gaussian distribution", International Conference on Computer Application and System Modeling (ICCASM) 2010, Volume: 2, Digital Object Identifier: 10.1109/ICCASM.2010.5619314, pp 214-218, 2010

[32]Peng Suo; Yanjiang Wang, "An improved adaptive background modeling algorithm based on Gaussian Mixture Model", 9th International Conference on Signal Processing (ICSP) 2008, Digital Object Identifier: 10.1109/ICOSP.2008.4697402, pp 1436 – 1439, 2008

[33]Haq, Anwaar-ul; Gondal, I.; Murshed, M., "Automated multi-sensor color video fusion for nighttime video surveillance", IEEE Symposium on Computers and Communications (ISCC) 2010, Digital Object Identifier: 10.1109/ISCC.2010.5546791, pp.529-534, 2010

[34]A.Djouadi, O.Snorrason et F.Garber, The quality of training-sample estimates of Bhattacharyya coefficient, IEEE transactions on Pattern Analysis and Machine Intelligence, vol. 12, n°1, pp 92-97,1990

[35]Jianhua Lin, Member, IEEE, "Divergence Measures Based on the Shannon Entropy", IEEE transactions on information theory. vol. 37, no. i , 1991

[36]Charoenpong, T.; Supasuteekul, A.; Nuthong, C., "Adaptive background modeling from an image sequence by using K-Means clustering", International Conference on Electrical Engineering/Electronics Computer Telecommunications

and Information Technology (ECTI-CON) 2010, pp.880-883, 2010

[37]Huazhong Xu; Pei Lv; Lei Meng, "A people counting system based on head-shoulder detection and tracking in surveillance video", International Conference on Computer Design and Applications (ICCDA)2010, vol.1, Digital Object Identifier: 10.1109/ICCDA.2010.5540833, pp.V1-394-V1-398, 2010

AN IMPROVED ADAPTIVE THRESHOLDING SCHEME FOR FAULT DETECTION: APPLICATION TO A CEMENT ROTARY KILN SYSTEM

Boualem Ikhlef[1], Abdelmalek Kouadri[2], Abderrazek Bensmail[3] and Mimoun Zelmat[1]

[1]Applied Control Laboratory, University of Boumerdes, Av. de l`indépendance, 35000 Boumerdès, Algeria. Email:blm_ikhlef@yahoo.fr

[2]Institute of Electrical and Electronics Engineering,University of Boumerdes, Av. de l`indépendance, 35000 Boumerdès, Algeria.

E-mails:ab_kouadri@hotmail.com

[3]Ain El Kebira Cement Plant, SCAEK, BP 01, 19400 Ain El Kebira, Algeria.

E-mail: aek_bensmail@yahoo.fr

Abstract

Projection methods have been extensively employed for monitoring operation in several industrial processes. Their capabilities, to measure variability in a given process, make them more attractive to the users. Instead, the important numbers of measured signals, these techniques make process's monitoring operation more ergonomic, and easy to exploit the information given by measured signals. In this paper, we develop an adaptive thresholding approach in order to detect, analyze and diagnose faults in a cement rotary kiln system. The developed threshold is obtained using statistical tools based on two-dimensional plot for large-sized multivariate measured data. These two statistical dimensions represent the instantaneous mean and variance of the measured signals in the cement plant. The obtained threshold' performances are compared with the fixed threshold technique through the rate of false alarms. In addition, two natural faults are used to show that the developed threshold can accurately detect their occurrence. The accuracy, robustness and effectiveness of the adaptive threshold depend primarily to the computed confidence intervals, after testing the distribution law of the mean and variance data using Shapiro-Wilk method. The obtained confidence intervals are sufficient to constitute a powerful and interesting tool to overcome the difficulties of parametric uncertainties quantification and devices measurement inaccuracies which increase false alarms. It is also important to note the high sensitivity of proposed fault detection scheme in detecting faults with relatively low amplitudes.

Keywords — Fault detection, adaptive threshold, large sized multivariate data, mean, variance, statistical test, confidence interval, significance level, cement rotary kiln.

CRASH RESISTANCE SIMULATION, AN INVESTIGATION INTO VEHICLE FRAME STIFFNESS IN FULL FRONTAL IMPACT TEST USING LS DYNA

Benhizia A.[1, *], Outtas T.[1]

[1] Mechanics of Structures and Materials Laboratory, University Hadj Lakhdar, Batna, Algeria

[*]Corresponding author. Tel.: +213794662415; fax: +213 33 81 21 43

E-mail address: benhiziauniv@yahoo.fr

Abstract

In the crash-test, keeping the space around the occupants remains the subject of research for the automobile manufacturers. The analysis of the crash-test with explicit finite element programs such as LS-DYNA helps us to reduce the actual testing on prototypes in the automotive industry. The frontal crash is extremely fast, it is about 120ms, the physical knowledge of the frame leader sheets are very difficult to obtain and control during this time. We are interested to study and optimize the nonlinear dynamic behavior of a frame leader model examining the influence of local changes on the geometry of the frame rail and the configuration of assembly. The model of the frame chosen, it consists mainly of two beams connected with ties. We have used "solid works" for the design of the model parts. Three configurations represent the model's geometry of the frame studied. .The dynamics resulting In the 3 configurations, shows that the vulnerable areas caused the initiation of lateral deflection, this does not allow the absorption of shock causing a large deformation of the frame. The results lead us to conclude a preliminary choice of a complete tubular structure for the frame parts, the proper choice of the shape of the frontal part allows starts the buckling in a predetermined direction, This is numerically stabilized in the model by using a small crease, putting the part of the carrier more rigid than the frontal one.

Keywords: frontal crash / dynamic / non linear / finite element

Introduction

Precise deformation modeling is the key to reduced vehicle structures damage [1,2]. The goal of crashworthiness was to avoid vehicle deformations as much as possible. Over the years, the body structures evolved to include progressive crush zones to absorb part of the crash kinetic energy by plastic deformations. The front and rear part of the automobile frame are areas where the deformation is controlled [3], there is a great necessity to be able to control the deformation of the structure. This can be realized by a special distribution and orientation of the structural stiffness. As part of this effort, computer models of automobile frame with sheet metal forming processes have been developed and applied to determine the crash response of rail equipment. Numerical simulation is carried out with LS-DYNA3D in order to identify the forming effect on the crashworthiness.

2. Geometry

As a first step, we will model the frame chosen, it consists mainly of rails connected and ronforced.

the software Solid Works will be used as a tool for creating 3-D models part. Three different configurations represent the model's geometry of the frame studied.

2.1 Model Geometry

The frame rail is partitionned into two parts (figure 1). In the first test, the front rail part is a tube, with length of 600 mm, this part being deformable under the action of a frontal impact [1,2], its installed to join the U-shaped rail extention part , this one being used to carry the vehicle body. The deformation in this part is much less than the preceding one because of the rigid assembly [3,4].

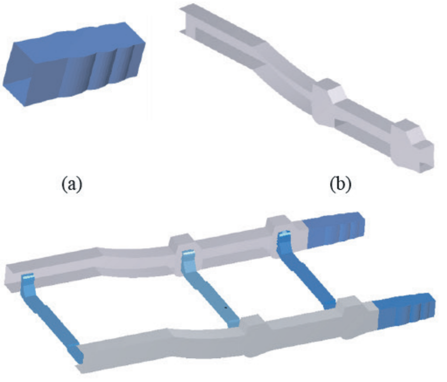

Figure 1. 1st geometry configuration
Front frame rail, (b) Rail extention

2.2 Model Geometry

In the second test (figure 2), the front frame rail geometry is formed in a "U-shaped" configuration and assembled to the remainder of the tubular rail extention.

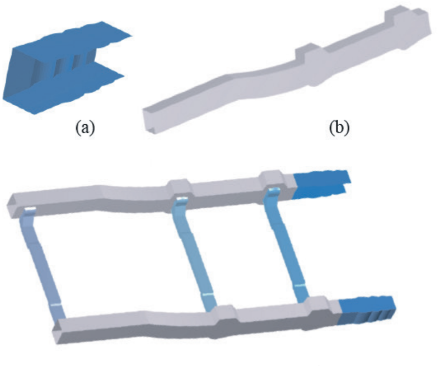

Figure 2. 2nd geometry configuration
(a) Front frame rail, (b) Rail extention

2.3 Model geometry

In the third test (figure 3), the frame rail is formed by the assembly of two parts formed in a Ushaped Configuration.

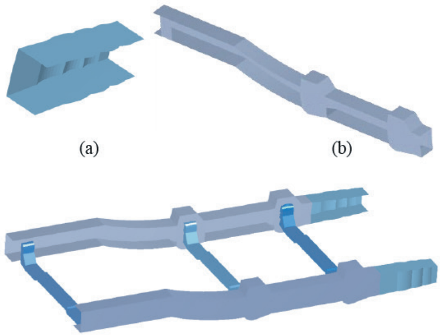

Figure 3. 3rd geometry configuration
(a) Front frame rail, (b) Rail extention

3. Material Model

Recent studies show that the hardening characteristics and the strain rate sensitivity of the materials significantly affect the crush response [1,5]. Therefore, the modeling of the stress–strain relationship of the material is a crucial issue in the numerical simulations of an impact event, particularly for materials showing large strain hardening. Type 24, one of the material models available in LS-DYNA, is a piecewise linear isotropic elasto-plastic material model. In this model, strain rate sensitivity is taken into account and the relation between the dynamic stress and the strain rate of a particular metallic alloy is given by Cowper–Symonds relation [6].

$$\sigma_y = \left[1 + \left(\frac{\dot{\varepsilon}}{c} \right)^{1/p} \right] . \sigma_0$$

Where: σ0 is the initial elastic stress, έ is the rate of deformation, C and P is the Cowper-Symonds
parameters.

4. Finite Element Modeling

The code LS-DYNA version 970 was used in all finite element simulations. Although the boundary conditions in an actual crashing event are very complicated, depending on the constraints of the object to be hit, it is assumed that the crushing object is rigid body fully fixed . This rigid body is modeled as an analytical rigid surface. The geometry is meshed within ANSA. The parts of the
finite element model are modelled using four-node Belytschko-Tsay shell elements; the result is a finite element model, where only the constraints and loads have to be applied to be ready for the solution process.

5. Crush Simulations and Results

To determine the effects of frame rail geometry on the crush response of the component we chose the frontal impact test using the simulation software LS DYNA. Generally, it takes 20–40 ms to deform front frame which depends on the space of the engine room and the length of the front frame [2], the frame geometry made of 2 mm thick sheet metal. The frame model is crushed at an impact velocity of 15.5 mm/ms into a perpendicular rigid wall (figure 4) and the termination time is 40 ms.

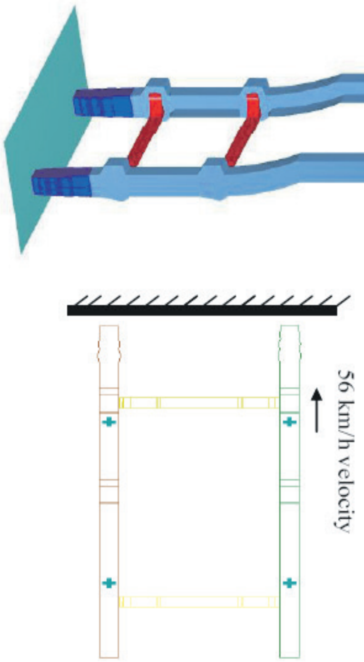

Figure 4. Position of the model and the barrier in case of frontal impact 56 km/h

The Numerical results are presented for the three impact test cases after 40 ms in stress and deformation of the models geometries.

5.1 Model Results

5.1.1 Plastic Strain

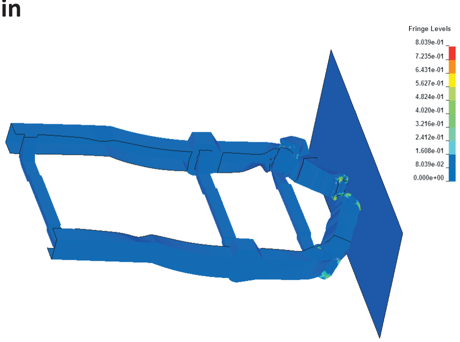

Figure 6. plastic strain,in
final configuration (1st model), t=40ms

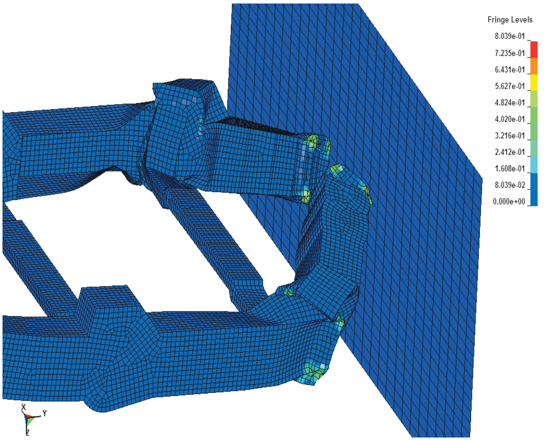

Figure 7. Zoom in,plastic strain concentration,(1st model) , t=40ms

Figure 6 illustrates the influence of the first modification on the frame, the failure areas are in the second part of the frame (rail extention figure 7), and this impact reveals that the lateral deflection

of the front frame rail with a tubular form does not allow the absorption of the shock, therefore strong deformation of the vehicle body.

5.1.2 Von misses stress

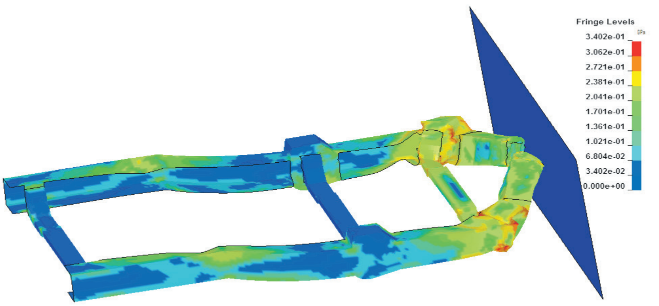

Figure 8. , von Mises stress (GPa), in final configuration (1st model), t=40ms

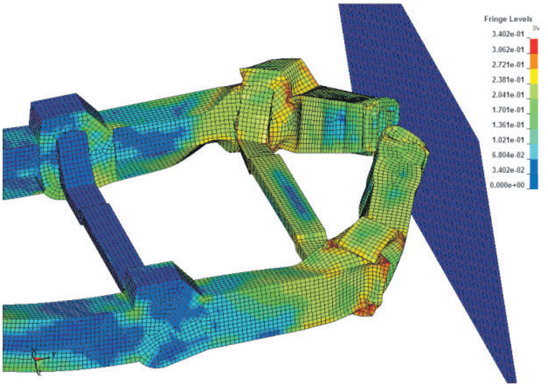

Figure 9. Zoom in ,von Mises stress, concentration, 1st model, t=40ms

The detailed evaluation of the base frame failures reveals that only the 2nd part(rail extension Figure 8), is subjected to the residual and high cyclical stresses which cause premature failure, in the absence of primary reinforcement and the lateral deflection of the front rail part (figure 9). The excessive rigidity of the front rail part (tube form) transmits the deformations to the frame rail extension.

5.2 Model Results

5.2.1 Plastic Strain

Figure 10 shows the influence of the second modification on the frame.

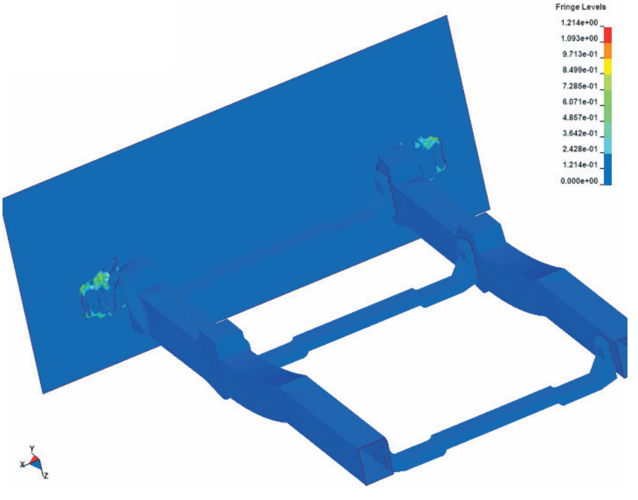

Figure 10. Plastic strain in,final configuration ,(2nd model), t=40ms

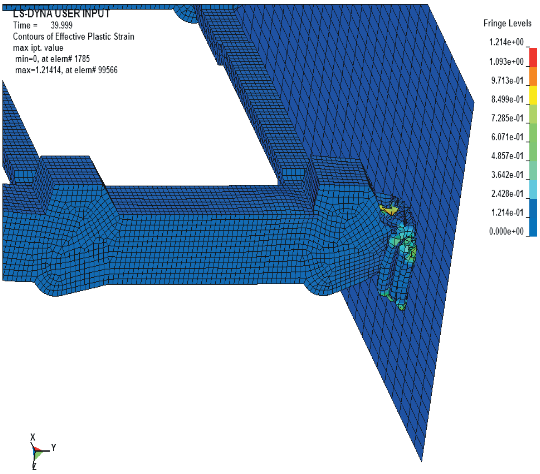

Figure 11. Zoom in, plastic strain concentration, (2nd model), t=40ms

It is noticeable from this configuration that the front frame rail (U form) is deformed and deviated at the same time, Consequently, we can see that the second part of the frame (rail extention) preserves its geometry compared to the initial state (figure 11). As a result, during the crash event, the initial deformation is localized and enabling the crush pattern to be designed directly into the front frame rail.

5.2.2 von misses stress

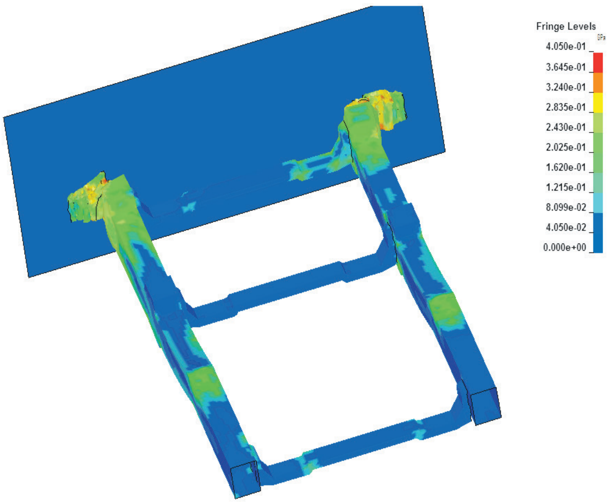

Figure 12. von Mises stress (GPa) in final configuration (2nd model), t=40ms

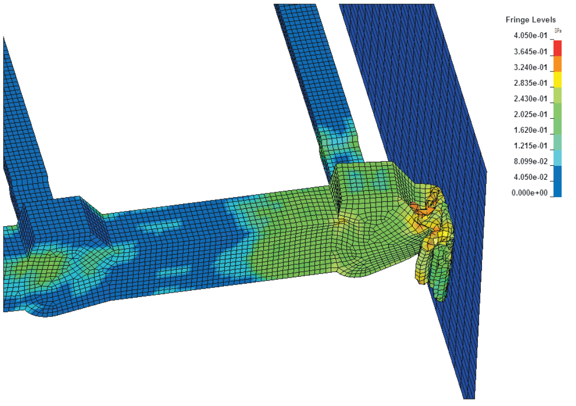

Figure 13. Zoom in, von Mises
Stress concentration, (2nd model) t=40ms

Figure 12 shows that the proper choice of the shape of the frontal part allows starts the buckling in a predetermined direction as a result, the stress concentration which may occur in the front frame rail putting the rail extention more rigid (figure 13).

5.3 Model Results

5.3.1 Plastic Strain

Figure 13 illustrates the influence of the third geometrical modification on the frame.

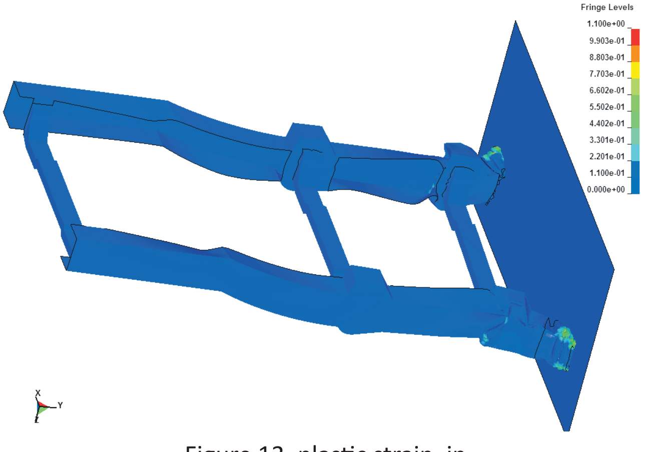

Figure 13. plastic strain, in
final configuration (3rd model), t=40ms

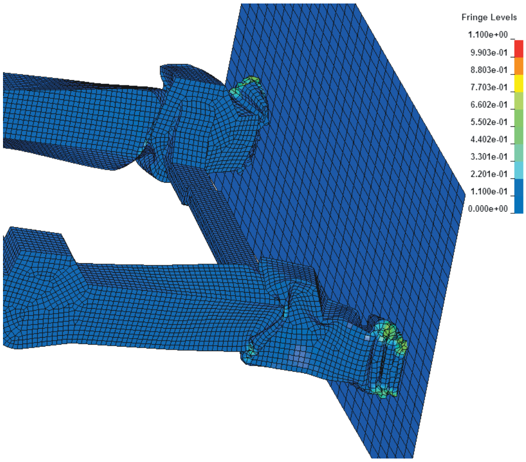

Figure 14. Zoom in, plastic strain,
(3rd model),t=40ms

The failure areas are localized in the second part (rail extention figure 14), as result, it caused the initiation of lateral deflection, this does not allow the absorption of shock causing a large deformation of the rail extention, that requires reinforcements in this part to avoid the rotation of the frontal part during the impact.

5.3.2 von misses stress

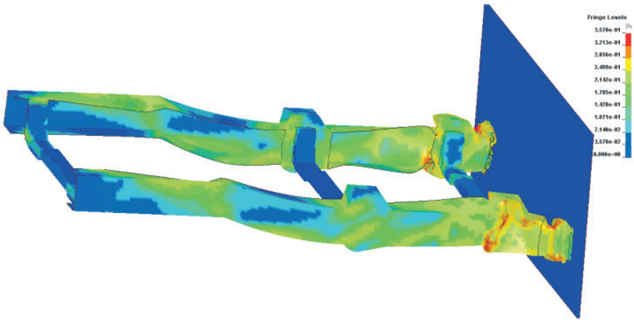

Figure 15. von Mises stress (GPa) in final configuration (3rd model), t=40ms

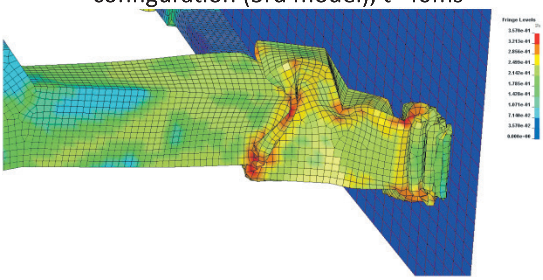

Figure 16. Zoom in , von Mises stress concentration, (3rd model), t=40ms

In this case, the stress concentration in the rail extention shows that the U shape of this one leds to

create the failure areas (figure 15), consequently we lose all the length of the frontal part during the impact because of the lateral deflection. This third geometry presents a similar behavior with the first one (lateral deflection), even it is less (figure 16), it always poses a safety problem.

6. Results Comparison

The results of the lateral deflection of the front frame rail during the impact simulation are summarized in the lateral displacement(x-direction) of an element located directly on the outside surface of the frontal part during the contact between this part and the fixed obstacle (figure17), this one is shown in the figure 18.

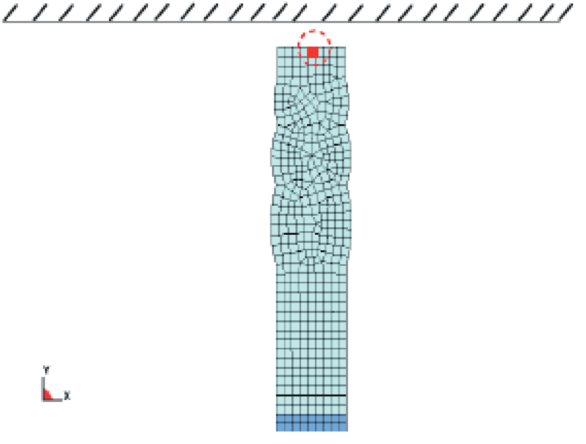

Figure 17. Element chosen and position in the front frame rail

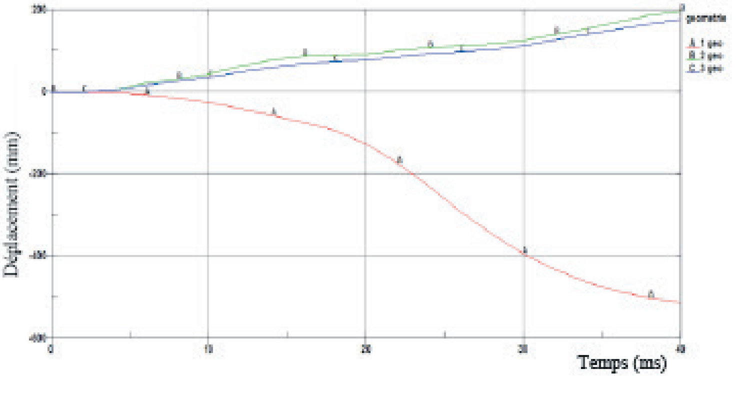

Figure 18. The lateral displacement of an element located directly on the surface of front frame rail

In the 1st assembly The excessive rigidity of the frontal part (tube form) initiate the lateral deflection The displacement response shows a total y-rotation of the front frame rail and a maximum displacement is shown in this assembly (500 mm occurs at 40 milliseconds), after which the structure loses its frontal part, and transmits the deformations towards the back of the frame (rail extention). The 2nd assembly affirms that the shape of the front frame rail part allows starts the buckling in a predetermined direction and all deformations are consumed in this part, putting the part of the carrier more rigid during the shocks. In the 3rd assembly the maximum deflection occurs at 40 ms of approximately 200 mm this will be create the failure areas on the rail extension.

7. Conclusion

Designers typically engineer structures using elastic analysis to withstand service loads without yielding or collapsing. Automotive structures, however, must meet all previously mentioned service load requirement, plus it must deform plastically in a short period of time (milliseconds) to absorb the crash energy in a controllable manner. The results in the stress and plastic strain allowed us to affirm that to absorb and channel the deformation during the frontal impact, it would be more judicious not to adopt the U shape on the frontal part of the frame.

The evolution of the Von Misses stress in the 3 configuration after the impact of 40 ms shows that the stress concentrates primarily on the level of the edges of the tubes forming the rail, and not on the flat shapes.While following the same reasoning, unlike the first and the third assembly, in the 2nd geometry the stress concentration was established in the front frame rail, this one strongly made the vehicle body more rigid. This led us to conclude that the final design was the product of a long evolution guided primarily by testing,the most important factor is the choice of geometry frame rail, such as a complete tubular structure form of the frame rail.

References

[1] Recep Gumruk, Sami Karadeniz, A numerical study of the influence of bump type triggers on the axial crushing of top hat thin-walled sections, Thin-Walled Structures 46, 1094–1106, 2008

[2] Yong-Bum Cho, Chul-Ho Bae, Myung-Won Suh, Hyo-Chol Sin, Thin-Walled Structures 44 ,415–428, 2006

[3] Shujuan Hou, Qing Li, Shuyao Long, Xujing Yang, Wei Li, Crashworthiness design for foam filled thin-wall structures, Materials and Design 30 , 2024–2032,2009

[4] Reid JD, Towards the understanding of material property influence on automotive crash structures, Thin-Walled Structures, 24:285–313, 1996

[5] Yuxuan Li, Zhongqin, Lin, Aiqin Jiang, Guanlong Chen, Use of high strengthsteel sheet for lightweight and crashworthy car body,Materials and Design 24, 177- 182. 2003

[6] LS-DYNA Keyword user's manual, Livermore Softmore Technology Corporation, Version 970, 2003

RELIABILITY STUDY FOR A MECHANISM AIDED BY ASYNCHRONOUS ACTUATOR POWERED BY ASYNCHRONOUS DIESEL GENERATOR

H. Meglouli ;A Chebouba;Y Naoui

hmeglouli@yahoo.fr

Laboratoire d'électrification des entreprises industrielles

University of Boumerdes- Algeria

Tel/Fax: 213 24 81 17 33

Abstract- The modern electric facilities are equipped by a great number of different mechanisms and devices actioned by Asynchronous electric Motor (ASM), the power of these motors is equal to the power of the generating devices, where their most complicated working regime is the starting when their power is equal to the power of the generating devices.

In this regime we can have an overcharge of the generating devices by the active and reactive power.

For this reason, this article is dedicated to the study of the starting methods of asynchronous motors that action the mechanisms and that are powered by Asynchronous Generating Diesel (AGD) with a limited capacity of DRY value and a given couple of resistance.

Keywords: Reliability, Autonomous asynchronous generator, starting of the asynchronous motors, Tention converter.

Introduction :

There are several factors that considerably influence the characteristics of the asynchronous motors starting process from a AGD, amongst these factor:

-The initial conditions of the process,

- The oscillation of frequency and amplitude of the AGD tension, - The non linear character of the electric machines parameters used as an actioner motor for the generator,

-The mechanisms resistant couple.

If we take into account these factors, the study of the transient regime in the AGD-ASM system using analytical methods will be complex and will induce high calculations uncertainties. In this article, we will study the analysis of the regimes dynamics of the starting from AGD of mechanisms with asynchronous electric actionner using a numerical method to achieve a given precision of the calculations.

2-Mathematical model of the starting regime of mechanisms with asynchronous actionner powered by AGD

A- General characteristic of the model

Studies performed previously have shown that for a complete analysis of the common operating regime of AGD and ASM, it is necessary that the mathematical model takes into account the review of the transient regimes for the direct starting of the motor, the starting through an auxiliary resistance in the statoric circuit as well as the starting through the Tension Converters with Thyristors (TCT). In addition to considering the electromagnetic systems properties, the supplying of the consumers by a three-phased tension under neutral line, the necessity in a large interval of the regulation of the key elements starting angle value (because the actioning mechanisms has the same power that the generator) In the mathematical model, the functioning of the TCT of 3TT type that is composed of two thyristors connected head to foot in every phase of the supplying line is described.

B- Mathematical model of the asynchronous motor with short-circuited rotor.

In order to study the operating regime of ASM with the auxiliary elements connected to its statoric coil, we have to write the composed differential equations in relation to the statoric current and to the rotoric hooking flux in a simple shape [1]. [2]. [3] in the (α, β, σ) coordinate system.

The ASM equations are the folowing:

$$\frac{di_{\alpha M}}{d\tau} = \left[U_\alpha - R_{SM} i_{\alpha M} - L_1 (r_{rM} L_1 . L_{\alpha M} - T_1 \psi_{\alpha M} - w_{rM} \psi_{\beta M}\right] \frac{1}{L_S \Sigma}$$

$$\frac{di_{\beta M}}{d\tau} = \left[U_\beta - R_{SM} i_{\beta M} - L_1 (r_{rM} L_1 . L_{\beta M} - T_1 \psi_{\beta M} - w_{rM} \psi_{\alpha M}\right] \frac{1}{L_S \Sigma}$$

$$\frac{d\psi_{\alpha M}}{d\tau} = r_{rM} L_1 . i_{\alpha M} - T_1 \psi_{\alpha M} - w_{pM} \psi_{\beta M}$$

$$\frac{d\psi_{\beta M}}{d\tau} = r_{rM} L_1 . i_{\beta M} - T_1 \psi_{\beta M} - w_{rM} \psi_{\alpha m}$$

where :

$$R_{sM} = r_{rM} + R_n$$

$$L_{s\Sigma} = L_{sM} + L_n$$

$$L_1 = \frac{L}{L_{mM} + L_{rM}}$$

$$T_1 = \frac{r_{rM}}{L_{mM} + L_{rM}}$$

$L_{rM}$and L_{sM}:ASM's rotoric and statoric flux scattering inductances.

L_n **:** Inductance of the auxiliary resistance.

L_{mM}**:**Mutual inductance of the ASM's statoric and rotoric coils .

w_{rM}:The pulsation of the ASM's rotor rotation speed.

i_M : ASM statoric current .

ψ_M :Hooking flux of the ASM's rotor

The calculation of the transient regime in the ASM is performed in a relative units system, the nominal current amplitudes and the generator tension are taken as basis value, the basis time is the same for the processes calculation. The instantaneous values of the motor current in the generator relative units system are transformed using of the transfer coefficients

$$K_\sigma = \frac{i_{\sigma M}}{i_{\sigma G}}$$

$i_{\sigma M}$ and $i_{\sigma G}$: Basis values of the currents in the motor and the generator relative units system.

The electromagnetic couple developed by ASM is determined by the formula (2):

$$C_M = \psi_{\alpha M} . i_{\beta M} - \psi_{\beta M} . i_{\alpha M}$$

The equation of the movement of the mechanism axis that action the ASM is:

$$\frac{dw_{rM}}{d\tau} = \frac{1}{J\Sigma}\left(C_M - \frac{C_{cM}}{C_{\sigma M}} \right)$$

J_Σ : Sum of the inertias couples of the ASM mobile mass and of the mechanism translated to the motor rotor

C_{cM} : Couple of the mechanism resistance (N.m).

$C_{\sigma M}$: Basis value of the ASM couple (N.m).

To take into account the influences of the rotor current and the saturation of the machine iron on the variation of the rotation frequency at the starting time we include in the mathematical model the relations linking the rotor scattering inductance and the motor rotor active resistance with the motor sliding [4].

$$r_{rM} = (r_{nr} - r_{rM}) g_M$$

$$L_{rM} = (L_{nr} - L_{rM}) g_M$$

Where:

r_{nr} : Active resistance of the rotor.

L_{nr} :Rotor scattering inductance at the starting.

g_M : Motor sliding (g_M =1)

C - Mathematical model of the Tension Converter with Thyristors TCT For the development of the TCT mathematical model we take into account the following [3]:

The arm of each branch is composed of two thyristors connected head to foot when the command signal arrives to the thyristor trigger and become in the closed state regardless of the system tension where it is present at that given moment.

The thyristor remains closed so far the value of the current that crosses it is higher than the upholding current.

In its closed state, the thyristor is replaced by an active resistance; the drop of tension in this latter one corresponds to the drop of tension value in the thyristor in the closed state.

In its open state, the thyristor is replaced by an active resistance in which the current becomes equal to the inverse current of the chosen thyristor.

Taking into account these simplifications, the control of the thyristors state is achieved by the analysis of every step of the command tension value calculation and the value of the current that crosses it at that given moment. To achieve this objective, the mathematical model takes into consideration the equations of the ASM phase current derived from the first two equations of the system (1)

$$\frac{di_a}{d\tau} = \left[\left(U_a - U_N\right) - R_{SM} i_a - L_1 (r_{rM} L_1 . i_a - w_r . \psi_{\beta M}\right] \frac{1}{L_{SM}}$$

$$\frac{di_b}{d\tau} = [\left(U_b - U_N\right) - R_{SM} i_b - L_1 [\left(\frac{1}{2}(r_{rM} L_1 . i_a - T_1 \psi_{\alpha M} - w_r . \psi_{\beta M})\right) + \frac{\sqrt{3}}{2}\left(r_{rM} L_1 \frac{i_b . i_c}{\sqrt{3}} - T_1 \psi_{\beta M} + w_{rM} . \psi_{\alpha M}\right)]] \frac{1}{L_{s\Sigma}}$$

$$\frac{di_c}{d\tau} = [\left(U_c - U_N\right) - R_{SM} i_c - L_1 [\left(-\frac{1}{2}(r_{rM} L_1 . i_a - T_1 \psi_{\alpha M} - w_{rM} . \psi_{\beta M})\right) - \frac{\sqrt{3}}{2}\left(r_{rM} L_1 \frac{i_b . i_c}{\sqrt{3}} - T_1 \psi_{\beta M} + w_{rM} . \psi_{\alpha M}\right)]] \frac{1}{L_{s\Sigma}}$$

Where:

$$U_a = U_\alpha$$

$$U_b = \frac{-U_\alpha}{2} + \frac{\sqrt{3}}{2} U_\beta$$

$$U_c = \frac{-U_\alpha}{2} - \frac{\sqrt{3}}{2} U_\beta$$

U_a, U_b and U_c :tensions of phases of AG

U_N : Tension between the neutral points of the AG and ASM statoric coils.

The functioning algorithm of TCT in the lack of a neutral link line in the naval network is limited by three possible conduction regimes that are:

- Three-phased conduction: closed arm for all phases.
- Two-phased conduction: closed arm for any phase.
- Neutral conduction: open state of the arms for the three phases.

For the TCT chosen types, taking into account the previous simplifications on the asynchronous machines symmetry,

U_N value can be determined for any time moment. At the time of the functioning of the symmetrical electric machines, U_N is different from zero only in the case of the two-phased conduction. For the thyristors that are used in the model and at the time of passing from TCT to any

conduction state that precedes the two-phased one, the initial values of the currents in the phases of open thyristor are equal in value but opposed in phase, on the other hand, U_N because in the AGD-ASM system, the symmetrical regime still exists at the following time moment. The same current will cross the two phases with open thyristor.

In these conditions, the instantaneous value of U_N can be calculated using the system of equations (7) that leads to the following values:

The phase (a) closed:

$$U_N = \left(U_b + U_c + L_1 . \frac{d\psi_{\alpha M}}{d\tau} \right) . \frac{1}{2.L_{sM}}$$

The phase (b) closed:

$$U_N = \left(U_b + U_c - L_1 . \left(\frac{1}{2} \frac{d\psi_{\alpha M}}{d\tau} - \frac{\sqrt{3}}{2} \frac{d\psi_{\beta M}}{d\tau} \right) \right) . \frac{1}{2.L_{sM}}$$

The phase (c) closed:

$$U_N = \left(U_a + U_b - L_1 . \left(\frac{1}{2} \frac{d\psi_{\alpha M}}{d\tau} - \frac{\sqrt{3}}{2} \frac{d\psi_{\beta M}}{d\tau} \right) \right) . \frac{1}{2.L_{sM}}$$

The opening of the thyristors command signal is formed using the command law taken for the TCT.

3- Algorithm of calculation of the starting regime

The simulation by MATLAB software of the system ((1) - (5)), using the Runge-Kutta method, has allowed us to get the following results of the ASM starting powered by AGD.

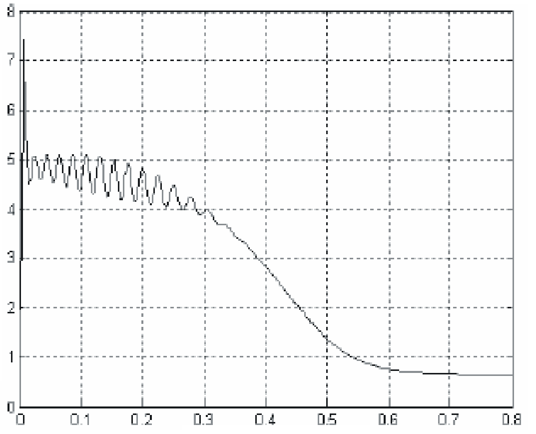

Fig. 1. Variations of the Is current in terms of the time for a direct ASM starting powered by AGD

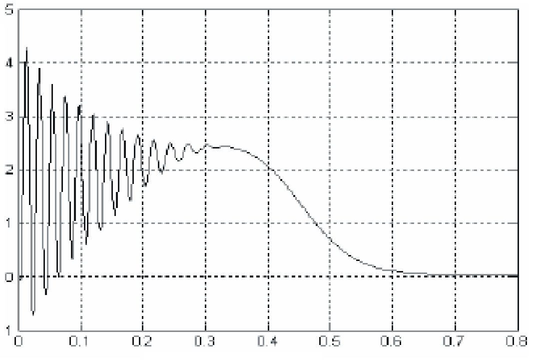

Fig. 2. Variations of the electromagnetic couple according to the time for a direct ASM starting powered by AGD

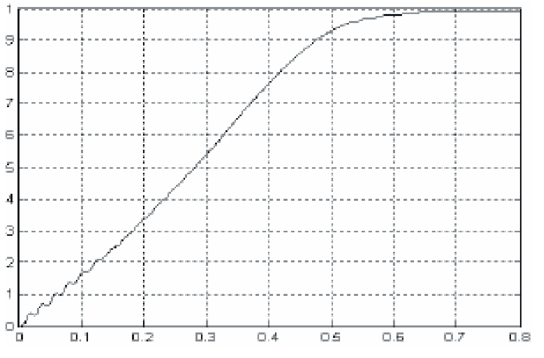

Fig. 3. Variations of the angular speed Wr according to the time for a direct ASM starting powered by AGD.

We notice on the three previous figures that at the time of the direct ASM starting powered by AGD, the existence of peaks of statoric currents and peaks of couple that can be the origin of the machine destruction by overheating, especially in the case of excessive repetitions

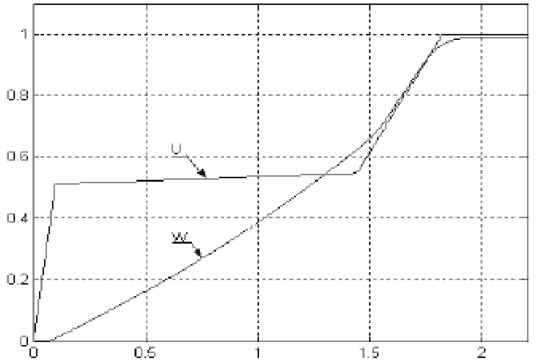

Fig. 4. Variations of the angular speed Wr and the U tension according to the time for an ASM starting with a TCT powered by AGD

We notice on this figure that for this type of starting the variation of tension that powers the ASM is progressive.

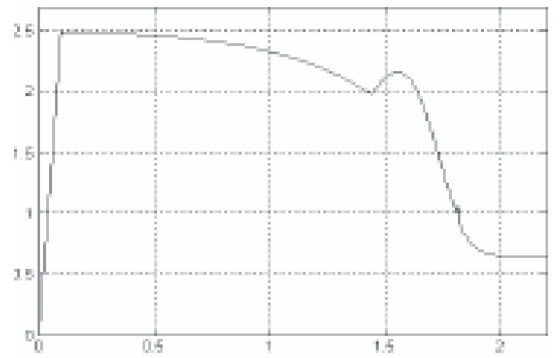

Fig. 5. Variations of the *Is* current in terms of time for an ASM starting with a TCT powered by AGD

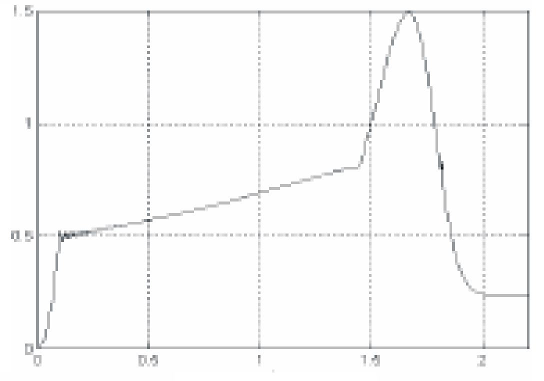

Fig. 6 . Variations of the electromagnetic couple Cem in terms of time for an ASM starting with a TCT powered by AGD

We notice on the two previous figures, the absence of any current or couple abrupt peaks. The resulting drop of tension that and mechanical shocks due to the brutal apparition of the couple. The starting time in this case can exceed the direct starting time by several times.

4 - Command of the starting regime by a Tension Converter with Thyristors

For an ASM starting, the limitation of the current peaks can be obtained not only by the reduction of the tension amplitude via the introduction of the auxiliary resistances in its statoric circuit, but also using other regulation methods of this tension value in the devices that allow the command of this starting regime, by means of varying the commutation of the allowed or blocked state of the semiconductor components (thyristor, power transistor, triac) [5]. [7]. [8].

The most efficient actionners of asynchronous mechanisms are the starting devices constructed on the basis of Tension Converters with Thyristor (TCT) commanded by a phase angle [8]. [9]. For an automatic command of the starting regimes of the asynchronous actionners mechanisms, several solutions exist currently. Amongst them we can mention the solution that uses gradators, where the power circuit includes in every phase two thyristors assembled head to foot; the variation of tension that powers the ASM is progressive and is obtained via varying the conduction time by phase angle of these thyristors during every half period (fig.7) [5]-[6].

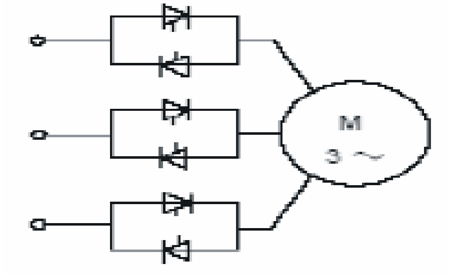

Fig. 7. Block diagram of the ASM starting through a gradator

This type of starting limits the call of current, the ensuing drop of tension and the mechanical shocks resulting from the brutal apparition of the couple. For the ADG energizing systems linked to an excitation device (DRY) whose action rapidity can be compared to the action rapidity of the command system by phase angle of the TCT key elements and which can have a positive effect if we introduce in the TCT automatic system a negative return loop between the starting angle of the thyristors' triggers and the drop of tension between the AGD limits. The possibility to use a system with TCT for the ASM starting command from an AGD is represented on the figure (8). For the elements of commutation we use some photothyristors that can be commanded by a luminous impulse. To assure a galvanic insulation between the power circuit and the command circuit at the time of the of the installation functioning, the primaries of the impulsion transformers T1-T3 are joined with the AGD statoric coils , the secondary of these transformers are plugged with the Zener diodes DZ7-DZ12 stabilizing the phases tensions. If a drop of tension appears the phase changes and the length of the command luminous impulse that determines the value of the starting angle of the photothyristor also changes. The choice of the command tensions phase angle and the parameters of the photothyristors allow the creation of a negative return loop by a drop of tension. We can have a large regulation interval of the photothyristors starting angle by means of the formation of the phase command signal that has a tension which exceed the anode-cathode tension of these photothyristors in a varying interval between 30° and 120°. The relation of the photothyristors starting angle with the tension phase amplitude is determined by the equation (8)

$$\alpha = \frac{\pi}{3} + \arcsin.\frac{U_{sT}.k_T}{U_m}$$

Where:

α : Pothothyristors starting angle

U_{sT} : Stabilizer tension

k_T : Transformers transformation coefficient

U_m : Amplitude of the tension phase instantaneous value

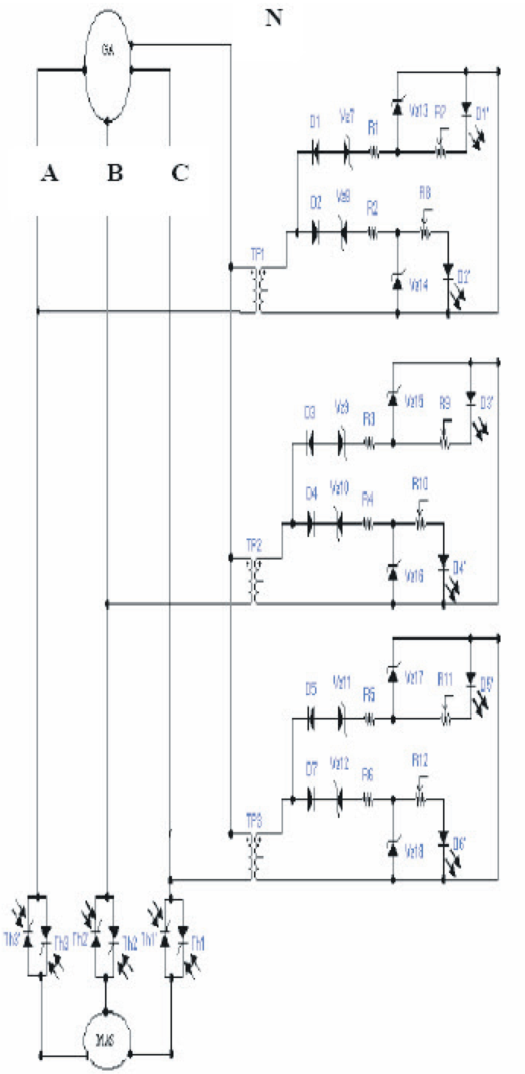

Fig. 8. Electric diagram of the ASM starting powered by AGD through a TCT

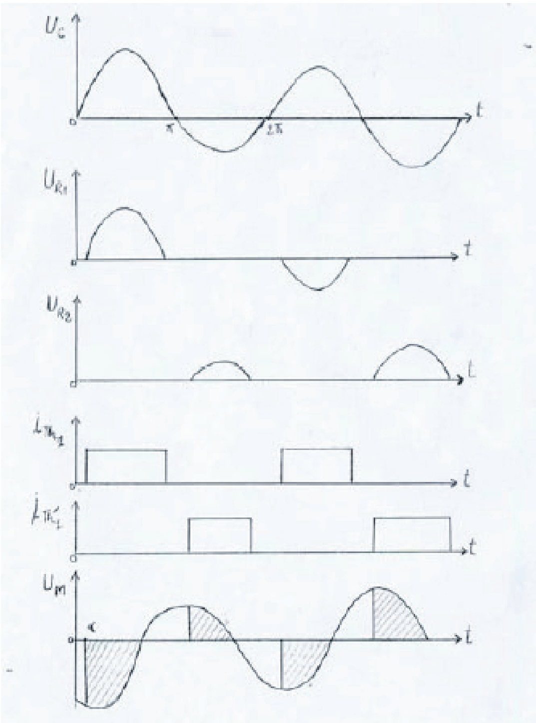

Fig . 9 . Functioning chronogram of the photothyristors

We take into consideration the variation character of the ASM power coefficient at the time of its starting. The chosen regulation interval of the starting angle is sufficient to command this starting because it ensures the conditions of TCT functioning in the case of three or two conductor arms.

On the figure (10) we represented the oscillogramms of the regime in the case of an ASM starting through a TCT [9] [10] [11]. The curves represent the effective tension value, the frequency of the diesel generator actionner and the starting duration of ASM for

different powers. The comparison between these features and the parameters of the ASM's direct starting regimes (fig(1)-(2)) permits to point out that the use of the TCT lead to the decrease the drop of tension in the load, the starting time in this case can exceed the time of direct starting by several multiples.

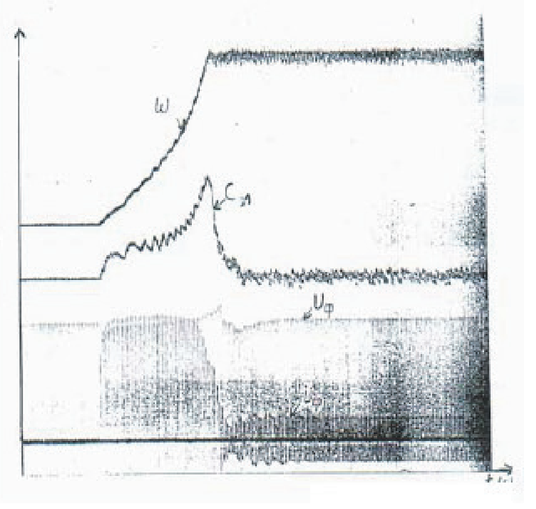

Fig . 10. Oscillogramme of the ASM starting powered by AGD through a TCT

5. Conclusion

We have developed a mathematical model of the common functioning regime dynamics of the AGD and of the mechanisms with asynchronous actionneur. This model takes into consideration the elements of the following system:

1- Diesel, asynchronous generating, asynchronous

motor with auxiliary resistances in the statoric circuit with a resistance couple on the corresponding axis of the different mechanisms, tension regulator with thyristors, the calculation parameters of the transient regimes are closer of the experimental data with a precision around 13%.

2- The calculations of the parameters of the asynchronous machines starting regimes of 4A, AM and AO series, for a capacity of DRY equal to 1.45 pu and for a limitation of tension drop on the borders of AGD of 20% of *Un* , give a steady direct starting of the asynchronous machines of a power of 20 to 25% of the nominal power of AG, without limitation of the tension drop value and for the same value of DRY capacity the AGD can assure a direct ASM starting with a power of 30 to 40% of the nominal power of AG.

3- The analysis of the possibilities of the starting regime command of the mechanisms with asynchronous actionner by a AGD with the use of a TCT with negative return loop between the angle of the thyristors triggers opened state and the drop of tension on the borders of AGD, shows that by this method we can limit the drop of tension on the borders of the load and can increase the unit of motors power started for a limited value of the DRY capacity. We noticed that the couple developed by ASM in the time of starting through a TCT has a smaller value compared to the starting through auxiliary resistances for the same value of tension drop that appeared on the AGD borders.

References

[1] T.A.Glasinko,V.I.Khrisanov, ''Les systèmes semiconducteurs des actionneurs électriques asynchrones impulsives à faible puissance '', Liningrad, Inergoatomisdat,1981,144 p.

[2] Abudura S., Konacof G.A. «La détermination de la puissance du Diesel naval dans l'exploitation » journal : Installation énergétique navale, N°2, Odessa, 2000, p 43-49.

[3] J.P .Caron. J-P.Hautier,''Modélisation et commande de la machine asynchrone'' Paris: éditions TECHNIP, 1995. 324p

[4] I.B.Kobilov, '' Les machines électriques, Moscou, Inergoatomisdat, 1986,360p

[5] I.B.Kobilov, '' La modélisation mathématiques des machines électriques '', Moscou, L'école supérieur, 1987,247p.

[6] S.Abudura,''Les regimes de fonctionnement des Diesels navals et des Diesels générateurs'', Odessa, Konsalting, 2002, 236 p.

[7] M.L.Doumbia « Outil d'aide à la conception des systèmes d'entraînement de machines électriques»,thése de doctorat ,Université de Montréal ,mai 2000, 178p.

[8] Y.Zidani , M.Naciri ,''A numerical Approach for the optimal capacitor used the self excited induction generator'',IEEE,2001.